Dissertation

submitted to the

Combined Faculty of Natural Sciences and Mathematics

of Heidelberg University, Germany

for the degree of

Doctor of Natural Sciences

Put forward by

Adrian Herkert

born in Mosbach

Oral examination: February 6, 2020

Characterization of a Monolithic Pixel Sensor Prototype in HV-CMOS Technology for the High-Luminosity LHC

Referees:

Prof. Dr. André Schöning

Prof. Dr. Ulrich Uwer

Zusammenfassung

Eine Aufrüstung des Large Hadron Colliders (LHC) ist in Planung, mit deren Hilfe dessen Potential bis zum Ende seiner Laufzeit voll ausgeschöpft werden soll. Die instantane Luminosität des sogenannten High-Luminosity LHC (HL-LHC) wird das 5- bis 7,5-fache des Werts betragen, für den der LHC ursprünglich ausgelegt war ($1 \cdot 10^{34}\,\mathrm{cm}^{-2}\,\mathrm{s}^{-1}$). Um die daraus folgenden Zunahmen von Pile-up, Datenraten und Strahlendosen handhaben zu können, müssen die Detektoren der LHC-Experimente ebenfalls aufgerüstet werden (Phase-II upgrade). Aus diesem Grund wird der Spurdetektor des ATLAS-Experiments komplett durch einen neuen nur aus Siliziumdetektoren bestehenden Spurdetektor namens Inner Tracker (ITk) ersetzt werden. Es wurde bereits festgelegt, dass für den Pixel-Teil des ITk hybride Detektoren verwendet werden. Hauptsächlich wegen ihrer geringeren Herstellungskosten wurde zuvor auch der Einsatz monolithischer Pixelsensoren in Betracht gezogen. Unlängst finden diese vermehrt Anwendung in Teilchenphysikexperimenten. Im ITk wären sie für die äußerste Lage des Pixeldetektors verwendet worden, da sich hier die Kostenersparnis am größten ausgewirkt hätte.
Im Rahmen der hier vorliegenden Arbeit wurde ein hochspannungsbetriebener monolithischer aktiver Pixelsensor(HV-MAPS)-Prototyp charakterisiert und auf seine Tauglichkeit in Bezug auf die Verwendung für den ITk untersucht.

Abstract

The Large Hadron Collider (LHC) is planned to undergo a major upgrade, called the High-Luminosity LHC (HL-LHC), to fully exploit its physics potential until the end of its operation with an instantaneous luminosity of 5 to 7.5 times the design value ($1 \cdot 10^{34}\,\mathrm{cm}^{-2}\,\mathrm{s}^{-1}$). Consequently, the LHC experiments have to be upgraded as well (Phase-II upgrade) to be able to cope with the resulting increase in pile-up, data rates, and radiation doses. Therefore, the tracking detector of the ATLAS experiment, the Inner Detector, will be fully replaced by a new all-silicon tracking detector, the Inner Tracker (ITk). While it has been decided that only the baseline design of the pixel part of the ITk will be pursued, which forsees the use of hybrid pixel detectors, it has been worthwhile to study monolithic pixel sensor options as well, whose production is comparatively cost-efficient. Monolithic pixel sensors have recently made their way into particle physics experiments and they were considered as an alternative sensor option for the outermost pixel layer of the ITk. Within the scope of this thesis, a high voltage monolithic active pixel sensor (HV-MAPS) prototype, called ATLASPix_Simple, was characterized and studied regarding its suitability for the use in the ITk.

Contents

1 Introduction **11**

2 The HL-LHC and the ATLAS ITk upgrade **15**
2.1 The LHC 15
2.1.1 LHC operation timeline 15
2.1.2 HL-LHC 19
2.2 The ATLAS experiment 20
2.2.1 The ATLAS detector (before HL-LHC) 20
2.2.2 Upgrades of the ATLAS detector for the HL-LHC . . . 26
2.2.3 The ITk upgrade 28

3 Silicon pixel detectors **33**
3.1 Working principle 33
3.2 Readout electronics 38
3.3 Radiation damage to silicon detectors 42
3.3.1 Ionization effects 42
3.3.2 Silicon bulk damage 44
3.4 Particle tracking with silicon detectors 48
3.5 Silicon pixel detector technologies used in particle physics . . . 53
3.5.1 Hybrid pixel detectors 53
3.5.2 Monolithic pixel detectors 56

4 Introduction to ATLASPix1/ATLASPix_Simple **61**
4.1 Architecture of ATLASPix_Simple 63
4.1.1 Active pixel 64
4.1.2 Readout cells 67
4.1.3 Readout state machine 69
4.1.4 Timestamps 71

5 Characterization of ATLASPix_Simple **73**
5.1 Setups 73

5.1.1 Operation of a single sensor . . . 74
5.1.2 Reference time measurement . . . 78
5.1.3 Telescope setup . . . 79
5.1.4 Software . . . 81
5.2 Testbeam facilities . . . 84
5.2.1 DESY . . . 84
5.2.2 PSI . . . 84
5.3 Basic sensor performance . . . 85
5.3.1 Current-voltage characteristic . . . 85
5.3.2 Power consumption . . . 85
5.3.3 Influence of DAC settings on pulse shaping and power consumption . . . 87
5.3.4 Noise and threshold dispersion . . . 92
5.3.5 Efficiency . . . 95
5.3.6 Hit clusters . . . 102
5.3.7 Line crosstalk . . . 105
5.3.8 Time resolution . . . 111
5.4 Studies with sub-pixel resolution . . . 120
5.4.1 Description of DURANTA telescope setup and DAQ . . . 122
5.4.2 Software alignment, track fit, and pointing resolution . . . 123
5.4.3 Sub-pixel efficiency . . . 125
5.4.4 Sub-pixel studies of hit clusters . . . 130
5.4.5 Sub-pixel timing . . . 133
5.5 Studies on radiation tolerance . . . 136
5.5.1 Irradiated samples . . . 136
5.5.2 Cooling setup . . . 137
5.5.3 Leakage current after irradiation . . . 141
5.5.4 Threshold dispersion and SNR after irradiation . . . 143
5.5.5 Testbeam measurements . . . 145

6 ATLASPix_IsoSimple **155**

7 Conclusion **161**

Appendix **165**
A1 Default sensor configuration . . . 165
A2 Straight line fit formulae . . . 166
A3 Efficiency error calculation . . . 167

Chapter 1

Introduction

Our current knowledge about elementary particle physics is, on the one hand, represented by the theoretical model called the Standard Model of particle physics, which describes all known elementary particles and their interactions (excluding gravity), and which is consistently being confirmed by experiment. On the other hand, we observe phenomena that cannot be explained by the Standard Model, for example, dark matter, dark energy, and the excess of baryons over antibaryons in our observable universe.
A major driving force of todays research in the field of particle phyiscs is therefore the experimental search for new physics beyond the Standard Model that can explain the above phenomena. Physicists are either looking for deviations from the Standard Model predictions in the data of precision measurements or for previously unobserved signatures at the high energy frontier.
Both approaches rely a great deal on continuing technological progress in particle accelerator and detector technologies. After its greatest success as of yet, the discovery of the Higgs boson in 2012, and being in operation for more than a decade, the Large Hadron Collider (LHC), earth's most powerful particle accelerator, reached only about half of its planned runtime at the time this thesis is being written. To fully exploit its physics potential, the LHC will undergo a major upgrade, called the High-Luminosity LHC (HL-LHC), which is planned to be ready for operation in 2026.
Coping with the resulting, unprecedentedly challenging operating conditions requires upgrades of the detectors of the LHC experiments as well. A part thereof is the replacement of the tracking system of the ATLAS detector, the Inner Detector, by a completely new all-silicon tracking detector, called the Inner Tracker (ITk). It consists of a pixel detector, as its innermost component, surrounded by a silicon microstrip detector. Due to the high track density at the HL-LHC, the pixel detector becomes even more important to maintain or even improve the good performance of the ATLAS detector.

Consequently, the new pixel detector is designed to cover a significantly larger area than the one that is currently in operation.
With pixel detectors generally becoming larger in size and at the same time new monolithic pixel sensor technologies finding their way into particle physics experiments, it is worthwhile to consider taking advantage of the cost-efficient production of said monolithic pixel sensors compared to the well-established hybrid detectors. While the ATLAS experiment is pursuing only the ITk baseline design, which forsees hybrid detectors, several monolithic pixel sensor options were studied regarding their suitability for their use in the outermost pixel layer of ITk.
One of the prototypes produced for this purpose is a high voltage monolithic active pixel sensor (HV-MAPS) called ATLASPix_Simple. Its characterization in terms of efficiency, noise, time resolution, and radiation tolerance is the topic of this thesis.

Thesis outline

The thesis contextualizes the work that has been carried out within its scope by introducing the LHC and the ATLAS detector as well as their planned upgrades in chapter 2. Chapter 3 gives a summary of the working principle and characteristics of silicon pixel detectors as well as several examples of specific pixel sensor technologies used in particle physics. A description of the pixel sensor prototype characterized in this thesis, ATLASPix_Simple, is given in chapter 4. Chapter 5 represents the central part of the thesis. Section 5.1 describes the test setups that were used to perform the measurements presented in the thesis and section 5.2 briefly discusses the utilized testbeam facilities. While sections 5.3 and 5.4 present results on the performance of unirradiated samples, section 5.5 focuses on studies on radiation tolerance. In chapter 6, the performance of a similar sensor prototype is compared to that of ATLASPix_Simple. Chapter 7 concludes the thesis.

Contributions from the author

The author was not involved in the design of ATLASPix1, which was done by the ASIC and Detector Laboratory at the Karlsruhe Institute of Technology. The test setups (hardware, software, and firmware) used within the scope of this thesis to perform measurements with ATLASPix_Simple were developed by members of the Heidelberg Mu3e group. The author designed the insert PCB for ATLASPix1 and modified the configuration and DAQ software to enable the use of ATLASPix_Simple and ATLASPix_IsoSimple.
The commissioning of ATLASPix_Simple (with the Heidelberg test system)

was performed by the author.
All measurements of the power consumption and analog performance of ATLASPix_Simple (sections 5.3.2 and 5.3.3) as well as laboratory measurements of the time resolution of ATLASPix_Simple and ATLASPix_IsoSimple (parts of section 5.3.8 and chapter 6) were carried out and the corresonding data was analyzed by a Master student in the Heidelberg Mu3e group. The results were presented first in the corresponding Master thesis [69] and are summarized here. The corresponding results are highlighted again by a prefacing statement at the beginning of each of the respective sections.
All other laboratory measurements with ATLASPix_Simple presented in this thesis were carried out by the author.
Within the scope of this thesis, measurements with ATLASPix_Simple were performed at eight testbeam campaigns, of which several were co-organized by the author. While testbeam campaigns are a collaborative effort and at all of the campaigns different sensor types were tested, the author was responsible for all testbeam measurements with ATLASPix_Simple.
The author co-organized the irradiation campaigns discussed in this thesis and made significant contributions to the design and construction of the cooling system used for irradiated samples.
The software for the analysis of testbeam data used within the scope of this thesis was developed within the Heidelberg Mu3e group and modified by the author for the analyses presented in chapters 5 and 6, which were all performed by the author.

Chapter 2

HL-LHC and the ATLAS ITk upgrade

2.1 The LHC

The Large Hadron Collider (LHC) is Earth's most powerful particle accelerator up to date. It was built by the European Organization for Nuclear Research (CERN) (see figure 2.1 [1]) and its operation started in 2008. Since then, it has been pushing boundaries both at the high-energy and the high-intensity frontier. In the year 2012, one of the LHC's major physics goals was achieved with the discovery of a new particle [2, 3], whose properties are consistent with the Higgs boson, which previously had been the last unobserved elementary particle predicted by the Standard Model (SM) of particle physics. The discovery was made independently by the ATLAS and the CMS experiment, which both operate similar general-purpose detectors [4, 5]. In total, there are seven LHC experiments located at the 27 km long accelerator ring, with the remaining five being LHCb, ALICE, TOTEM, LHCf, and MoEDAL, which use detectors tailored to probe more specific phenomena, e.g. the quark-gluon plasma and b-physics.

2.1.1 LHC operation timeline

The LHC accelerates protons or heavy ions in two beam lines inside the 27 km long ring and collides them with a bunch crossing frequency of 40 MHz (for protons). In 2009, protons were accelerated with the LHC for the first time to energies unprecedented in human-built particle accelerators. The LHC research programme began in 2010 with Run 1 at a proton-proton center-of-mass energy of 7 TeV. Also in 2010, the first run with lead-lead collisions took place, based on which the ALICE collaboration reported the creation of a

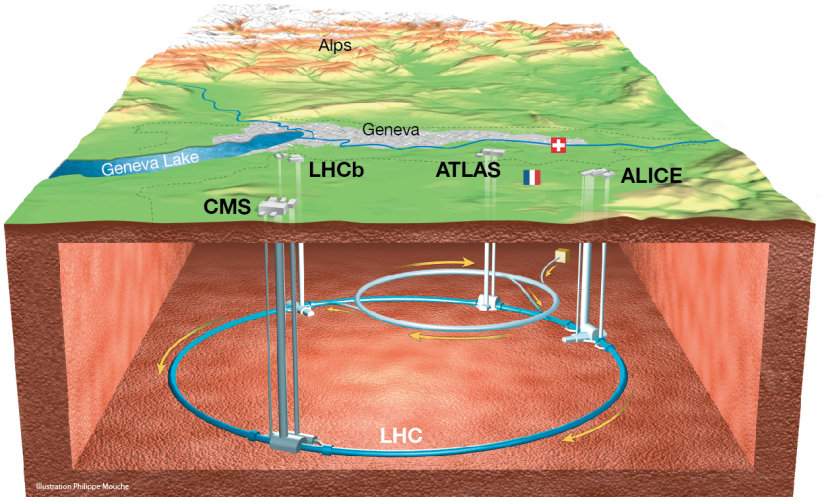

Figure 2.1: Overall view of the LHC [1]

quark-gluon plasma in 2011. The LHC has been the highest-luminosity (see below) hadron accelerator since 2011. The discovery of a new particle with a mass in the range of 125 to 126 $\mathrm{GeV/c^2}$, potentially the SM Higgs boson, in 2012 has been the major success of the LHC so far. Further physics results from Run 1, which ended in 2013, include for example the observation of several exotic hadronic states consitent with penta- [6] and tetraquarks [7] by the LHCb collaboration. Run 2 lasted from 2015 to 2018 with a center-of-mass energy for proton-proton collisions of 13 TeV. A peak luminosity of ca. $2.1 \cdot 10^{34}\,\mathrm{cm^{-2}\,s^{-1}}$ was achieved, which corresponds to two times the design value. The LHC's remaining runtime serves the purpose of collecting a large data set with Run 3, scheduled for 2021 to 2023, and afterwards with the HL-LHC (see section 2.1.2). Figure 2.2 [8] shows a long term schedule for the LHC operation including luminosity predictions for Run 3 and the HL-LHC.

Luminosity

The (instantaneous) lumiminosity $\mathcal{L}$ is a measure of the number of particles that take part in collisions per unit time. Multiplying it with a cross section σ_{cs}, a measure of the probability of a certain process to occur when particles collide, yields the expected rate of interactions N of the kind of the corresponding process:

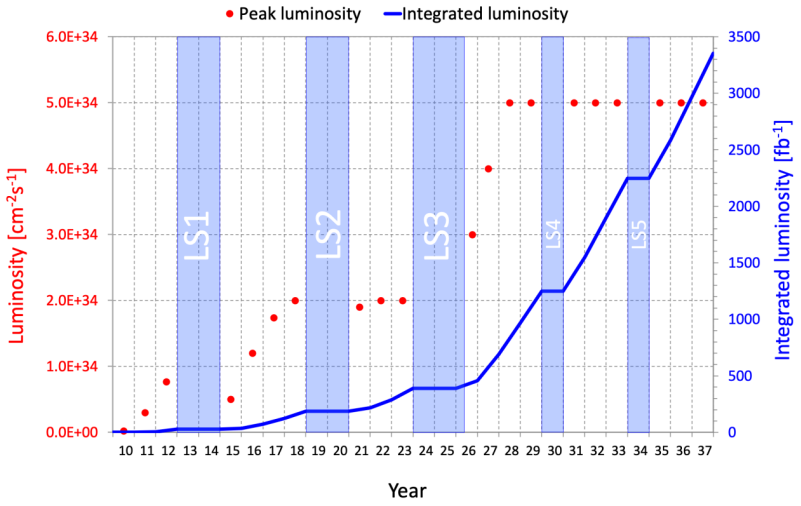

Figure 2.2: Long term schedule of the LHC operation including luminosity predictions for Run 3 and HL-LHC, using the nominal value for the instantaneous luminosity of the HL-LHC [8]

$$\frac{\mathrm{d}N}{\mathrm{d}t} = \sigma_{\mathrm{cs}} \cdot \mathcal{L} \tag{2.1}$$

To quantize the accumulated number of events in a collider over the course of its operation, one usually quotes the integrated luminosity, which relates to the expected total number of interactions N_{total} as follows:

$$N_{\mathrm{total}} = \sigma_{\mathrm{cs}} \cdot \underbrace{\int \mathcal{L}\,\mathrm{d}t}_{\text{integrated luminosity}} \tag{2.2}$$

$\mathcal{L}$ depends on the number of particle bunches inside the ring, the bunch population, the revolution frequency, and geometrical effects due to the bunches being extended objects colliding under an angle.
The LHC was designed to have 2808 bunches per beam, each including $1.15 \cdot 10^{11}$ protons. At the design luminosity of $\mathcal{L} = 1.0 \cdot 10^{34}\,\mathrm{cm}^{-2}\,\mathrm{s}^{-1}$ the average number of interactions per bunch crossing (pile-up) was recorded to be $\langle \mu \rangle = 27$.

Acceleration stages

Before protons or ions are accelerated in the LHC, they undergo a series of pre-acceleration steps. The protons are initially gained by removing electrons

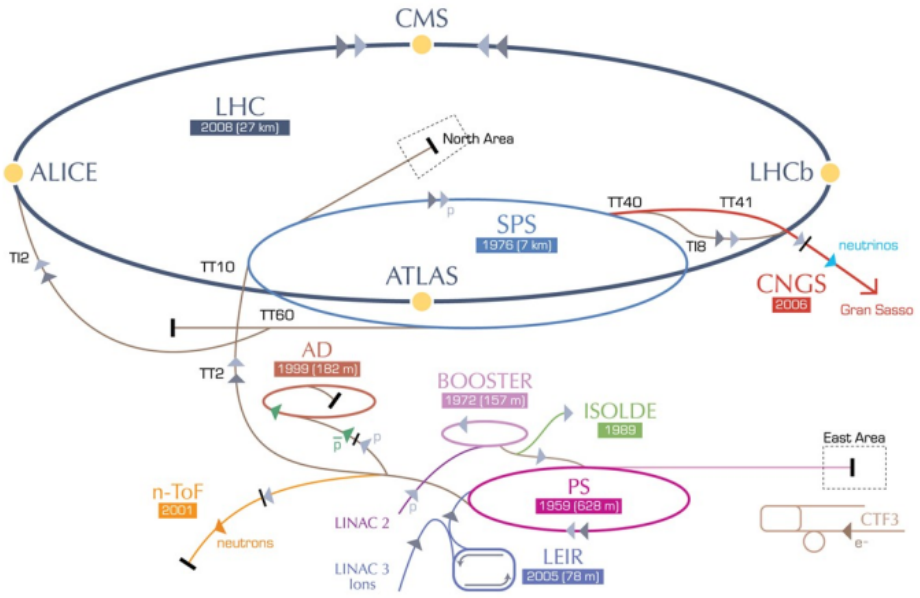

Figure 2.3: Layout of the CERN accelerator complex [10]

from hydrogen atoms using an electric field. They are first accelerated to an energy of 50 MeV with a linear accelerator called Linac 2. Starting from here, the proton beam is injected successively into three synchrotrons. The Proton Synchrotron Booster (PSB) accelerates the protons to an energy of 1.4 GeV, which significantly increases the number of protons that can be filled into the Proton Synchrotron (PS). The latter delivers different kinds of particles directly to experiments or to more powerful accelerators. For an LHC fill, protons with the maximum possible energy of 25 GeV are delivered to the Super Proton Synchrotron (SPS), where they are accelerated to an energy of 450 GeV before they are finally injected into the two beampipes of the LHC. It takes about 4 minutes to fill the LHC and 20 minutes to accelerate protons to 6.5 TeV. The two beams circulate for many hours in opposite direction while being brought to collision at the four points where the main experiments are located. For lead runs of the LHC, lead ions are accelerated in Linac 3, collected in the Low Energy Ion Ring (LEIR), and then follow the same steps as protons starting with PS [9]. Figure 2.3 [10] shows a layout of the CERN accelerator complex.

2.1.2 HL-LHC

The High-Luminosity LHC (HL-LHC) [11] is a planned luminosity upgrade of the LHC, scheduled to start operation in 2026. Its purpose is to fully exploit the physics potential of the LHC until the end of its lifetime. The nominal value for the peak luminosity of the HL-LHC is $5.0 \cdot 10^{34}\,\mathrm{cm}^{-2}\,\mathrm{s}^{-1}$, i.e. five times the LHC's initial design luminosity. The aim is to accumulate about $3000\,\mathrm{fb}^{-1}$ of integrated luminosity at a center-of-mass energy of 14 TeV in about 12 years, which is approximately 10 times the integrated luminosity of the LHC's first 12 years of operation. Design margins should even allow for a peak luminosity of up to $7.5 \cdot 10^{34}\,\mathrm{cm}^{-2}\,\mathrm{s}^{-1}$ [11].
Collecting a data set with large integrated luminosity is essential for significantly increasing the precision for measurements of SM processes and the sensitivity for new physics in direct and indirect searches [12]. The HL-LHC physics programme includes extensive studies of the Higgs boson properties, e.g. the Higgs self-coupling [13], searches for heavy resonances, supersymmetry, and dark matter signatures [14], as well as probes in many sectors of flavor physics [15].
The key target variables to achieve the luminosity increase are the following [11]: The beam current is planned to be increased to 30 % above the LHC's ultimate design value of 0.86 A, requiring all the available beam pipe cooling power.
The number of protons per bunch is supposed to increase by a factor of two while the transverse emittance[1] must be kept at low value. This point concerns all acceleration stages, starting with the beam generation.
Decreasing the transverse size of the beam at the nominal collision point requires modified and more powerful final focussing magnets.
The use of so-called RF crab cavities is planned, which generate a high transverse electric field that rotates the bunches in the crossing plane to increase their overlap during collision.
The bunch crossing frequency will be kept at 40 MHz.
To carry out the HL-LHC physics programme, the detectors of the LHC experiments need to be upgraded as well (Phase-II upgrade programme). They need to maintain or improve their performance while dealing with increased occupancies and data rates, an expected pile-up of up to $\mu = 200$, and a harsh radiation environment.
The following section first introduces the ATLAS detector and subsequently discusses its upgrade for the operation at the HL-LHC with focus on its

[1] The emmitance is a measure of the beam's average spread in position and momentum space. While the transverse size, measured by the so-called β-function, changes along the beam, e.g. due to focussing magnets, the emittance stays constant.

innermost component, the pixel detector.

2.2 The ATLAS experiment

The ATLAS experiment is one of the four main experiments at the LHC and one of two general-purpose experiments. Its detector is built around one of the LHC's four collision points. To meet the challenges of the HL-LHC, the detector requires a major upgrade, the so-called Phase-II upgrade, which is discussed in section 2.2.2. Section 2.2.1 describes the ATLAS detector before the upgrade.

2.2.1 The ATLAS detector (before HL-LHC)

The ATLAS detector is built such that it covers a large fraction of the solid angle around the collision point. It consists of a stack of several types of particle detectors arranged as a barrel part around the beam axis, with the collision point in the center, and so-called end-caps located up- and downstream of the collision point. An image of the whole detector is shown in figure 2.4 [16]. In the following, the individual sub-detectors, the magnet system, and the trigger and data acquisition scheme are described.

The Inner Detector

The innermost part of the ATLAS detector is the so-called Inner Detector [17], which is used for track and vertex reconstruction. By performing precise measurements of several space points along the trajectory of a charged particle in the presence of a known magnetic field, one can determine the track's curvature and therefore the particle momentum (see section 3.4).
The Inner Detector comprises three sub-detectors, a pixel detector, which is the closest to the collision point, followed by a silicon strip detector (SCT), and a transition radiation detector (TRT) on the outside. An image of the Inner Detector is shown in figure 2.5 [18].

Pixel detector: The pixel detector provides the high granularity required close to the collision point to reconstruct primary vertices as well as secondary vertices corresponding to the decays of long-lived particles such as mesons including b-quarks. The initial pixel detector consists of three barrel layers at radii of 50.5 mm, 88.5 mm, and 122.5 mm, all with a length of two times 400.5 mm as well as end-cap disks at distances from the collision point of 495 mm, 580 mm, and 650 mm. The pixel size is $50 \times 400\,\mu\text{m}^2$. Being located

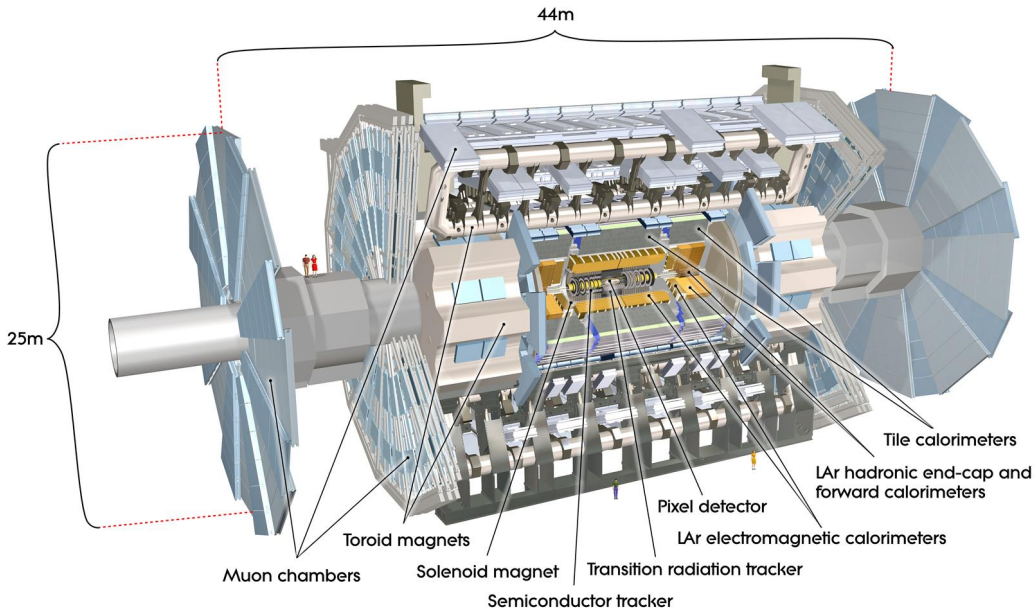

Figure 2.4: Image of the whole ATLAS detector (before Phase-II upgrade) [16]

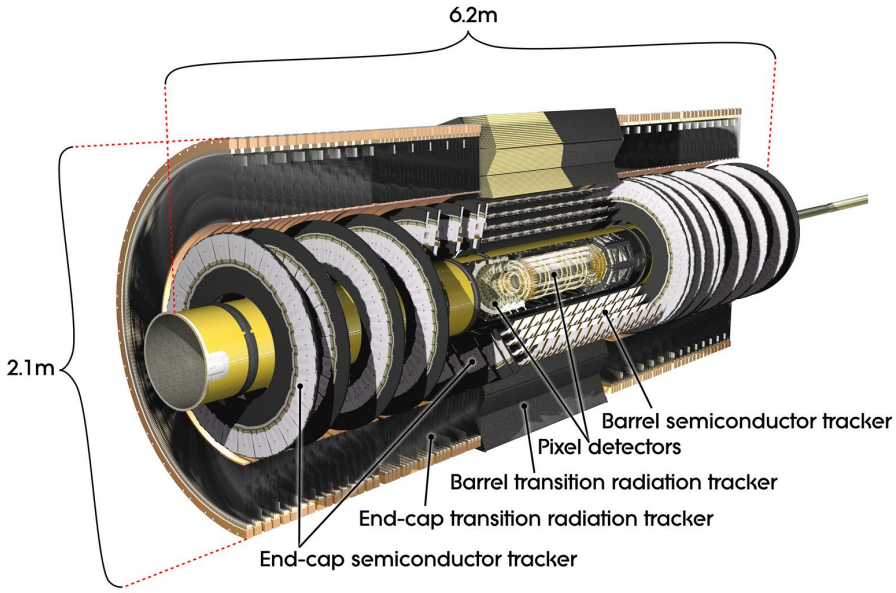

Figure 2.5: Image of the ATLAS Inner Detector [18]

this close to the collision point, the pixel detector is exposed to a significent radiation dose. To increase radiation tolerance (see section 3.3.2), the sensors are fabricated from oxygenated substrate [19] and the bias voltage can be increased from 150 V up to 600 V to compensate for the substrate degradation over time. Furthermore, a small gate oxide thickness and special layout techniques are used in the design of the readout ASIC to increase its radiation tolerance. The pixel detector is operated at a temperature between $-5\,°C$ and $-10\,°C$ to reduce the leakage current (see sections 3.1 and 3.3.2).

Insertable B-Layer: The insertable B-Layer (IBL) [20] is an innermost fourth pixel barrel layer that was added later on (in 2014) at a radius of 33 mm. It represensts the first large scale application of 3D sensors (see section 3.5.1) and CMOS 130 nm technology. The IBL was installed to prevent efficiency loss, especially in the tagging of b-quark decays, due to radiation damage at increased luminosity. The IBL provides redundancy and higher precision. The pixel size is reduced to $50 \times 250\,\mu m^2$ and a faster readout ASIC is used to cope with higher occupancies. The 3D sensor technology has been proven to have a very high radiation tolerance (see section 3.5.1). A new CO_2-based cooling system is used together with the IBL.

Semiconductor Tracker: Further away from the collision point, silicon microstrips are used instead of pixels with the strips running parallel to the beam axis. The corresponding sub-detector is called Semiconductor Tracker (SCT). Its geometry is similar to that of the pixel detector. There are four barrel layers and each end-cap consists of nine disks. Barrels and disks are covered with strip sensors on both sides. The detector is located at radii between 30 cm and 55 cm and extends to 2.8 m on both sides of the collision point.

Transition Radiation Tracker: The Transition Radiation Tracker (TRT) combines the extension of the tracking detectors outwards up to the solenoid magnet with the capability of standalone electron identification. It consists of more than 300,000 straw tubes with a diameter 4 mm oriented in parallel to the beam axis in the barrel region and radially in the end-cap region. In the center of each tube, there is a gold-plated tungsten wire with a potential difference to the wall of 1500 V. The tubes are filled with a gas mixture containing 70 % of Xe.
A traversing charged particle ionizes the gas. The resulting free electrons drift to the wire and create a signal. Typically, there are more than 30 hits per track.

The space between the straw tubes is filled with polymer fibres (barrel) and foils (endcaps) to create transition radiation, for which the probability increases with the traversing particle's relativistic γ-factor. The latter is larger for an electron than for a heavier particle with the same energy. The corresponding photons can be absorbed by the Xe leading to photoemission and consequently to an enhancement of the signal in the straw tube. By comparing the signals to an additional high threshold, electrons can be separated from heavier particles.

Magnets

Strong magnetic fields are required to bend the tracks of charged particles to determine their momentum (see section 3.4). The ATLAS detector features two types of superconducting magnets [21].
The Inner Detector is surrounded by a solenoid with an inner diameter of about 2.5 m. It creates a 2 T magnetic field parallel to the beam axis.
The magnetic field in the muon spectrometer is created by three large scale air-core toroids, one in the barrel region and one on each side to close the field in the end-cap regions. They create fields inside the muon detectors of approximately 0.5 T and 1.0 T, respectively. The outer dimensions of the barrel toroid are approximately 20 m and 25 m.

Calorimeters

Particle energies are measured with two types of calorimeters. A liquid argon (LAr) calorimeter [22] is used to measure the energy of electromagnetic showers and tile [23] and LAr calorimeters are used to measure the energy of hadronic showers. In the drawing shown in figure 2.6 [24], the calorimeters are highlighted. They are all sampling calorimeters, i.e. they are made of alternating layers of material that produces particle showers and material that is used to measure deposited energy.

Electromagnetic calorimeter: Seen from the inside out, first comes the electronic calorimeter. This detector consists again of a barrel part and two end-caps. They are made from lead plates with thicknesses between ca. 1 mm and 2.5 mm, in which electromagnetic showers are produced, and LAr, which fills the ca. 4 mm wide gaps between the lead. A traversing particle ionizes the LAr and the resulting free electrons drift towards an electrode in the middle of the gap. The LAr calorimeter is designed such that it fully contains all electromagnetic showers. Going outwards, the granularity gets coarser. The LAr has to be kept at a temperature of 88 K. It shares its

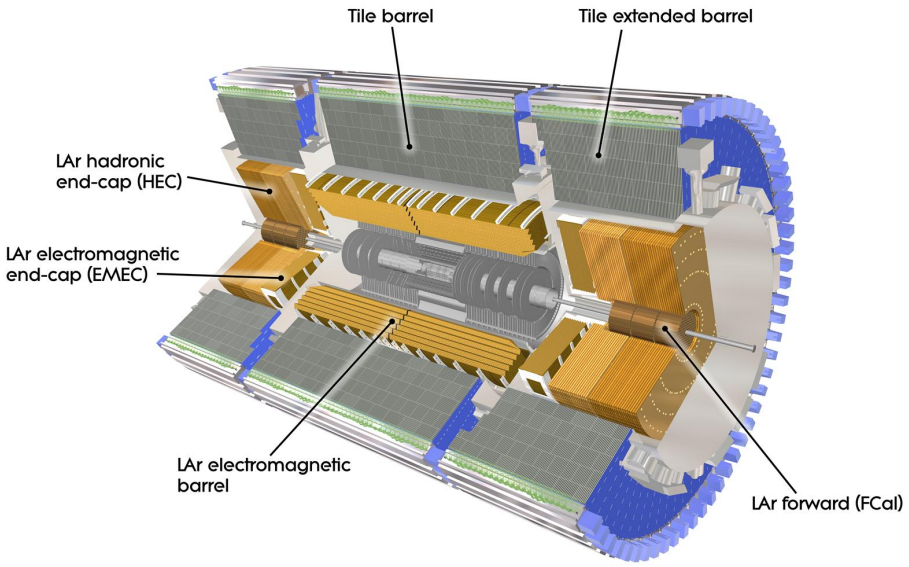

Figure 2.6: Image of the ATLAS calorimeters [24]

cooling infrastructure with the solenoid magnet to minimize the amount of material in front of the hadronic calorimeter.

Hadronic calorimeter: The hadronic calorimeter consists mostly of an extended barrel part. Hadronic showers are produced in steel plates with thicknesses between 4 mm and 5 mm. 3 mm thick scintillators are used as active material. They consist of polysterene doped with fluorine and they are read out by photomultiplier tubes that are connected via optical fibres. The end-cap parts of the hadronic calorimeter is again a LAr calorimeter, which uses 20 mm to 50 mm thick copper plates to create showers.

Additional LAr calorimeters, called FCal, are used in the very forward regions.

The Muon spectrometer

The outermost sub-detector is the muon spectrometer [25]. It starts at a radius of $\sim$ 4.25 m end extends to a radius of $\sim$ 11 m. Muons are the only detectable particles that pass through the hadronic calorimeter, at least in the central detector region. They get deflected in the magnetic field that is created by the air-core toroid magnets mentiond above to measure their

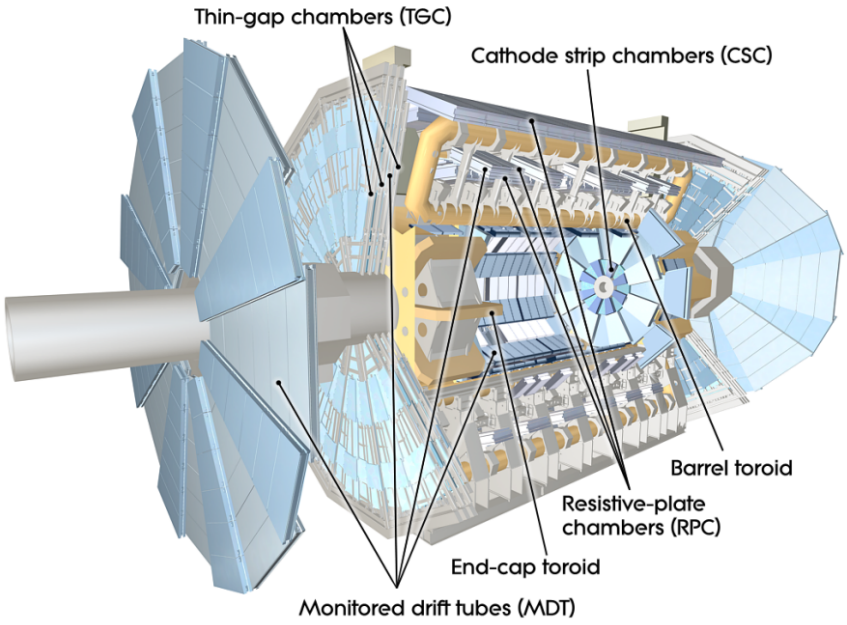

Figure 2.7: Image of the ATLAS muon spectrometer [26]

momentum. The muon spectrometer consists of several components, which are shown in figure 2.7 [26]. The tracking is performed using Monitored Drift Tubes (MDT), whose position has to be known with high precision, and in the forward region, where the density of charged particle tracks is higher, multi-wire proportional chambers, called Cathode Strip Chambers (CSC). In addition, resistive plate chambers (RPC) are used in the central region for fast measurements used for triggering. In the end-cap region another set of multi-wire proportional chambers is used, called Thin-gap Chambers (TGC). They, too, provide fast signals used for triggering as well as a measurement of the track coordinate that is not relevant to determine the curvature of the muons and therefore not covered by the MDT measurement.

Forward detectors

ATLAS features two types of forward detectors for luminosity and total cross section measurements [27]:

LUCID: Two quartz fibre Cherenkov detectors, called LUCID, are placed around the beampipe at a distance of about 17 m from the collision point, one on each sides of the experiment. They are used as luminosity monitors.

ALFA: The ALFA Roman Pot detectors are located in the LHC tunnel at an approximate distance of 240 m from the collision point on both sides of the experiment. They are scintillating fibre detectors, designed to measure the elastic proton scattering at very small angles.

The trigger system

The ATLAS detector produces data at an event frequency of 40 MHz, where an event corresponds to one collision of proton bunches. With an event size of $\mathcal{O}(1\,\mathrm{MB})$, this results in a data rate that is too high to be written to mass storage. It is the task of the trigger system to reduce the rate of events to be stored for later analysis to approximately 1 kHz. To achieve this, it has to decide within $\mathcal{O}(1\,\mathrm{s})$ upon the occurance of an event if it is interesting enough to store it or not.
Since Run 2, the ATLAS trigger system has had two stages. The first trigger level (L1) is implemented in hardware. It uses only part of the full detector information to reduce the rate of events to be processed further from 40 MHz to approximately 100 kHz.
Events accepted by L1 are processed by a software-based so-called high-level trigger (HLT) [28], which makes the final trigger decision. The HLT runs a sequence of algorithms on event data, including for example online event reconstruction within a geometrical region of interest (RoI), which si defined by L1, and searches for certain objects like leptons or jets.

2.2.2 Upgrades of the ATLAS detector for the HL-LHC

The ALTAS detector will undergo a major upgrade to meet the challenges of the new operating conditions at the HL-LHC, which include increased pile-up, occupancies, and data rates, as well as exposure to large doses of radiation.
All sub-detectors as well as the trigger and data acquisition system are subject to the upgrade:

Tracking: One of the largest changes is the replacement of the complete Inner Detector by an all silicon tracking detector called Inner Tracker (ITk), which is covered in a dedicated section below (2.2.3).

Muon spectrometer: The MDT chambers will be integrated into the new level-0 trigger (see below) and readout and trigger electronics of the

sub-systems used for triggering will be exchanged with new electronics that is capable of handling higher rates and larger latencies. The power system for the RPC, TGC, and MDT chambers and electronics will need to be replaced due to component obsolescence, ageing, and radiation damage. RPC chambers will be installed in the inner barrel layer to increase the acceptance and robustness of the trigger. MDTs in this region will be replaced by new small-diameter MDTs to make space for the RPCs. Some old RPCs in high-rate regions will be refurbished. Some TGCs will be replced by ones with better background-suppression capabilities. The innermost parts of the end-caps, SCSs and MDTs, will be replaced by Micromegas and small-strip TGCs. [29]

LAr calorimeter: The current LAr calorimeters themselves are expected to achieve a good performance also over the period of the HL-LHC, with signal degradations only expected in the FCal. However, all existing readout and trigger electronics, on- and off-detector, will have to be replaced to adapt to the new overall trigger architecture and the new requirements in terms of radiation tolerance. [30]

Tile calorimeter: It is not planned to change the scintillating tiles and fibres, or all the PMTs. The old first-level calorimeter trigger uses analog signals with reduced granularity. This system will be replaced and the full digital tile information will be sent to the trigger system at 40 MHz. With the corresponding new bandwith capability, the trigger buffers storing the full event data can also be moved off-detector, decreasing the risk of single event upsets (SEU) in the new radiation environment. Accessibility for maintenance must be optimized for compliance with radio-protection rules at increased activation. [31]

Trigger and data acquisition system: The system will be redesigned to a large degree. The baseline foresees a single Level-0 hardware trigger that accepts events with a rate of 1 MHz and a maximum latency of 10 µs based on calorimeter and muon information. Its processors include updated versions of the calorimeter trigger processors and complementary ones that will implement more sophisticated, offline-like algorithms. The higher-level trigger system is called Event Filter (EF). It consists of a CPU-based processing farm, which is complemented by a hardware-based tracking processor, called HTT. The event filter is capable of regional and global track reconstruction and refines trigger objects, while rejecting events as early as possible during their processing. It reduces the rate of accepted events to approximately

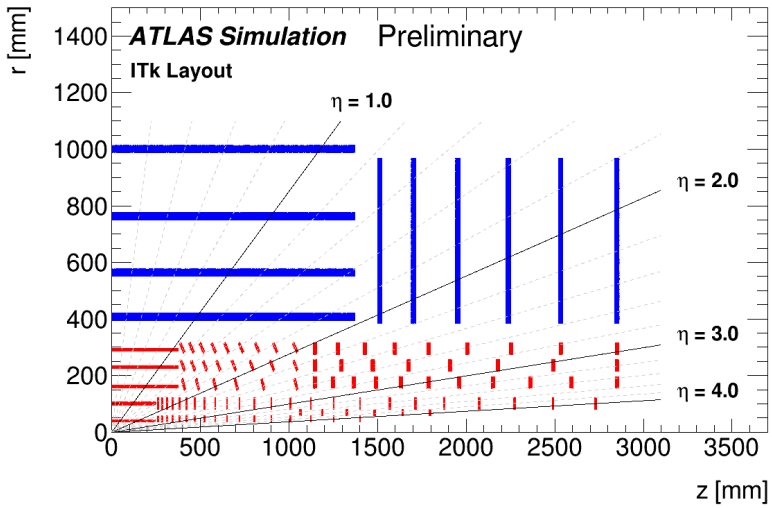

Figure 2.8: Schematic showing one quarter of the ITk layout, cut along the beam axis, with the nominal collision point in the bottom left corner [37]

10 kHz, which is the event rate for permanent storage. [32]

The high-granularity timing detector: A high-granularity timing detector (HGTD) will be installed inside the gaps between the ITk and the LAr calorimeter end-caps to resolve pile-up in the forward region. Its design is based on the detector technology of low gain avalanche diodes (LGADs), which can achieve a time resolution of down to 30 ps. Benefits in forward object reconstruction as well as online and offline luminosity determination are expected. [33]

2.2.3 The ITk upgrade

For operation at the HL-LHC, the inner tracking system of the ATLAS detector will be replaced. By the end of Run 3, the existing components will have reached the end of their lifetime due to radiation damage. Furthermore, they were not designed to operate under HL-LHC conditions. The newly designed system is an all silicon tracking detector, called Inner Tracker (ITk), which offers higher granularity, increased solid angle coverage, a higher readout bandwidth, and an expected higher radiation tolerance compared to the old Inner Detector. The operation of a TRT is not feasible anymore because its occupancy would be too large [34].
Figure 2.8 [37] illustrates the - at the time of writing - latest iteration of the ITk layout. The strip detector consists of four strip module layers in the

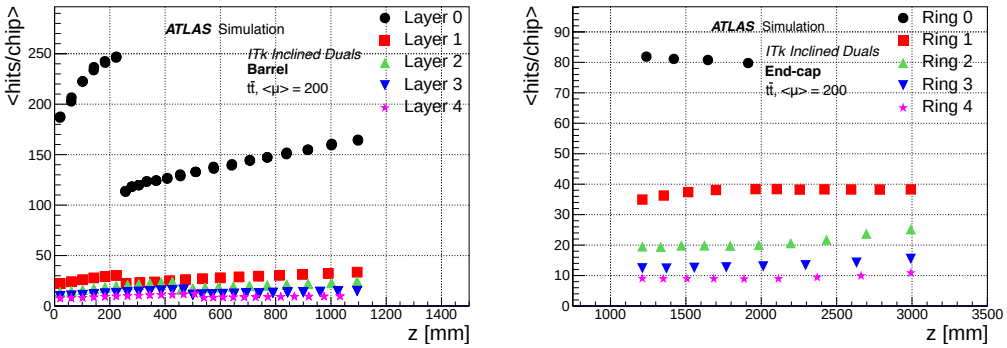

(a) Barrel (b) End-cap

Figure 2.9: Simulated number of hits per chip and bunch crossing vs z-position in the barrel region (a) and the end-cap region (b) for the ITk pixel detector [36]

barrel region and six disks per end-cap. The pixel detector consists of five flat barrel layers, extended by inclined and vertical rings in forward direction. The new strip detector covers and area of roughly $165\,\mathrm{m}^2$, 2.5 times the area of the old one, and has nearly ten times as many electronics channels (roughly 60 million) [35]. The radius of the outermost layers is ca. 1 m.
The number of pixel layers and the outer radius of the pixel detector have increased to make more use of the finer granularity of pixels compared to strips.
The ITk is expected to perform as good and in many cases better than the Inner Detector, but in a much more difficult tracking environment [35].
Figure 2.9 [36] shows simulation results for the number of hits per chip and bunch crossing plotted against the position along the beam axis (z) for the five pixel layers in the barrel region (a) and the end-cap region (b). $\mathrm{t\bar{t}}$-events with a pile-up of 200 are used. The simulated chip size is ca. $380\,\mathrm{mm}^2$. Note that the layout used in [36] is slightly different from the one presented above and the detector model does not yet include all services and support structures [37]. At the time of writing, it is still under discussion if the pixel size will be $50 \times 50\,\mu\mathrm{m}^2$ or $25 \times 100\,\mu\mathrm{m}^2$.

Figure 2.10 [36] shows the simulated NIEL fluence (a) and total ionizing dose (b) (see section 3.3) distributions for the pixel detector for an integrated luminosity of $4000\,\mathrm{fb}^{-1}$. The baseline design for the pixel detector foresees to replace the two innermost layers after half the runtime of the HL-LHC. Table 2.1 [36] shows the simulated maximum lifetime fluences and ionizing doses in different regions of the pixel detector for the above scenario, i.e half

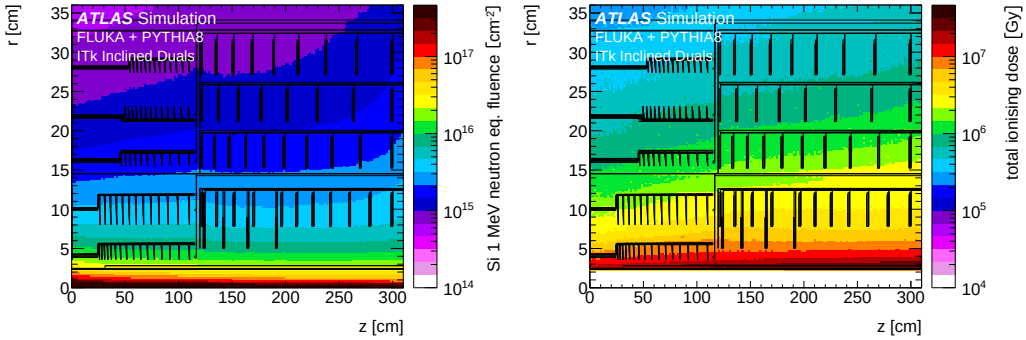

(a) NIEL fluence (b) Total ionizing dose

Figure 2.10: Simulated NIEL fluence (a) and total ionizing dose (b) distributions for the ITk pixel detector for an integrated luminosity of 4000 fb^{-1} [36]

the integrated luminosity is assumed for Layer 0 and Layer 1 compared to the other layers. These results were multiplied by a safety factor of 1.5.

Monolithic pixel options

The baseline design of the pixel part of ITk foresees hybrid pixel detectors (see section 3.5.1). Such detectors don't have a large commercial market outside of particle physics and their production cost and time are comparatively large. Therefore, alternative monolithic pixel technologies were considered for the outermost pixel layer. Here, the potential for cost reduction is the highest because, out of all pixel layers, it covers the largest area. The cost advantage was estimated to be 6.5 % of the total costs of the pixel upgrade plus half the common costs shared with the strip upgrade [38], assuming a drop-in design. The latter denotes a design where only the sensor and the readout ASIC are replaced by a monolithic chip while all other detector components (module support structure, readout infrastructure, cooling system, etc.) are kept the same as for the baseline design.
The main requirements for the monolithic pixel options are the same as for the baseline option for the outermost pixel layer. A radiation tolerance up to a NIEL fluence of ca. $1 \cdot 10^{15}\,\mathrm{n_{eq}/cm^2}$ and a TID of ca. $5 \cdot 10^5$ Gy are required (see figure 2.10). The maximum accepted noise rate is specified as 10^{-6} per pixel and bunch crossing, i.e. 40 Hz per pixel. Efficiency and time resolution should be as good as possible while definite requirements are not formulated in the pixel part of the ITk Technical Design Report (TDR) [36]. Studies on the tracking performance are carried out assuming 99 % and 97 % efficiency.

Luminosity	Layer	Region	Fluence / $10^{14}\,n_{eq}/cm^2$	Dose / MGy
$2000\,fb^{-1}$	0	flat barrel	131	7.2
		inclined barrel	123	9.9
		end-cap	68	6.3
$2000\,fb^{-1}$	1	flat barrel	27	1.5
		inclined barrel	35	2.9
		end-cap	38	3.2
$4000\,fb^{-1}$	2 - 4	flat barrel	28	1.6
		inclined barrel	30	2.0
		end-cap	38	3.5

Table 2.1: Simulated maximum NIEL fluences and total ionizing doses for different regions of the ITk pixel detector, multiplied by a safety factor of 1.5 [36]

The second value is a lower limit and the baseline technologies are expected to perform better than that until the end of their lifetime.
The time resolution should be good enough to be able to match hits to the bunch crossing in which they occur. To be able to do this for 99 % of all hits at a bunch spacing of 25 ns (assuming a 100 % time-independent detection efficiency) requires a time resolution of $\sigma \approx 4.8\,ns$[2].
Two monolithic sensor technologies were under consideration. One of them is based on a small collection electrode and full lateral depletion is achieved by a lightly-doped n-type implant inside the p-type substrate (see section 3.5.2). The other technology is based on a large collection electrode and a large reverse bias voltage ($\sim -100\,V$), hence it is called high voltage monolithic active pixel sensor (HV-MAPS) technology (see section 3.5.2). Prototypes exist for both technologies. The first HV-MAPS prototype specifically produced to demonstrate the feasibility of the HV-MAPS technology for the ITk upgrade is ATLASPix1, which comes in three variants. The characterization of one of them, ATLASPix_Simple, is the subject of this thesis.

[2] σ is defined here as one standard deviation of a normal distribution.

Chapter 3

Silicon pixel detectors

Silicon pixel detectors make use of the semiconductor properties of silicon to detect ionizing particles. They have high granularity, are compact, and their production benefits from the high standards of the semiconductor industry. Besides applications in, for example, digital cameras and clinical imaging, silicon pixel detectors are used in particle physics experiments as tracking and vertex detectors.

3.1 Working principle

An ionizing incident particle loses energy inside the silicon bulk by creating free electron-hole pairs. An electric field forces free charge carriers to drift towards an electrode, which induces a current according to the Shockley-Ramo theorem [39, 40]. This current charges the detector capacitance C and the resulting voltage can be measured.
Silicon pixel detectors use a reversely biased p-n junction as their basic sensing element.

The p-n junction

A p-n junction is the interface between a p-type and an n-type semiconductor. A p- or n-type semiconductor is created by doping, i.e. the deliberate introduction of impurities into the crystal structure. It changes a semiconductor's electrical properties by introducing allowed energy states inside the gap between the valence and the conduction band. An n-type semiconductor is doped with atoms that have more valence electrons than those of the pure semiconductor. This creates energy states close to the conduction band such that the dopant atoms have a high probabilty of being thermally ionized,

which creates an excess of free electrons in the valence band. Such impurities are therefore called electron donors. A typical n-type dopant for silicon is for example phosphorus. Analogously, a p-type semiconductor is doped with atoms that have less valence electrons than the atoms of the pure semiconductor, which represent so-called electron acceptor impurities that create energy states close to the valence band. The result is an excess of free holes. A typical p-type dopant for silicon is for example boron.
For silicon detectors, an essential property of the p-n junction is that it becomes depleted of free charge carriers, making it almost non-conductive. The excess of charge carriers - electrons in the n-type and holes in the p-type semiconductor - leads to their diffusion towards the respective opposite side of the junction, where they recombine with carriers of the opposite charge. This leaves a negative space charge region on the p-type side and a positive space charge region on the n-type side, which results in an electric field acting against the diffusion process and ultimately to an equilibrium state. There are no free charge carriers left in the so-called depletion region. Assuming box shaped charge distributions, the resulting electric field and electric potential have the shapes illustrated in figure 3.1. Note that the electric potential drawn here as well as in figure 3.2 (denoted as "Voltage") can be regarded as the lower edge of the conduction band or the upper edge of the valence band. The electric potential difference that develops across the junction when there is no additional external voltage applied is called the build-in voltage U_{bi}.

Characteristics of the p-n junction

A p-n junction is a diode, i.e. it conducts primarily in one direction. Depening on the polarity of a voltage that is applied to a p-n junction externally, one distinguishes between forward and backward bias (see figure 3.2).
When the positive pole is connected to the p-type region and the negative pole to the n-type region, the junction is in forward bias. The corresponding potential difference has the opposite polarity of that across the unbiased p-n junction. The resulting potential difference across the junction is smaller than in the unbiased case or even switches sign. Consequently, also the electric field and the width of the depletion region are smaller. With increasing bias voltage, ultimately, the depletion region becomes small enough to allow current flow of minority charge carriers across the junction.
The junction is in reverse bias when the negative pole is connected to the p-type region and the positive pole to the n-type region. In this case, the resulting potential difference across the junction is larger than in the unbiased case. Hence, the electric field and the width of the depletion region have to be larger. A very small reverse leakage current flows across the junc-

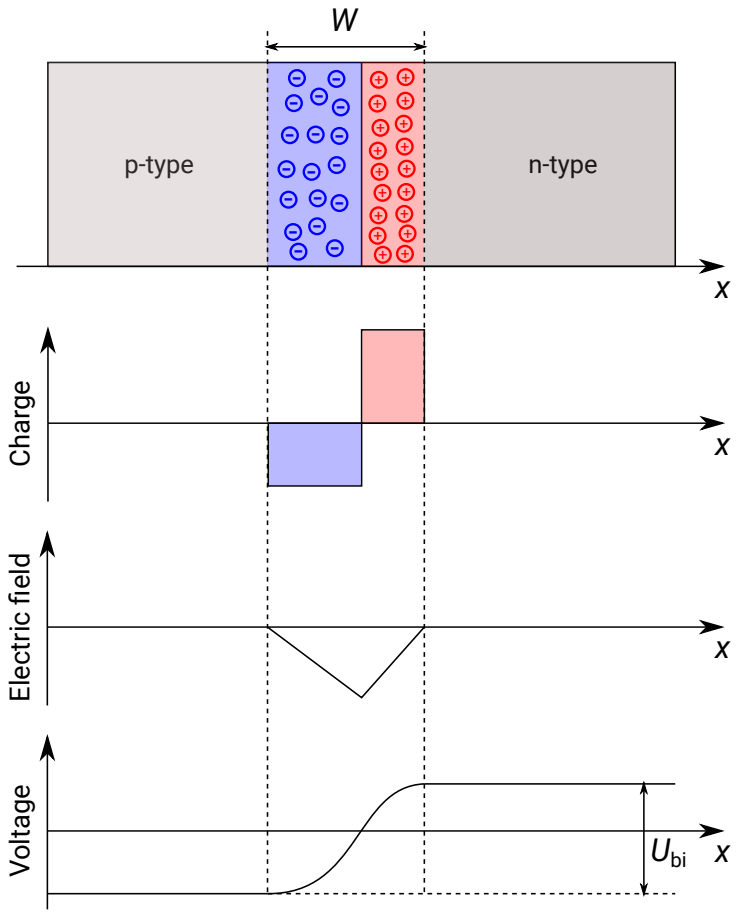

Figure 3.1: Illustration of the space charge regions around a p-n junction and the resulting electric field and potential

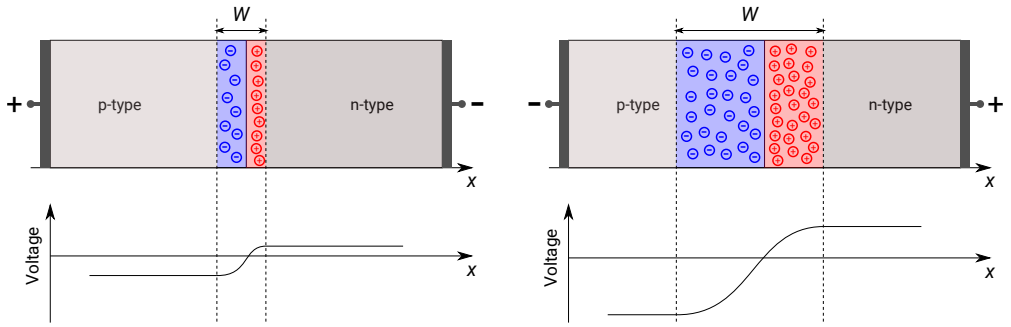

(a) Forward bias (b) Reverse bias

Figure 3.2: Illustration of the change in the width of the depletion region and the potential difference across a p-n junction in forward (a) and reverse (b) bias

tion. When the bias voltage and therefore the potential difference becomes large enough, the depletion region breaks down and a large current starts to flow. Two breakdown mechanisms can occur (independently or simultaneously). Tunneling of electrons from the valence to the conduction band is called the Zener effect. An avalanche breakdown on the other hand occurs when electrons are sufficiently accelerated by the electric field to create new electron-hole pairs upon collision with bound electrons.
The current-voltage characteristic of a p-n junction is shown in figure 5.8. In forward bias, it is given by the Shockley diode equation:

$$I = I_{\mathrm{S}}\left(e^{\frac{qV}{nk_{\mathrm{B}}T}} - 1\right) \tag{3.1}$$

with the reverse bias saturation current I_{S}, the elementary charge q, the Boltzmann constant k_{B}, the temperature T, and a quality factor n, which accounts for non-ideal behaviour of real diodes.
I_{S} is part of the reverse leakage current. It is almost independent of the reverse bias voltage and it is caused by the diffusion of minority carriers from the neutral regions into the depletion region. A more important component of the leakage current, which is a noise source for silicon detectors, is the thermal generation of free charge carriers in the depletion region. It is proportional to the volume of the latter and therefore denoted as I_{vol}. Its temperature dependence is given by

$$I_{\mathrm{vol}} \propto T^2 \mathrm{e}^{-E_{\mathrm{g}}(T)/(2k_{\mathrm{B}}T)} \tag{3.2}$$

with the size of the band gap E_{g}. As a rule of thumb the volume current doubles every 8 K [41].

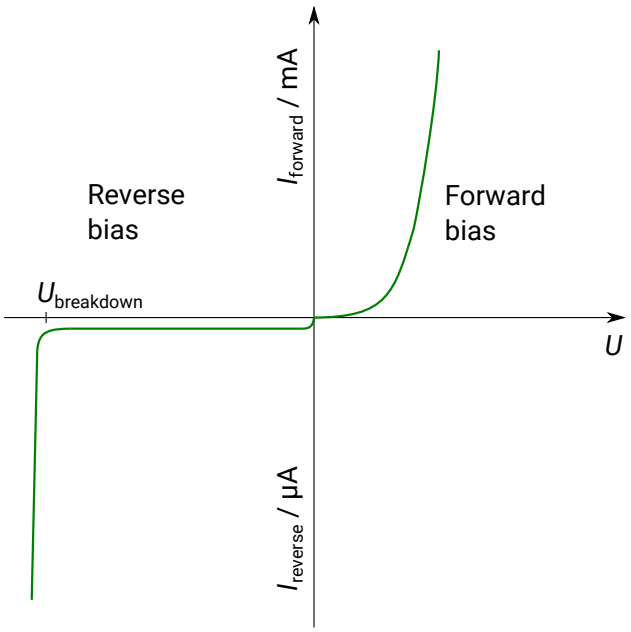

Figure 3.3: Current-voltage characteristic of a p-n junction

The width W of the depletion region is given by

$$W = \sqrt{\frac{2\epsilon_{\text{Si}}}{e}\left(\frac{1}{N_{\text{A}}} + \frac{1}{N_{\text{D}}}\right)(U + U_{\text{bi}})}\,, \tag{3.3}$$

where ϵ_{Si} is the absolute permittivity of silicon, e is the electric charge, N_{A} and N_{D} are the acceptor and donor concentrations, and U is the reverse bias voltage. The built-in voltage U_{bi} is of the order of 0.5 V and for silicon detectors usually negligibly small compared to U. The resistivity ρ of doped silicon is related to the dopant concentration N by

$$\rho = \frac{1}{eN\mu}, \tag{3.4}$$

where μ is the mobility of free charge carriers. Silicon detectors usually consist of shallow highly doped implants inside a low-doped substrate such that the depletion region mostly forms inside the substrate. Let N be the doping concentration of the substrate. Then equations 3.3 and 3.4 (and $U \gg U_{\text{bi}}$) yield

$$W \approx \sqrt{2\epsilon_{\text{Si}}\mu\rho U}. \tag{3.5}$$

The maximum of the electric field is located directly at the junction and its value is

$$E_{\max} = \frac{2U}{W} \approx \sqrt{\frac{2eN}{\epsilon_{\mathrm{Si}}}U}. \tag{3.6}$$

The total capacitance C that is charged by the signal charge Q has many components, some of which are hard to quantify [41]. A major contribution is given by the detector capacitance C_{d} of the pixel diode, which can be approximated by that of a parallel plate capacitor:

$$C_{\mathrm{d}} = \epsilon_{\mathrm{Si}}\frac{A}{W}, \tag{3.7}$$

where A is the area of the charge collection electrode. A smaller C leads to larger signals. While the dominant noise sources might also depend on C_{d} they are usually internal to the amplifier circuit and dont't stem from actual physical charge at the amplifier input in contrast to the signal. A smaller C_{d} leads to a better signal-to-noise ratio (SNR) [42].

3.2 Readout electronics

The front-end readout electronics of silicon pixel detectors consist of integrated circuits, which are fabricated using the same microprocessing techniques as for the sensor diodes. They can be implemented on the same substrate as the sensor or on a separate chip. Their fundamental building blocks are metal-oxide-semiconductor field-effect transistors (MOSFET). This subsection focuses on summarizing the working principle and basic characteristics of MOSFETs.
A MOSFET has four terminals: gate, source, drain, and substrate (see figure 3.4). Its operating principle is based on the modulation of the charge concentration between source and drain by the gate electrode, which is insulated from the other device regions by a dielectric layer, which consists of silion dioxide[1]. Source and drain are connected to separated highly doped regions of the opposite type than the substrate. If they are of p-type, the MOSFET is called pMOSFET and, analogously, if they are of n-type, the MOSFET is called nMOSFET (see figure 3.5). Logic that is implemented using only one type of MOSFET is accordingly called PMOS or NMOS logic. If both types are used, the logic is called Complementary MOS (CMOS) logic.
There are three types of operation of a MOSFET depending on the voltages at the terminals. They are discussed in the following in case of an nMOSFET (same as for pMOSFET with opposite polarities of charges and voltages):

[1]Less commonly also other insulater materials are used. The device is then called metal-insulator-semiconductor field-effect transistor (MISFET).

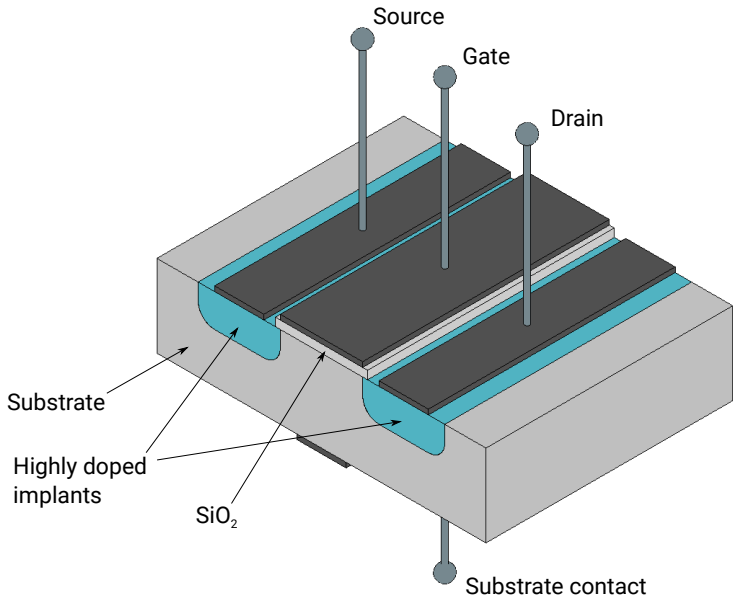

Figure 3.4: Generic drawing of a MOSFET

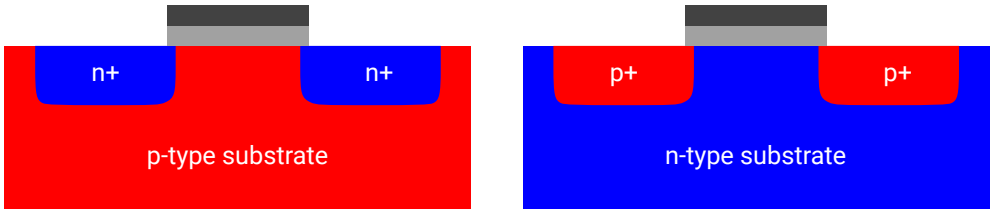

(a) nMOSFET (b) pMOSFET

Figure 3.5: Schematic drawings of an nMOSFET and a pMOSFET

Cutoff: When the gate-source voltage is smaller than the device's intrinsic threshold voltage ($U_{\mathrm{GS}} < U_{\mathrm{th}}$), the device is turned off. Ideally, the current between drain and source is zero (see figure 3.6a). In reality, a small sub-threshold leakage current can flow.

Linear region: When $U_{\mathrm{GS}} > U_{\mathrm{th}}$ and $U_{\mathrm{DS}} < U_{\mathrm{GS}} - U_{\mathrm{th}}$, where U_{DS} is the drain-source voltage, the transistor is turned on. A so-called inversion layer of electrons populates the region underneath the electrode forming a conductive channel between source and drain (see figure 3.6b). The electron density in the channel is controlled by the gate voltage. The transistor acts like an adjustable resistor.

Saturation region: When $U_{\mathrm{GS}} > U_{\mathrm{th}}$ and $U_{\mathrm{DS}} > U_{\mathrm{GS}} - U_{\mathrm{th}}$, the channel does not extend to drain anymore, but the electric field between drain and the channel is very high, so conduction continues. In this mode, the source-drain current is only weakly dependent on the gate voltage.

The typical resulting voltage-current characteristic of a MOSFET is shown in figure 3.7.

Body effect: The body effect is a change of the threshold voltage due to the application of a voltage $U_{\mathrm{BS}} \neq 0$ between source and the substrate, also called bulk or body. The substrate can then be considered as a second gate.

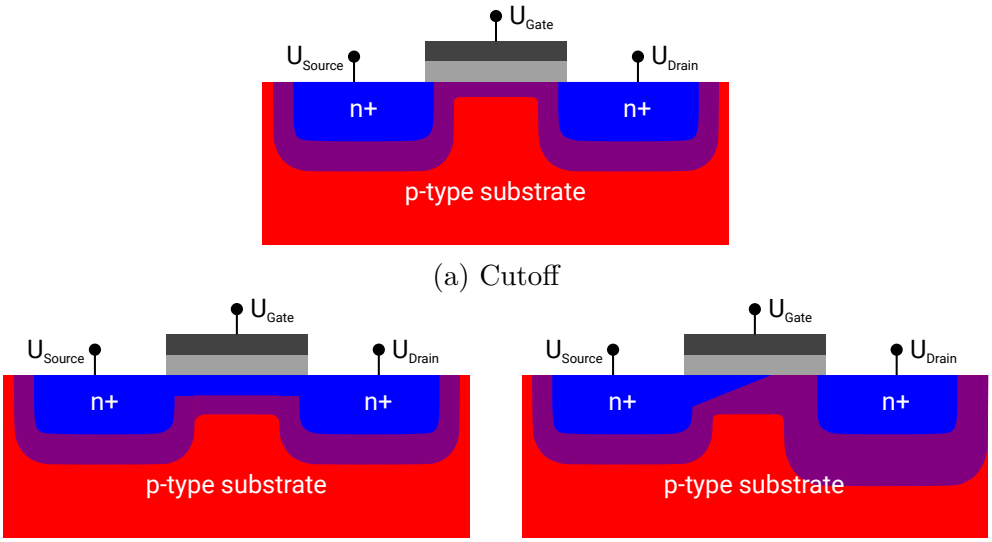

(a) Cutoff

(b) Linear region

(c) Saturation region

Figure 3.6: Operating modes of an nMOSFET; purple regions are depleted

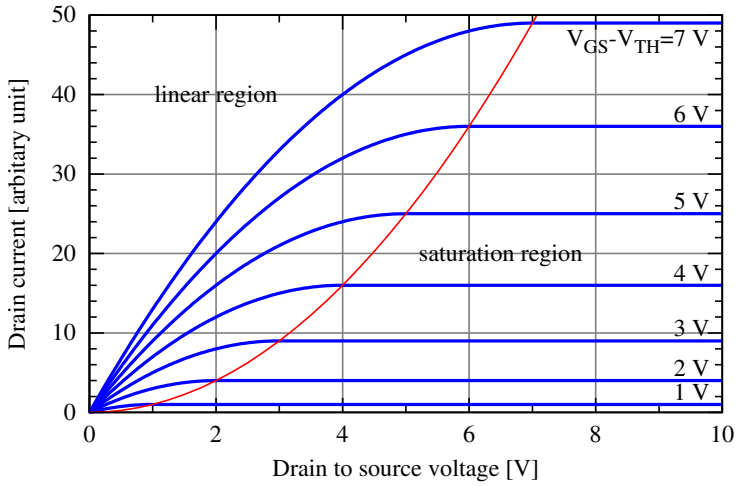

Figure 3.7: Current-voltage characteristics of a MOSFET [43]

3.3 Radiation damage to silicon detectors

In particle physics experiments, detectors often have to be operated in high radiation environments, which continuously causes damage to them and limits their lifetime. Especially pixel detectors are often brought as close to the interaction point as possbile because of their high granularity. Therefore, they have to fulfill high requirements in terms of radiation tolerance.
One distinguishes roughly between two fundamental mechanisms of radiation damage, namely surface effects resulting from ionization and radiation-induced defect formation in the silicon bulk.

3.3.1 Ionization effects

Ionizing radiation can have cumulative effects on silicon detectors. They are referred to as total ionizing dose (TID) or surface effects. The second term stems from the fact that the effects occur inside the silicon oxide (SiO_2), used as the dielectric between the gate electrode and the silicon in transistors, and at the interface between the silicon and the oxide. The TID affects a detector's readout circuitry.
In addition, ionizing radiation can cause single-event effects (SEE), e.g. the change of the logical state of a memory cell, which can lead to corrupted data or device failure.

Total ionizing dose effects

The total ionizing dose is the energy deposited in the detector volume by radiation via ionization. It is typically measured in gray (Gy). 1 Gy equals 1 J/kg.
Ionizing radiation creates electron-hole pairs in a transistor's oxide layer, most of which recombine immediately depending on the electric field. Electrons, however, have a high mobility in the oxide and some of them can be collected by a close-by positive electrode (e.g. the gate). Holes have a very low mobility in the oxide, due to many shallow hole traps [41]. Steered by the electric field, they move slowly by hopping from one shallow trap to the next. They can be trapped permanently by deep hole traps, possibly oxygen interstitials, which have a high density close to the interface between silicon and oxide [41]. A positive space charge region is created in the oxide.
Another ionizing dose effect is due to trivalent silicon atoms with one dangling bond, again at the interface between silicon and oxide. Dangling bonds are usually saturated with OH^--ions during production, but the ions can be separated from the silicon by radiation and then drift towards the positive

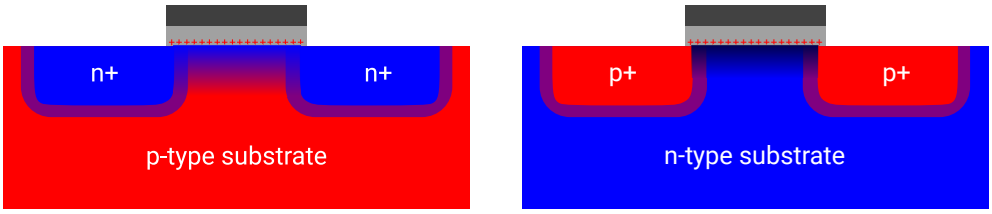

(a) nMOSFET can form conductive channel when "turned off"

(b) pMOSFET requires higher gate voltage to be "switched on"

Figure 3.8: Illustration of the mechanisms inducing threshold shifts of nMOS (a) and pMOS (b) transistors due to TID effects

electrode, leaving so-called interface states (or traps) that can trap either electrons or holes from the silicon bulk, depending on the doping [44].
The trivalent silicon atoms with a dangling bond can also contribute to the positive oxide charge, when the outer electron that not involved in a bond is removed by scattering with other electrons [41].
Oxide-trapped charge anneales at room temperature due to the tunneling of electrons from the silicon into the oxide while interface-trapped charges can partially anneal at higher temperatures ($\gtrsim 100\,°C$) [45].
The dominant radiation effects in MOS devices are due to positive oxide charge. It can change the threshold volage of a transistor. As illustrated in figure 3.8, the positive oxide charge creates a permanent conductive channel underneath the gate of an nMOS transistor while for a pMOS transistor it becomes harder to form the conductive channel. Consequently, the design current specifications of a circiut might not be able to be met or the transistors might not switch at all anymore.
Additionally, leakage currents can occur at the edges of the gate oxide (bird's beak) or the shallow trench isolation (STI) between transistors, which is also realized by SiO_2, where high electric fields can lead to high charge accumulation.
In general, surface effects are highly dependent on the used technology and the exact production process of the detector as well as the bias conditions during irradiation. The downscaling of transistor technologies lead to very thin oxide layers, such that surface effects have become less of a problem. Furthermore, gate-enclosed (or circular) transistors have been developed to reduce radiation induced leakage currents. Here, the drain contact is fully surrounded by the gate electrode, such that there is no oxide edge that connects source and drain.

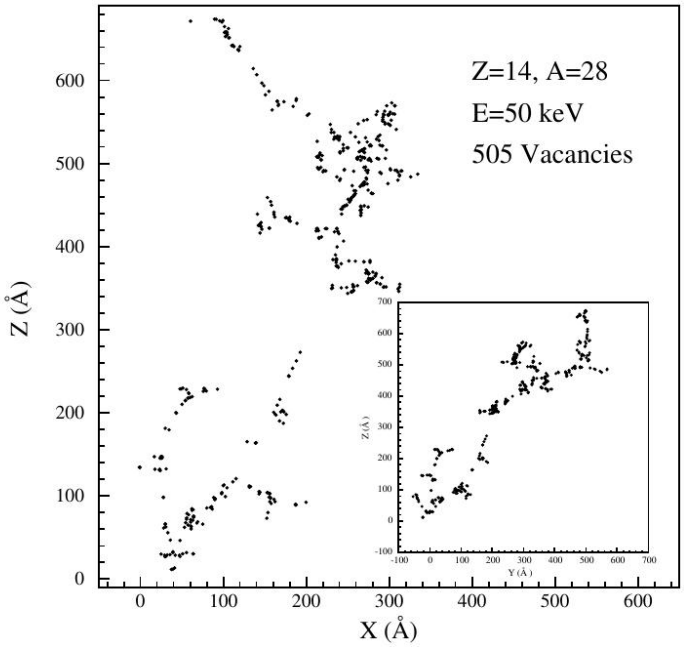

Figure 3.9: Simulation result for the spatial distribution of vacancies created by a single 50 keV Si atom [46]

3.3.2 Silicon bulk damage

High-energetic particles interact with the nuclei in the silicon bulk, which can lead to a displacement with respect to their lattice position. Such defects alter the electric properties of the material. Note that these effects are not relevant for SiO_2, because its structure is already highly irregular.
Hadrons (neutrons, protons, pions, etc.) or higher energetic leptons are able to displace Si ions to an interstitial site, leaving a vacancy at its place. If the recoil Si ion has enough energy, it can cause further defects or a defect cluster. Figure 3.9 [46] shows simulation results for the spatial distribution of the defects created by a single Si ion with a kinetic energy of 50 keV. In total, there are 505 vacancies. Part of the energy of a initial impinging charged particle is lost via ionization but this energy transfer is reversible and does not have a significant impact on the lattice structure.
The primary defects, interstitials and vacancies, are able to migrate through the silicon lattice. Hence, part of them anneals, but the remaining ones interact with each other or impurity atoms, forming different types of secondary point defects. Those secondary defects together with the defect clusters are the source of the macroscopic deterioration of detector properties.
Defects introduce localized states with energy levels inside the silicon band

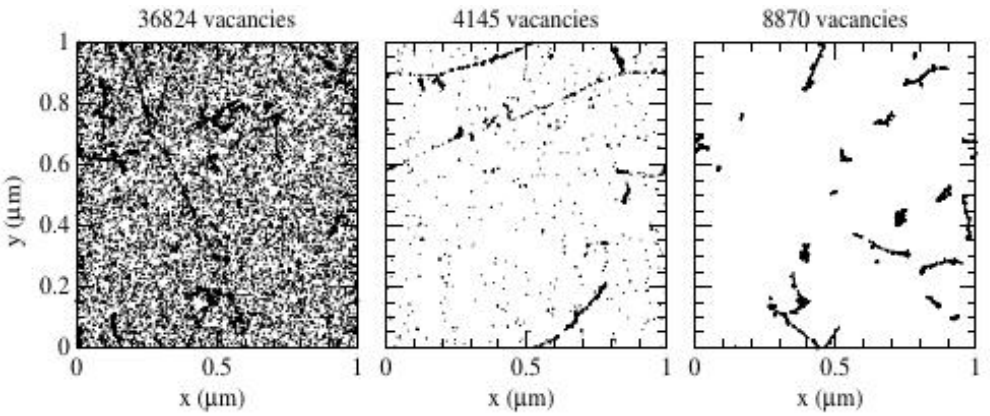

Figure 3.10: Simulation results for the initial spatial distribution of vacancies created by 10 MeV protons (left), 24 GeV protons (middle), and 1 MeV neutrons (right) [46]

gap and can act as generation and recombination centers for electron-hole pairs, trap charge carriers, and change the effective doping concentration.
Different kinds of particles interact differently with the silicon lattice. While, for example, neutrons only take part in nuclear interactions, silicon nuclei get partially screened from protons by their eletron clouds [41]. Figure 3.10 [46] illustrates the difference in the initial spatial distribution of vacancies created by 10 MeV protons, 24 GeV protons, and 1 MeV neutrons. The results stem from simulations of fluences of 10^{14} particles/cm^2. The plots show projections over 1 µm in the dimension perpendicular to x and y.
Despite obvious differences it is common practice to assume the non-ionizing energy loss (NIEL) scaling hypothsis, which says that, within some error margin, the NIEL damage caused by different types of particles differs only by an energy-dependent scaling factor, the so-called hardness factor κ. To compare results for irradiation with different particle species, one usually scales the fluence to that of 1 MeV neutrons that would result in the same damage. The fluence is then given in the unit 1 MeV n_{eq}/cm^2, while sometimes 1 MeV is omitted for convenience. n_{eq} stands for neutron equivalent.

Effects of bulk damage on sensor properties

Leakage current: The increased probability of charge carrier generation at the defects contributes to the leakage current in the silicon bulk. The contribution is proportional to the fluence ϕ:

$$I_{\text{vol}} = I_{\text{vol},0} + \alpha\phi V \tag{3.8}$$

α is called the current-related damage rate and V denotes the bulk volume. The increase in leakage current leads to more electronic noise and a larger power dissipation. The latter heats up the sensor which leads to an even larger leakage current. This can result in a feedback loop called thermal runaway.

Effective doping concentration: Radiation-induced defects can change the effective doping concentration N_{eff}, which is the difference of all donor-like states and all acceptor-like states. It is related to the full depletion voltage U_{dep}, the smallest reverse bias voltage for which the width of the depletion region W equals the thickness of the sensor d, by

$$N_{\text{eff}} = \frac{2\epsilon_{\text{Si}}}{ed^2} U_{\text{dep}}. \tag{3.9}$$

A phenomenological parameterization is given by [47]:

$$N_{\text{eff}} = N_{\text{eff},0} - N_{\text{C}}(\phi) + N_{\text{a}}(\phi, T_{\text{a}}, t) + N_{\text{Y}}(\phi, T_{\text{a}}, t) \tag{3.10}$$

The first term characterizes the deactivation of removable donors, assuming an initial n-type substrate, and the creation of acceptor-like defects:

$$N_{\text{C}}(\phi) = N_{\text{C},0}\,(1 - e^{-c\phi}) + g_{\text{c}}\phi \tag{3.11}$$

Donors are removed exponentially with ϕ. c is the material-dependent removal constant. The creation of acceptor-like defects is proportional to ϕ. The according defects are called acceptor-like because they lead to a negative space charge. In figure 3.11 [48], $|N_{\text{eff}}|$ and U_{dep} directly after irradiation are plotted against the fluence after correction for annealing during the irradiation process. At some point the space charge in an initial n-type substrate vanishes almost completely and after that the depletion behaviour is the same as for a p-type substrate. This is called type inversion. Note that the creation of acceptor-like states can be slowed down by the enhancement of the oxygen concentration in the silicon [49].
The second term in equation 3.10, denoted with N_{a}, parameterizes a short-term or beneficial annealing process and the third term, denoted with N_{Y}, the long-term so-called reverse annealing. The annealing depends on the annealing time t and temperature T_{a}. Figure 3.12 [47] shows N_{eff} plotted against the annealing time.

Acceptor removal: Initial dopant removal also occurs in p-type material for acceptors. It is considered non-relevant for high-resistivity substrates that are used in established pixel sensor technologies and already have a low

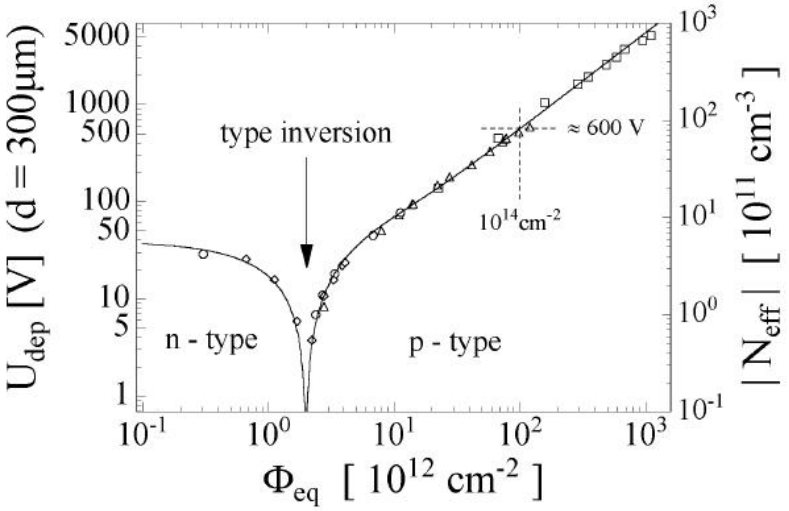

Figure 3.11: $|N_{\text{eff}}|$ and U_{dep} vs fluence [48]

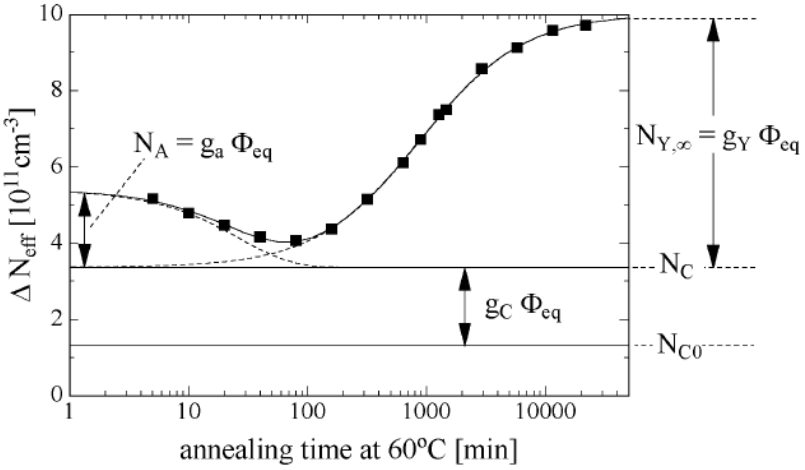

Figure 3.12: $|N_{\text{eff}}|$ vs annealing time [47]

N_{eff} from the start. However, initial acceptor removal can be relevant for new detector technologies like HV-MAPS that have a relatievely high initial doping concentration. First studies have shown that the fraction of removed acceptors increases with the fluence for neutron irradiation while the removal is observed to be complete [50] for proton irradiation. It has also been shown that the removal constant c decreases with increasing fluence. Further studies are required to gain a better understanding of acceptor removal [50, 51, 52].

Charge trapping: Some defects act as trapping centers. An electron trap captures an electron and releases it again into the valence band. The trapping of signal charges for longer than the charge collection time can lead to a significant charge collection deficiency. The release of trapped charges after the charge collection time contributes to the leakage current.

3.4 Particle tracking with silicon detectors

This section briefly discusses how silicon detectors are used in particle physics experiments to reconstruct particle tracks, momenta, and interaction vertices. Silicon detectors measure space points along particle trajectories in planes or cylindrical layers at fixed distances with respect to the nominal interaction point. A typical geometry of a tracking or vertex detector in collider experiments consists of several cylindrical layers of silicon detectors, whose symmetry axes are coincident with the beam axis. A projection of such a geometry onto the plane transverse to the beam is shown in figure 3.13. The reconstruction of paricle momenta requires a magnetic field that forces charged particles on a helical trajectory. Typically, a solenoid magnet is used to create a homogenous field parallel to the beam axis.

Measurement of the transverse momentum

The momentum component p_{T} transverse to the beam axis is given by

$$p_{\text{T}} = |q|Br = \frac{qB}{\kappa}\,, \tag{3.12}$$

where q is the charge, B is the magnetic field parallel to the beam axis, r is the radius of the projection of the trajectory onto the transverse plain, which describes a circle, and κ is the curvature defined as

$$\kappa = \frac{q}{|q|} \cdot \frac{1}{r}\,. \tag{3.13}$$

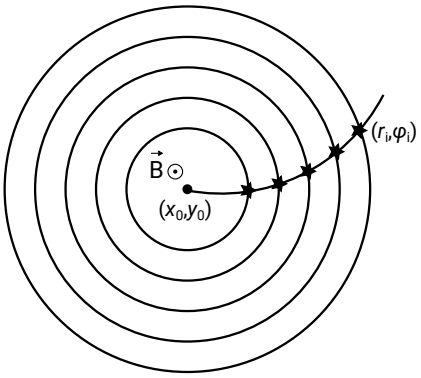

Figure 3.13: Schematic drawing of the projection of a barrel-shaped tracking detector onto the transverse plane

Consider the geometry shown in figure 3.14 of a particle trajectory in the transverse plain crossing three detector layers with equal distances of $L/2$. For small angles α, i.e. for large momenta, κ is related to the sagitta s by

$$|\kappa| \approx \frac{8}{L^2}\, s\,. \tag{3.14}$$

Therefore, the error of κ is

$$\sigma_\kappa = \frac{8}{L^2}\, \sigma_\mathrm{s}\,, \tag{3.15}$$

with σ_s being the error of s. The finite spatial resolution of the detectors can be quantified as a measurement error σ_det in y-direction, which is assumed to be the same for all three layers. It is

$$\sigma_\mathrm{s} = \sqrt{\frac{3}{2}}\, \sigma_\mathrm{det}\,. \tag{3.16}$$

The factor $\sqrt{3}$ stems from the number of detector layers $N = 3$. It can be shown that in the general case of N detector layers the error of the curvature is [53]

$$\sigma_\kappa = \frac{\sigma_\mathrm{det}}{L^2} \sqrt{\frac{720(N-1)^3}{(N-2)N(N+1)(N+2)}}\,. \tag{3.17}$$

The error of p_T is given by

$$\sigma_{p_\mathrm{T}} = \frac{p_\mathrm{T}^2}{|q|B}\, \sigma_\kappa. \tag{3.18}$$

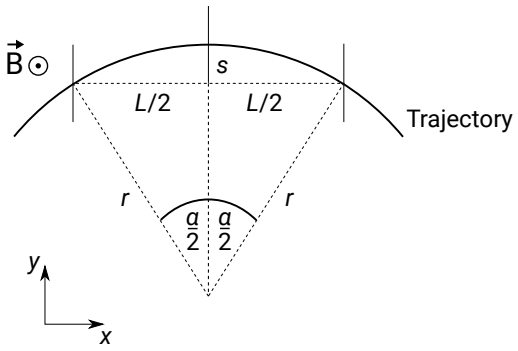

Figure 3.14: Projection onto the transverse plain of a particle trajectory crossing three equidistant detector layers in a magnetic field parallel to the beam axis

This result has several consequences for the optimum design of a pixel tracker. The relative transverse momentum resulution $(\frac{\sigma_{p_\mathrm{T}}}{p_\mathrm{T}})_\mathrm{det}$ is proportional to σ_det. Hence, the pixel pitch in the transverse plane has to be small. However, at some point mechanical tolerances and multiple Coulomb scattering (see below) will dominate over the contribution from the pixel size.
The proportionality of $(\frac{\sigma_{p_\mathrm{T}}}{p_\mathrm{T}})_\mathrm{det}$ to $1/L^2$ implies that a large lever arm is beneficial.
The same is true for the magnetic field due to $(\frac{\sigma_{p_\mathrm{T}}}{p_\mathrm{T}})_\mathrm{det} \propto 1/B$.
The relative transverse momentum resolution improves with the number of detector layers since it is approximately proportional to $1/\sqrt{N}$. However, the improvement becomes smaller with every additional layer.
Finally, it has to be pointed out that - and this cannot be improved on by optimizing the detector design - the relative transverse momentum resolution is proportional to p_T, i.e. it gets worse with larger momenta.

Multiple Coulomb scattering

Charged particles traversing a medium get deflected due to multiple Coulomb interactions with nuclei. This results in a displacement Δy and a deflection angle θ with respect to the undisturbed trajectory (see figure 3.15 [54]).
For thin scatterers, Δy can usually be neglected. The angular distribution of scattering angels can be described by Molière's theory. It can be projected onto two orthogonal planes. The results have a normally distributed core and additional tails due to large angle single scattering events. The RMS of the central 98 % of the planar scattering angle distribution θ_0 is given by [54]

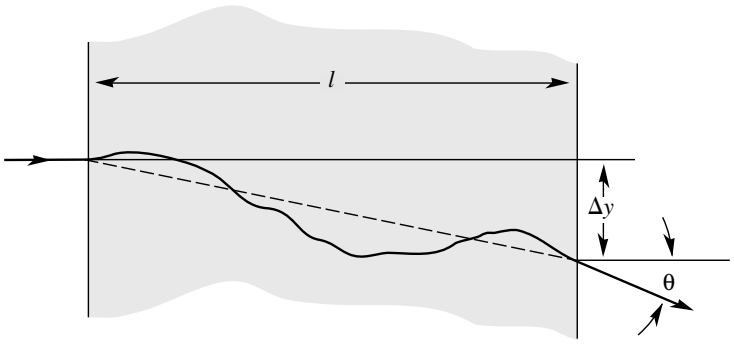

Figure 3.15: Illustration of multiple Coulomb scattering; modified from [54]

$$\theta_0 = \frac{13.6\,\mathrm{MeV}}{\beta c p}\, z \sqrt{\frac{l}{X_0}}\Big(1 + 0.038 \ln(\frac{l z^2}{X_0 \beta^2})\Big)\,, \tag{3.19}$$

where βc is the velocity of the incident particle, z its charge number, l the thickness of the medium, and X_0 the radiation length, a material constant that is used as a measure of energy loss of a traversing particle. The effect of multiple Coulomb scattering increases approximately proportionally to $\sqrt{l}$, while it decreases with $1/p$.
Multiple Coulomb scattering adds another contribution $(\frac{p_\mathrm{T}}{\sigma_{pT}})_\mathrm{scat}$ to the relative transverse momentum resolution. The latter is given in total by

$$\frac{\sigma_{p_\mathrm{T}}}{p_\mathrm{T}} = \sqrt{\Big(\frac{\sigma_{p_\mathrm{T}}}{p_\mathrm{T}}\Big)^2_\mathrm{det} + \Big(\frac{\sigma_{p_\mathrm{T}}}{p_\mathrm{T}}\Big)^2_\mathrm{scat}}\,. \tag{3.20}$$

Identification of secondary vertices

Events in collider experiments that involve b-quarks are usually of special interest. b-quarks form mesons that have a relatively long lifetime ($\mathcal{O}(1\,\mathrm{ps})$) and can therefore travel a significant distance ($\mathcal{O}(1\,\mathrm{mm})$) before they decay. This leads to vertices displaced from the nominal collison point. The identification of such secondary vertices allows to tag the corresponding events.
The performance in regard to identifying secondary vertices is quantified by the impact parameter resolution. The impact parameter d_0 is the smallest distance in the transverse plane of a reconstructed trajectory to the nominal collision point.
Consider again the geometry shown in figure 3.14, where the coordinate system is oriented such that the ideal trajectory crosses the detector layers at equal distances in x-direction. $x = 0$ shall be placed at the mean of the

x-values. It can then be shown that the d_0-resolution can be calculated as [53]

$$\sigma_{d_0,\mathrm{det}} = \sigma_{\mathrm{y,det}} = \frac{\sigma_{\mathrm{det}}}{\sqrt{N}}\Big[1 + \frac{12(N-1)}{(N+1)}\Big(\frac{x_0}{L}\Big)^2 + \frac{180(N-1)^3}{(N-2)(N+1)(N+2)}\Big(\frac{x_0}{L}\Big)^4 + \frac{30N^2}{(N-2)(N+2)}\Big(\frac{x_0}{L}\Big)^2\Big]^{\frac{1}{2}}, \tag{3.21}$$

where x_0 is the x-component of the nominal collision point. Consequently, it is beneficial to move the detector as close to the beamline as possible. The last two terms in the square root are due to the uncertainty of the curvature measurement, which can be improved on with a separate measurement by a detector larger than the vertex detector [53].
The effect of multiple Coulomb scattering on σ_{d_0} is dominated by the beampipe and the innermost detector layer and, assuming the innermost layer is placed directly on the beampipe, it is [53]

$$\sigma_{d_0,\mathrm{scat}} = \theta_{0,\mathrm{inner}}\, r_{\mathrm{inner}}\,, \tag{3.22}$$

with the beampipe radius r_{inner} and the RMS of the planar scattering angle distribution $\theta_{0,\mathrm{inner}}$ resulting from multiple Coulomb scattering in the inner layer and the beampipe. Also this result shows that a vertex detector should be located close to the nominal collision point.

3.5 Silicon pixel detector technologies used in particle physics

Before spreading into many fields of application, the development of position-sensitive semiconductor detectors was initiated in particle physics in the 1970s. Better spatial resolution and higher rate capabilities were required than bubble or drift chambers could provide, which first lead to the development of silicon microstrip detectors. They differ from pixel detectros by their sensing elements being elongated in one dimension ($\mathcal{O}(1\,\mathrm{cm})$). The development was made possible by making use of fabrication processes already established in microelectronics.

3.5.1 Hybrid pixel detectors

Hybrid pixel detectors were initially developed for and have become well established in particle physics. A prominent example is the ATLAS pixel detector, which is discussed in section 2.2.1. Hybrid detectors also represent the baseline technology for the ATLAS ITk upgrade (see section 2.2.2).
The distinguising feature of hybrid detector technologies is that the detection elements, implemented as an array of silicon diodes, and a readout ASIC (application-specific integrated circuit) are fabricated as separate entities. This allows for them to be optimized separately. While readout ASICs typically use standard substrate resistivities ($\sim 20\,\Omega\mathrm{cm}$), the sensors use high substrate resistivities of $\mathcal{O}(1\,\mathrm{k}\Omega\mathrm{cm})$. Sensor and readout ASIC have to be electrically coupled by bump-bonding. In this process (also called flip chip) every pixel is connected via its own solder bump to the readout ASIC. The concept is illustrated in figure 3.16.
Two types of hybrid pixel detectors can be distinguished by the shape and orientation of the depletion region: planar and 3D. While planar sensors are a well established technology, 3D sensors were operated first in a detector in the case of the ATLAS IBL (see section 2.2.1). The two technologies are discussed in the following.

Planar sensors

The pixel diodes are implanted at one side of the silicon bulk as illustrated in figure 3.17. The width of the depletion region corresponds to the full sensor width of typically $\sim 300\,\mu\mathrm{m}$ for detectors in operation and $\sim 100\,\mu\mathrm{m}$ for newly developed detectors [36]. The long charge collection distance makes this type of sensor prone to charge collecion inefficiencies after irradiation

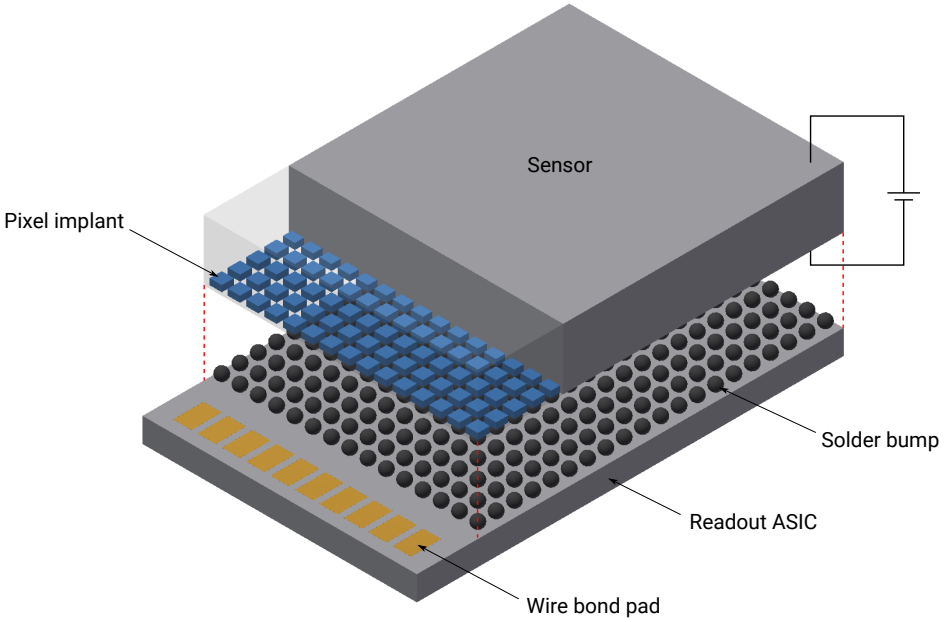

Figure 3.16: Illustration of the hybrid pixel detector concept

due to charge trapping (see section 3.3.2). To an extent, this can be compensated by increasing the reverse bias voltage up to ca. 1000 V. But this leads to a high power dissipation that needs to be cooled away. Planar sensors are proven to be able to achieve detection efficiencies of above 97 % up to radiation fluences of $1 \cdot 10^{16}\,\mathrm{n_{eq}/cm^2}$ [55].

3D sensors

3D sensors consist of an active p-type silicon bulk into which an array of n- and p-type electrodes are etched perpendicularly to the sensor surface (see figure 3.18). This results in a smaller charge collection distance compared to planar sensors as illustrated in figure 3.19 [57]. Hence, the trapping probability is lower and the sensor can be operated at lower bias voltages after high radiation fluences. It was shown that after a fluence of $2.8 \cdot 10^{16}\,\mathrm{n_{eq}/cm^2}$ an efficiency of above 97 % can be reached with a bias voltage below 150 V [56]. However, the production of 3D devices requires a complicated process affecting the yield, the production time and costs [58]. 3D sensors are chosen as the baseline technology for the two innermost layers of the ITk [36].

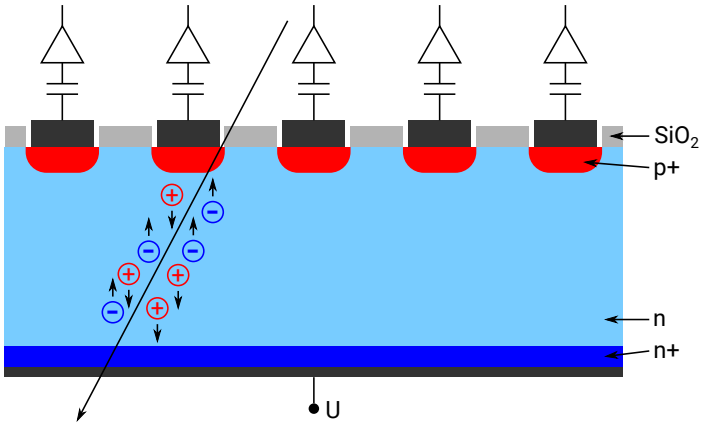

Figure 3.17: Schematic drawing of a planar pixel sensor

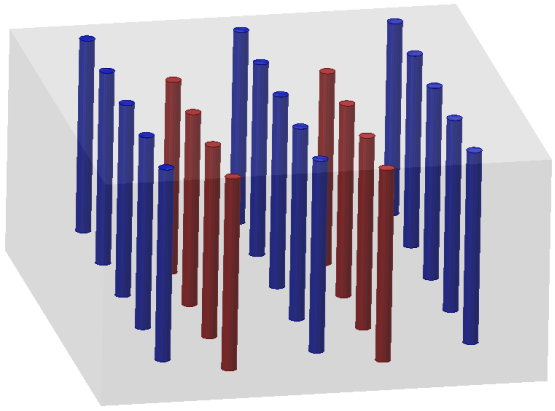

Figure 3.18: Schematic drawing of a 3D sensor showing the arrangement of n-type (blue) and p-type (red) electrodes

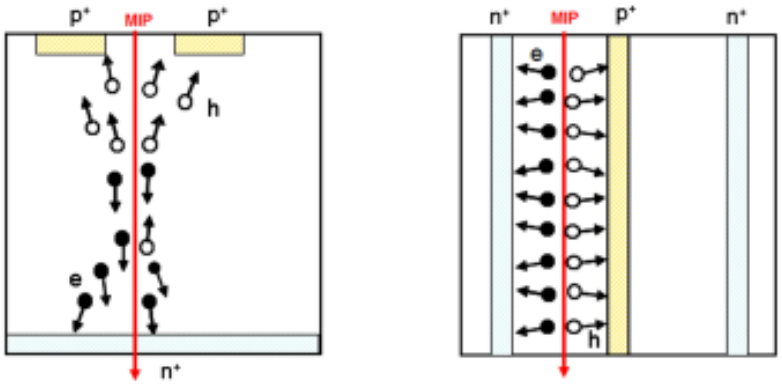

Figure 3.19: Schematic drawing illustrating the drift path in planar (left) and 3D (right) sensors; modified from [57]

3.5.2 Monolithic pixel detectors

A different approach to pixel detectors is to implement the sensor diode array and the front-end readout electronics in the same chip. This has some obvious advantages compared to hybrid detectors. First, it does not require the very cost and time intensive bump-bonding process needed for the production of hybrid detectors. Furthermore, it saves material, which reduces multiple Coulomb scattering and can therefore improve the tracking performance (see section 3.4). Especially the first point is becoming more relevant as tracking environments are becoming more dense and experiments are relying more on the high granularity of pixel detectors, which are therefore growing in size.
Within monolithic pixel sensors one generally distinguishes between charge-coupled devices (CCDs) and active-pixel sensors.
CCDs shift collected signal charges successivley from pixel to pixel until they reach an area on the chip where the charges can be processed. This requires a minimum of in-pixel electronics and allows for very small pixel sizes down to about $2 \times 2\,\mu m^2$ [59] and very thin chips ($\sim 20\,\mu m$). However, this technology has some drawbacks, e.g. the charge transport over long distances makes CCDs vulnarable for charge trapping due to radiation damage [60] and limits their readout speed.
In particle physics, the focus lies more on the development of active-pixel sensors, often also referred to as CMOS sensors. Here, signal processing electronics is implemented inside every pixel. In the following, different examples of monolithic active-pixel sensors developed within the particle physics community are presented.

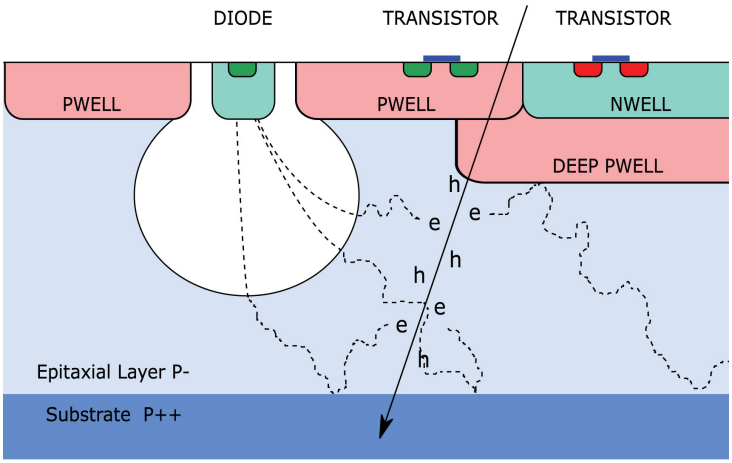

Figure 3.20: Illustration of the MAPS concept as implemented in the ALPIDE sensor [62]

First MAPS used in a vertex detector

The first large scale application of monolithic active pixel sensors (MAPS) in a collider environment is the PXL detector [61] of the STAR experiment at RHIC. It uses the so-called Ultimate-2, also known as Mimosa28, sensor. This sensor has a reticle size of $20.22 \times 22.71\,\mathrm{mm}^2$ and 928×960 square pixels with a pitch of $20.7\,\mu\mathrm{m}$. It is fabricated in a $0.35\,\mu\mathrm{m}$ process und uses a high-resistivity ($\geq 400\,\Omega\mathrm{cm}$) p-type epitaxial layer with a thickness of $15\,\mu\mathrm{m}$, in which signal charges are created. The epitaxial layer is grown on a highly doped p-type substrate and has highly doped p-well implants hosting the in-pixel electronics (see figure 3.20 [62], the deep p-well is not used here but in the ALPIDE sensor discussed below). The charge collection diode is implemented as n-well implant and biased with approximately 0.8 V [61]. The epitaxial layer is not fully depleted and signal charges move mainly by diffusion. Every pixel hosts an amplifier. Hits are digitized on chip. A rolling-shutter readout is used, where all colums are read out in parallel, one row at a time. One readout cycle takes $185.6\,\mu\mathrm{s}$. The chip periphery includes zero-suppression circuitry and the data is send off chip via two Low-Voltage Differential Signaling (LVDS) links at a clock speed of 160 MHz. The power dissipation of the full chip is ca. 700 mW [61].

ALPIDE

The ALPIDE sensor [63] was developed for the new inner tracking system (ITS) of the ALICE experiment at the LHC. The detector is designed to cover an area of about $10\,\mathrm{m}^2$ with seven barrel layers. At the time of writing

it is being assembled.
The sensor is based on the same concept as the Ultimate-2 sensor, but it uses a 180 nm CMOS process, which has several benefits. The smaller feature size should increase the tolerance towards ionizing radiation (see section 3.3.1). It also allows for a higher integration density enabling improvements on the readout speed[62]. In addition, the technology offers the possibiliy to use deep p-well implants (see figure 3.20 [62]), which allow for implementing full CMOS logic in the active sensor area without interfering with the charge collection. Furthermore, the process grants thicker epitaxial layers with higher resistivity, which increases the depletion region (see section 3.1). The sensor is specified to have a power consumption below $40\,\mathrm{mW/cm^2}$ [63].

Modifications to the ALPIDE concept

While the ALPIDE sensor is sufficiently tolerant towards NIEL damage well beyond a fluence of $10^{13}\,\mathrm{n_{eq}/cm^2}$ [64], going to $10^{15}\,\mathrm{n_{eq}/cm^2}$ requires charge collection via drift, i.e. a larger depletion region, to reduce the path length of signal charges as well as the charge collection time and therefore the trapping probability.
In case of the ALPIDE sensor, the depletion starts at the junction of the collection electrode and expands with increasing reverse bias (see figure 5.22), but it is difficult to laterally extend the depletion region far into the epitaxial layer in between the low resistivity substrate and the deep p-well, as this requires a potential gradient or an electric field in between two equipotentials [64].
A way to reach full depletion while keeping the collection electrode and hence the pixel capacitance small is to implement an additional planar p-n junction. This can be achieved by a lightly-doped n-type implant in the epitaxial layer as illustrated in figure 3.21 [64]. This was first tested with the so-called Investigator [65] chip. The depletion starts now at the junction and for reverse bias voltages of a few volts it reaches the collection electrode. The radiation tolerance of the process was validated through uniform high efficiency measurements on a test chip after neutron irradiation up to a fluence of $1 \cdot 10^{15}\,\mathrm{n_{eq}/cm^2}$ [65]. Large scale prototypes with different readout architectures were produced using this modification of the standard process. They are called MALTA and TJ MONOPIX [36, 66].

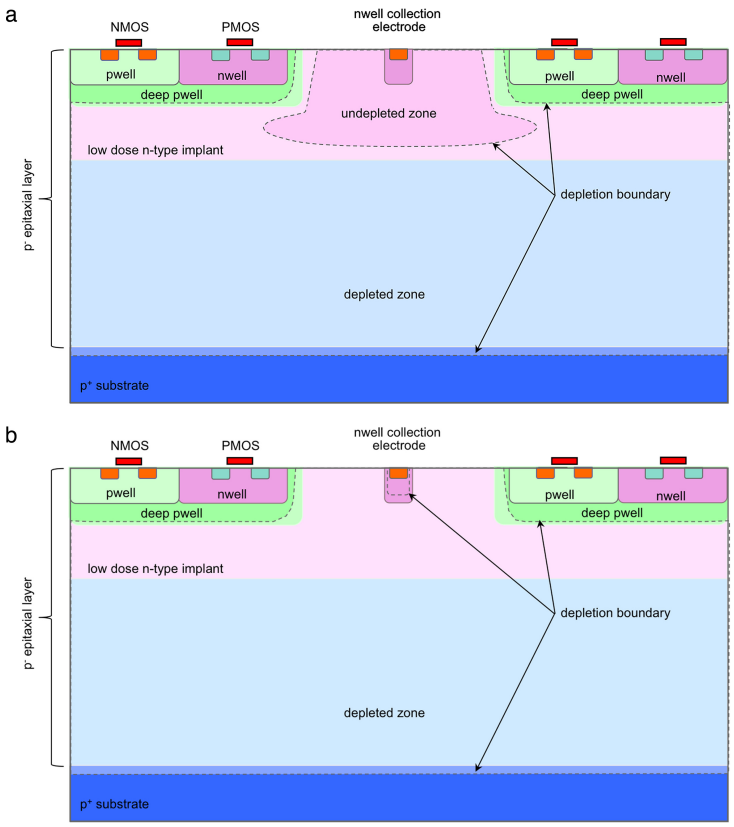

Figure 3.21: Illustration of modifications to the ALPIDE concept without bias (top) and with a bias of a few volts (bottom) [64]

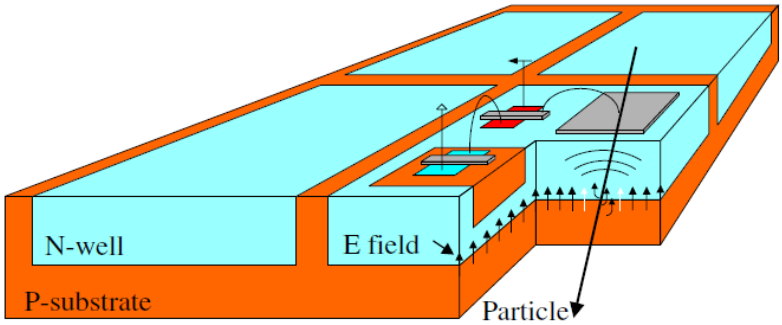

Figure 3.22: Schematic drawing of an HV-MAPS [67]

HV-MAPS

One way to achieve charge collection via drift in a monolithic architecture is to implant large charge collection electrodes in the form of deep n-wells (see figure 3.22) into a substrate with standard or comparatively low resistivity (ca. 20 Ωcm - 1 kΩcm) and apply a high reverse bias voltage of ca. 100 V. This results in a width of the depletion layer of $\mathcal{O}(10\,\mu m)$. Front-end readout electronics can be implemented inside the n-wells, while it has to be taken care of in its design that it does not interfere with the charge collection. The large collection electrode and the electronics inside of it result in a large pixel capacitance and therefore smaller signals compared to the ALPIDE approach. Consequently, HV-MAPS require more amplification, which results in a larger power consumption and a higher noise level.
The characterization of a specific HV-MAPS prototype, ATLASPix_Simple, is the subject of this thesis and its architecture is discussed in detail in chapter 4. It is based on a series of so-called MuPix prototypes, which were produced for the Mu3e experiment [68].

Chapter 4

Introduction to ATLASPix1/ATLASPix_Simple

The objective of this thesis is the characterization of the HV-MAPS prototype ATLASPix_Simple. The chip is part of a die, called ATLASPix1, which comprises three sensor prototypes produced to demonstrate the suitability of the HV-MAPS technology for the ATLAS ITk upgrade (see section 2.2.3). Figure 4.1 shows the layout of the ATLASPix1 reticle, indicating the three sensors ATLASPix_Simple, ATLASPix_IsoSimple, and ATLASPix_M2, whose differences are pointed out at the end of this section.

The reticle was produced by ams in the aH18 HV-CMOS process using wafers with different nominal[1] substrate resistivities of 20 Ωcm (standard), 80 Ωcm, 200 Ωcm, and 1000 Ωcm. The three ATLASPix1 sensors are based on the HV-MAPS concept introduced in section 3.5.2. They consist of active pixels hosting analog circuitry implemented inside deep n-wells that represenst the sensing diodes. Each pixel has its own signal line to the chip's periphery. The latter includes a phase locked loop (PLL), time stamp generators, the readout state machine and an 8b/10b encoder and serializer block. Most of these parts are similar for the three sensors and will be discussed in more detail for ATLASPix_Simple in section 4.1. In contrast to the so-called MuPix prototypes, which ATLASPix1 is based on, all three ATLASPix1 sensors have the comparator implemented inside the active pixel instead of the periphery. In the following, the distinguishing features of the three ATLASPix1 sensors are shortly pointed out.

[1] The non-standard substrate resistivities can vary between (50-100) Ωcm, (100-400) Ωcm, and (600-1100) Ωcm, respectively [70].

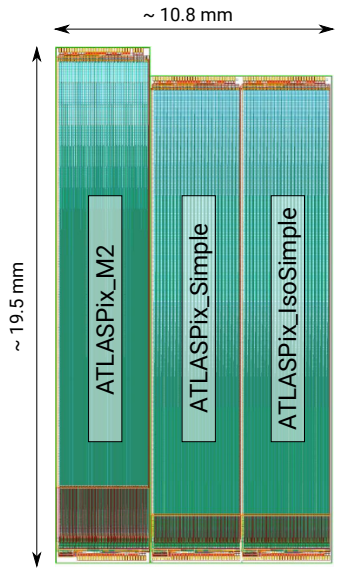

Figure 4.1: Layout of the ATLASPix1 reticle

ATLASPix_Simple

ATLASPix_Simple is the main subject of this thesis and is discussed in detail in the next section (4.1). One difference to ATLASPix_M2 is that is has one point-to-point connection from each pixel to the periphery, which results in a dense routing and sets a limit on the minimum possible pixel size in one dimension. The other main difference concerns the readout scheme, which is continuous and does not use on-chip trigger buffers.

ATLASPix_IsoSimple

ATLASPix_IsoSimple is identical to ATLASPix_Simple except for the implementation of the comparator. It has a deep p-well inside the deep n-well, which is non-standard in the aH18 process. It isolates pMOS transistors from the deep n-well and therefore allows for the use of a CMOS comparator inside the active pixel, while ATLASPix_Simple uses an NMOS comparator. CMOS logic in general has a lower power consumption and is expected to have a higher radiation tolerance since nMOS transistors are more prone to radiation induced leakage currents (see section 3.3.1).
Results on the performance of ATLASPix_IsoSimple are presented in chapter 6 and are compared to the results obtained with ATLASPix_Simple.

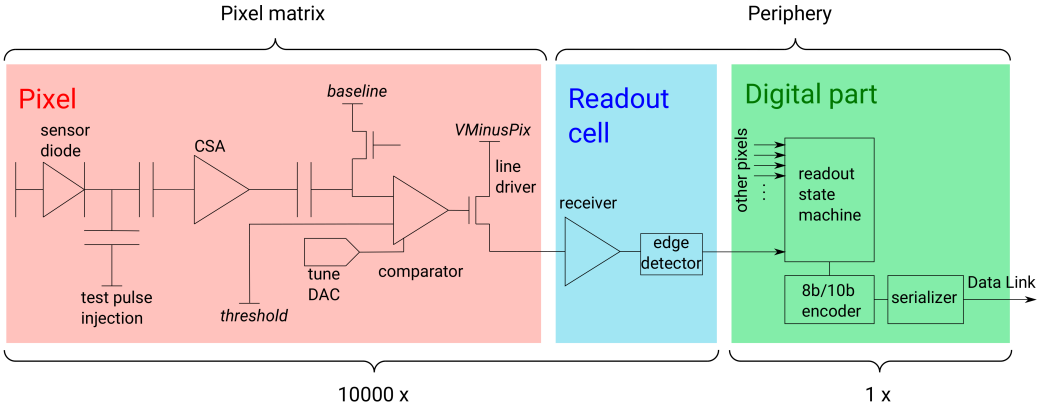

Figure 4.2: Schematic of the signal chain of ATLASPix_Simple

ATLASPix_M2

In contrast to ATLASPix_Simple, ATLASPix_M2 is equipped with on-chip buffers that can store hit information until the arrival of a trigger signal. Groups of 16 pixels share four buffers and the pixel addresses within these groups are encoded in eight bits. This reduces the number of signal lines from the pixel matrix to the periphery by a factor of two compared to ATLASPix_Simple and thus allows for a smaller pixel size of $60 \times 50\,\mu m^2$ compared to $130 \times 40\,\mu m^2$. The in-pixel amplifier and comparator are the same as for ATLASPix_Simple.
ATLASPix_M2 was not operated within the scope of this thesis and is not further discussed in the following.

4.1 Architecture of ATLASPix_Simple

ATLASPix_Simple has 25×400 pixels with a size of $130 \times 40\,\mu m^2$, resulting in an active area of $3.25 \times 16.0\,mm^2$. The signal chain from the sensor diode to the data output link is illustrated in figure 4.2.
Inside the deep n-well of each pixel a charge sensitive amplifier, a comparator, and a signal driver are implemented (see section 4.1.1). For each pixel, there is a point-to-point connection to its partner cell in the chip's periphery, which is referred to as the pixel's readout cell (see section 4.1.2) throughout this thesis. Here, a receiver and an edge detector are implemented. When a hit occurs, a hit flag is raised and two timestamps (see section 4.1.4) are stored. The on-chip state machine controls a continuous column-drain readout (see section 4.1.3). The data is sent off chip serially, zero-suppressed, and 8b/10b-encoded via one LVDS link with up to 1.6 Gbit/s depending on the input

Name	Voltage / V
VDD	1.9
VDDA	1.9
VSSA	1.0
VMinusPix	~ 0.8
VGatePix	2.2
HV	~ -60

Table 4.1: Required supply voltages

clock frequency. All clocks needed on the chip are generated from a fast clock, which is in turn generated by an on-chip PLL from the input clock and has five times its frequency.
Changes to the chip configuration can be made via shift registers connected to digital-to-analog converters (DACs) and configurable logic elements.
The chip requires six supply voltages. They are listed in table 4.1. According to the specifications of the aH18 process, the reverse bias voltage of the sensor diodes should be able to be as low as $-120\,\mathrm{V}$. However, an earlier breakdown is observed (see section 5.3.1).
Several features are implemented on the chip for testing and characterization purposes. There is the possibility to inject a test pulse into each pixel. All pixels of column 0 have an analog test output behind the amplifier (see section 4.1.1). Another test output, called Hitbus, allows for probing the signal behind the receiver in the readout cell (see section 4.1.2). This signal is representative of the comparator output. The Hitbus is implemented as the logical 'or' of all receiver outputs of blocks of 200 pixels within one column.
In the following subsections, the features mentioned above are discussed in more detail.

4.1.1 Active pixel

The pixel size is $130 \times 40\,\mu\mathrm{m}^2$. The layout of one pixel is shown in figure 4.3 [70]. It is surrounded by a p-type guard ring. The charge collection electrode is realized as a deep n-well (indicated by the outer red line) inside the p-type substrate. The resulting diode is reversely biased with a voltage (HV) of ca. $-60\,\mathrm{V}$. The deep n-well is connected via a high-ohmic transistor chain, which acts as a large variable (DAC: VNBiasPix) resistor, to VDDA. Its potential is floating within some margin due to changes in the electric field that are induced by the drift of signal charges. The in-pixel electronics is designed to minimize the influence of the resulting body effect (see section 3.2). It

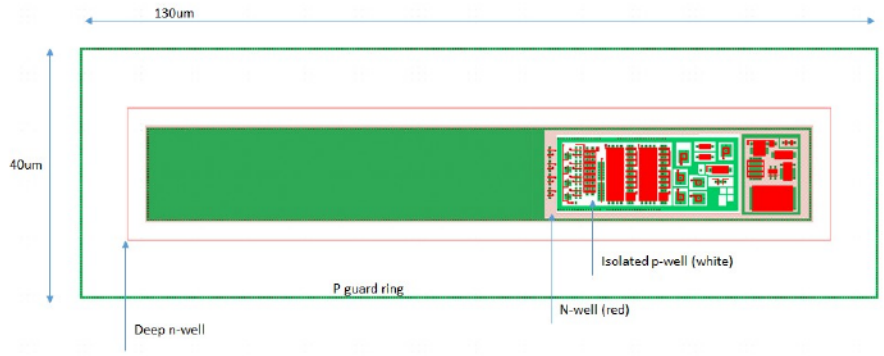

Figure 4.3: Layout of one active pixel [70]

includes a charge sensitive amplifier (CSA), a comparator and a driver for the signal line to the readout cell. The critical nMOS transistors are gate-enclosed to improve radiation tolerance (see section 3.3.1). The bulk material of all nMOS transistors is a shallow p-well (indicated in white), embedded in the deep n-well. The bulk material of the pMOS transistors is realized by a shallow n-well (red region surrounding the p-well), which is ohmically connected to the deep n-well. To avoid interference of switching transistors with other parts of the circuit, the comparator is implemented using only nMOS transistors, which are capacitively decoupled from the deep n-well by the p-n juntion between the latter and the shallow p-well.

A schematic of the in-pixel electronics is shown in figure 4.4 [69]. Voltage levels written in blue can be configured via on-chip DACs. Baseline (BLPix) and threshold (ThPix) of the comparator can be additionally connected to external voltage sources to ensure stable operation in case the DACs cannot supply the required current. The same is true for VDD_RAM. The in-pixel RAM cells are used to store three bits for tuning the threshold of the individual pixel and one bit for switching it off.
Figure 4.5 shows a schematic of the NMOS comparator and the line driver. The comparator works similar to a typical two-stage CMOS comparator. The CSA output pulse is modulated via a capacitance onto the fixed baseline voltage BLPix that is coupled via a variable resistor (DAC: BLResPix) to the gate of the comparator's input transistor M1. The first comparator stage, which includes the transistors M1 and M2, acts as a differential amplifier that amplifies small voltage differences with a large gain. When there is no signal, the gate voltage of the threshold transistor M2 is significantly larger than that of M1. Most part of the current in the first stage, which is limited by M5, flows through M2. The voltage level U_{th} is low and U_{out1} is

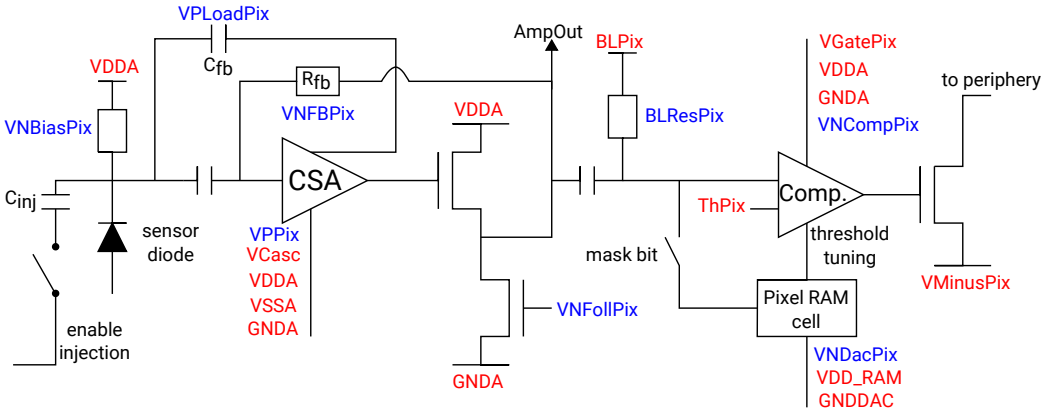

Figure 4.4: Schematic of the in-pixel electronics [69]

high. When there is a signal that is large enough such that the gate voltage of M1 exceeds that of M2, then most of the current flows through M1. This current is limited by M3, which is in saturation, and therefore the voltage level U_{out1} has to drop. The current in the second arm of the first stage is now lower than before so U_{th} rises. The voltage levels would asymptotically approach the respective high and low levels close to VDDA and U_5 if it weren't for the transistors M3 or M4 being in saturation, which reduces the output range but defines high and low levels which are reached fast by U_{th} and U_{out1}. When the signal ends, U_{th} and U_{out1} switch back to their initial state.
The difference to a CMOS comparator is that M3 and M4 are nMOS transistors instead of diode-connected pMOS transistors. Ensuring that they are in saturation requires the additional voltage VGatePix, which has to be larger than VDDA.
The second comparator stage acts in the same way as the first stage but its input voltages are U_{th} and U_{out1}, which already have a large difference, such that the output level U_{out2} switches faster than U_{out1}. The second stage is therefore called gain-stage. Note that U_{out2} is inverted with respect to U_{out1}, i.e. when a signal occurs, U_{out1} switches from the high level to the low level and U_{out2} from the low level to the high level.
The driver for the signal line to the readout cell uses only one transistor, M6, which acts as a switch. Its gate is connected to U_{out2}. When there is no signal, the switch is off and the voltage level of the signal line is pulled up to a high level via a pMOS transistor in the readout cell. When U_{out2} switches to its respective high level, M6 can conduct current and the level of the signal line is pulled down to the level VMinusPix, creating the signal pulse on the line.

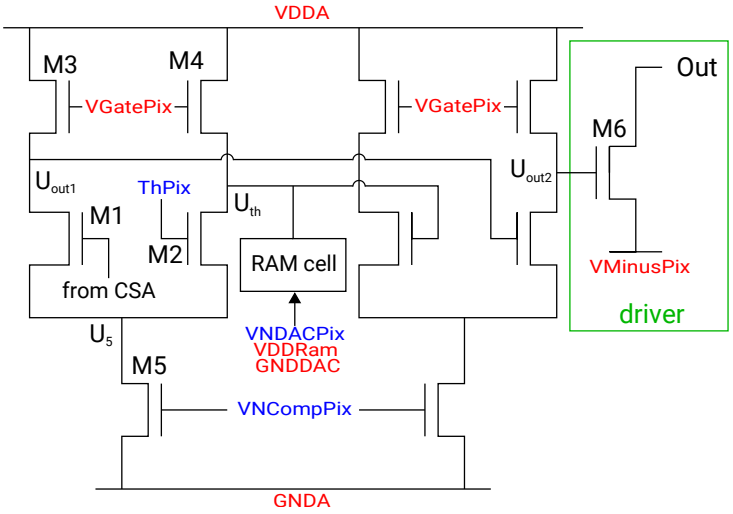

Figure 4.5: Schematic of the comparator and the line driver [69]

4.1.2 Readout cells

There is one readout cell for every pixel. They take up most of the space in the chip's periphery. One cell is $62.5 \times 4.2\,\mu m^2$ large, i.e. it has approximately half the width of a pixel. This stems from the cells being arranged in a "double column" structure of two blocks of 200 cells below one pixel column. The cells of the left block are connected to the lower 200 pixels of the associated column and those of the right block to the upper 200 pixels. The routing scheme is illustrated in figure 4.6 [69]. The different colors of the signal lines correspond to different metal layers.

In the readout cell, the signal coming from the pixel is converted to a digital signal with the logic levels GND and VDD by the receiver. A schematic is shown in figure 4.7 [69]. An edge detector creates a short digital pulse synchronous to the leading edge of the received signal. It raises the hit flag and enables the storage of the first timestamp (see section 4.1.4) in a RAM. A second timestamp is stored upon the crossing of the comparator threshold by the trailing edge of the signal directly without edge detection. The row address of each pixel is hardwired in its corresponding readout cell. In between the receiver and the edge detector the signal is tapped for a test output, the Hitbus, which is implemented as the logical 'or' of the signals of blocks of 200 pixels within one column.

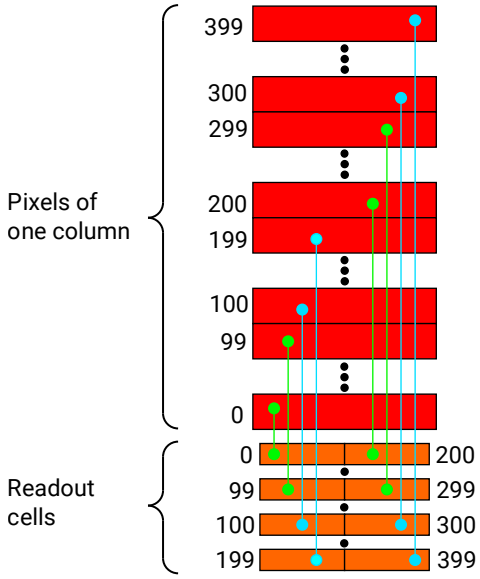

Figure 4.6: Illustration of the arrangement of the readout cells and the routing of the signal lines from the pixels to the readout cells [69]

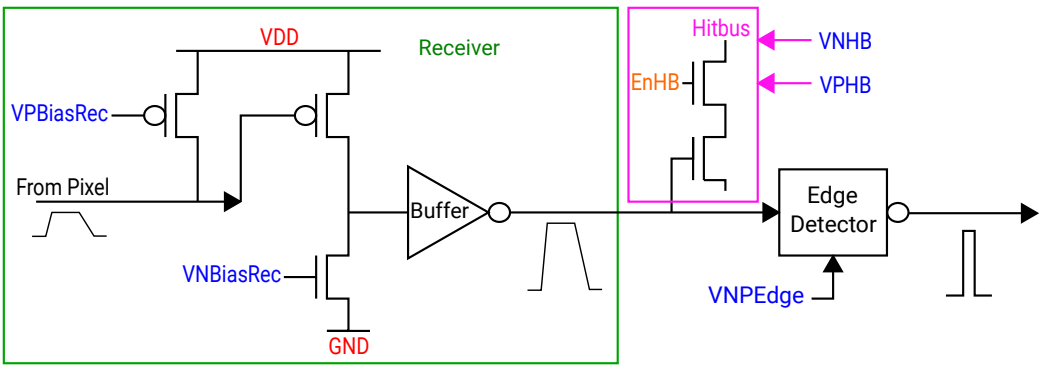

Figure 4.7: Schematic of one readout cell [69]

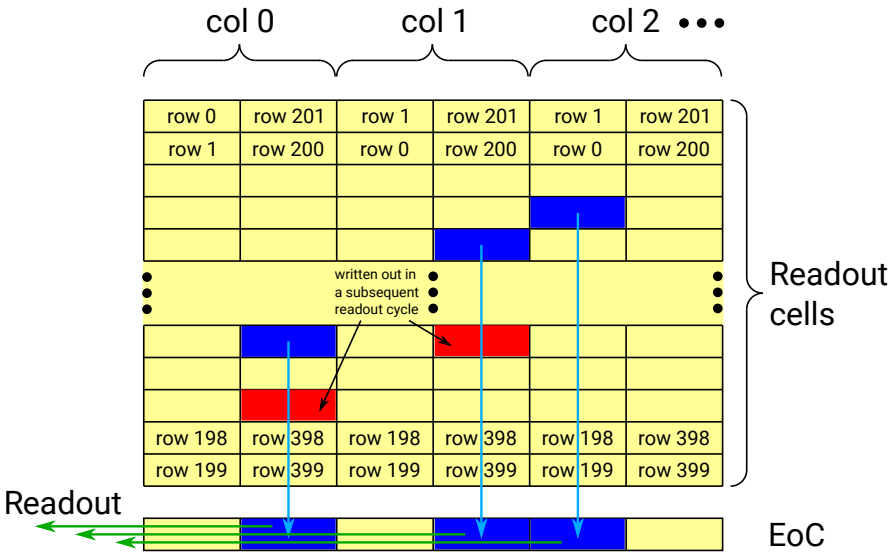

Figure 4.8: Illustration of the column-drain readout scheme of ATLASPix_Simple

4.1.3 Readout state machine

The readout scheme of ATLASPix_Simple is illustrated in figure 4.8. For every block of 200 readout cells, there is one so-called end of column (EoC) cell, i.e. there are two EoC cells per pixel column. A priority logic ensures that for every block of readout cells only the data of the hit with the smallest row address is copied to the EoC, which stores the column address. Controlled again by a priority logic, the hit data in the EoC is sent to the serializer once per readout cycle. Note that this readout scheme does not retain the chronology of hits.

A state diagram of the on-chip state machine is shown in figure 4.9 [72]. It operates in one of two possible modes. In the send-counter mode it continuously outputs the value of an on-chip 24-bit counter. In the pixel-readout mode it sequentially sends the PullDown (PD), LoadColumn (LdCol), LoadPixel (LdPix), and ReadColumn (RdCol) signals to the EoC. For every signal, there are two states. In state 1 the signal is sent and in state 2 the value of the data output is updated and the signal is released. Upon PD the data buses from the readout cells to the EoC are cleared. Upon LdCol the first hit in the priority logic of each readout cell block is transferred to the EoC. Upon LdPix new hits are stored in the readout cells. Upon RdCol the hit data stored in the EoC is sent to the serializer, one hit at a time.

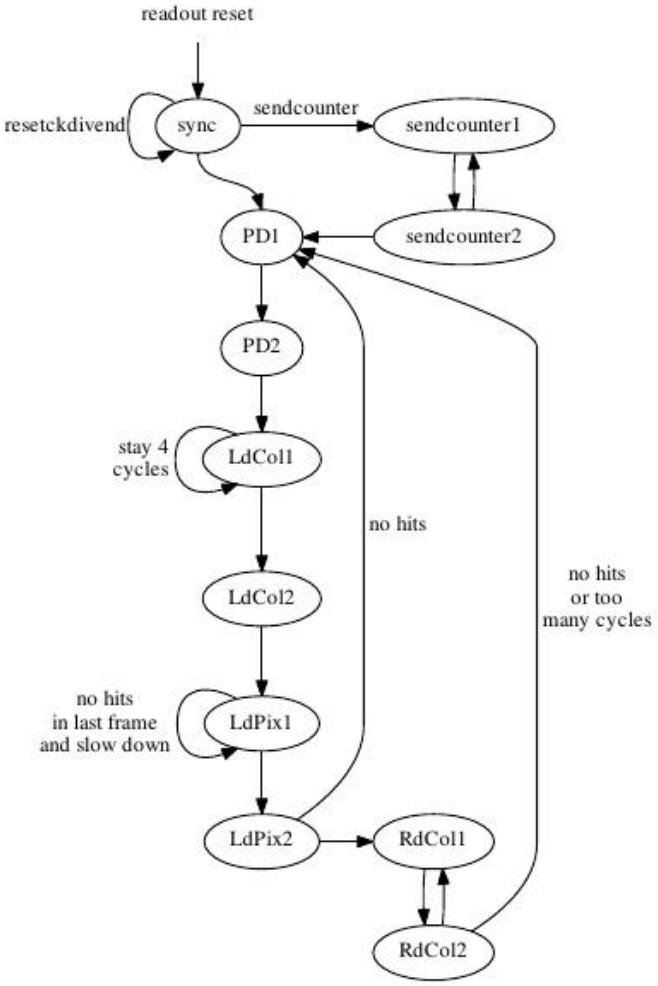

Figure 4.9: State diagram of the ATLASPix_Simple on-chip state machine [72]

The on-chip PLL derives a fast clock from the input clock with five times its frequency. All other clocks required on the chip are derived from the fast clock. The hit data undergoes several steps of serialization and is 8 bit/10 bit-encoded before it is sent off chip via one LVDS link, synchronized with both edges of the fast clock, resulting in a readout speed of 1.25 Gbit/s for an input clock frequency of 125 MHz. In the context of this thesis, the chip was always operated at this frequency. The link is specified to work reliably up to a speed of 1.6 Gbit/s.
The same state machine is implemented in the HV-MAPS prototype MuPix8, for which it is described in more detail in [72].

4.1.4 Timestamps

Apart from the row and the column address, the output data of each hit consists of two timestamps:
The first timestamp - in the following referred to as TS1 - is ten bits wide and its sampling is triggered by the leading edge of the comparator output. It represents the time of arrival of a hit.
The second timestamp - in the following referred to as TS2 - is six bits wide and its sampling is triggered by the trailing edge of the comparator output. The difference of both timestamps equals the time over threshold (ToT):

$$\mathrm{TS2} - \mathrm{TS1} = \mathrm{ToT} \tag{4.1}$$

The timestamps are realized by Gray code counters and are distributed to every readout cell, where they are stored upon the occurrence of a hit until the latter is read out. At an input clock frequency of 125 MHz, TS1 has a maximum precision of 16 ns bins. TS2 can be twice as precise. The binning of both timestamps can be made coarser by factors of integers up to 15 specified via configuration bits. Note that, for the simplified equation 4.1 to hold, TS1 and TS2 have to have the same unit and possible redundant most significant bits of TS1 have to be disregarded. This becomes relevant when the two timestamps are configured to run at different frequencies, e.g. to cover the full ToT spectrum ($\mathcal{O}(1\,\mu s)$) with TS2, while at the same time having the maximum precision for the time of arrival (TS1).

Chapter 5

Characterization of ATLASPix_Simple

This chapter represents the central part of this thesis. Two different types of ATLASPix_Simple samples were investigated, samples with a nominal substrate resistivity of 80 Ωcm and a nominal thickness of 70 µm and samples with a nominal substrate resistivity of 200 Ωcm and a nominal thickness of 100 µm. Section 5.1 introduces the setup that is used to configure and read out ATLASPix_Simple and the reference systems that are used to measure the time of arrival of particles and to reconstruct their tracks. Section 5.2 gives an overview of the utilized testbeam facilities. Measurement results are devided into three sections. In section 5.3, the performance of unirradiated ATLASPix_Simple samples is investigated based on laboratory and testbeam measurements. While the analyses in this section are performed either for the chip as a whole or on a single-pixel level, results of analyses with sub-pixel spatial resolution are presented in section 5.4. Finally, section 5.5 focuses on the performance of ATLASPix_Simple after irradiation with protons and neutrons.

5.1 Setups

The system used within the scope of this thesis to operate and characterize ATLASPix_Simple was developed over the course of the characterization of several successive HV-MAPS (MuPix) prototypes. In its latest iteration it can be used with different sensors that are similar to ATLASPix_Simple with a minimum amount of adaptations. It has been used with ATLASPix_Simple, ATLASPix_IsoSimple, MuPix7, MuPix8, and MuPix9.
The setup used to power, configure, and read out a single ATLASPix_Simple

sensor is described in section 5.1.1. The same system is used to build up a beam telescope by adding additional sensor layers. The telescope setup is used to characterize the device under test (DUT) using particle tracks from a testbeam as reference. The telescope setup is described in section 5.1.3. The sensors used for the telescope layers have a timing precision of 8 ns bins. Consequently, they cannot be used as a reference system for timing studies. Therefore, timing detectors are added to the system (see section 5.1.2). Measurements with sub-pixel spatial resolution were carried out using a different reference telescope, the DURANTA telescope at DESY. It is introduced in section 5.4 since it is independent of the system discussed in this section.

5.1.1 Operation of a single sensor

The most basic form of the setup is used to power, configure, and read out a single ATLASPix_Simple sensor, e.g. for lab measurements. From front- to back-end it consists of

- the so-called "insert" PCB that the sensor is bonded to,
- the mother PCB, whose features include input/output connections, repeaters, and voltage DACs,
- a SCSI/HSMC adapter card,
- an FPGA board,
- a PC.

Figure 5.1 (adapted from [69]) shows a schematic of the setup. In the following, the hardware components and briefly also the main functionality of the firmware are described. The software is covered in section 5.1.4.

Insert PCB

The sensor is wire-bonded to the so-called insert PCB. It connects the sensor's input inputs and outputs to the mother PCB via a 50-pin edge connector. It is the only hardware component that is specifically designed for every sensor type that is used with the setup. However, it is the same for all three ATLASPix1 chips, which have an almost identical pad layout. The three chips are not foreseen to be cut apart. One of the three sensors can be bonded according to how the die is placed on the PCB. Figure 5.2 [69] is a photo of an insert PCB with ATLASPix_Simple bonded to it.

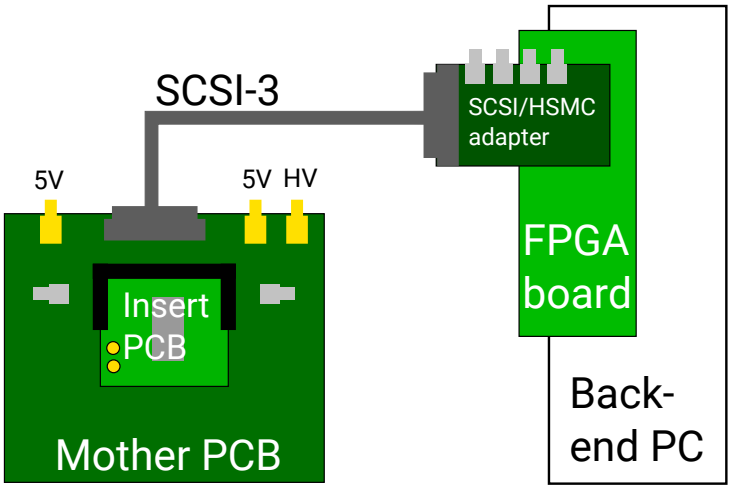

Figure 5.1: Schematic of the setup used to operate a single ATLASPix_Simple sensor;
modified from [69]

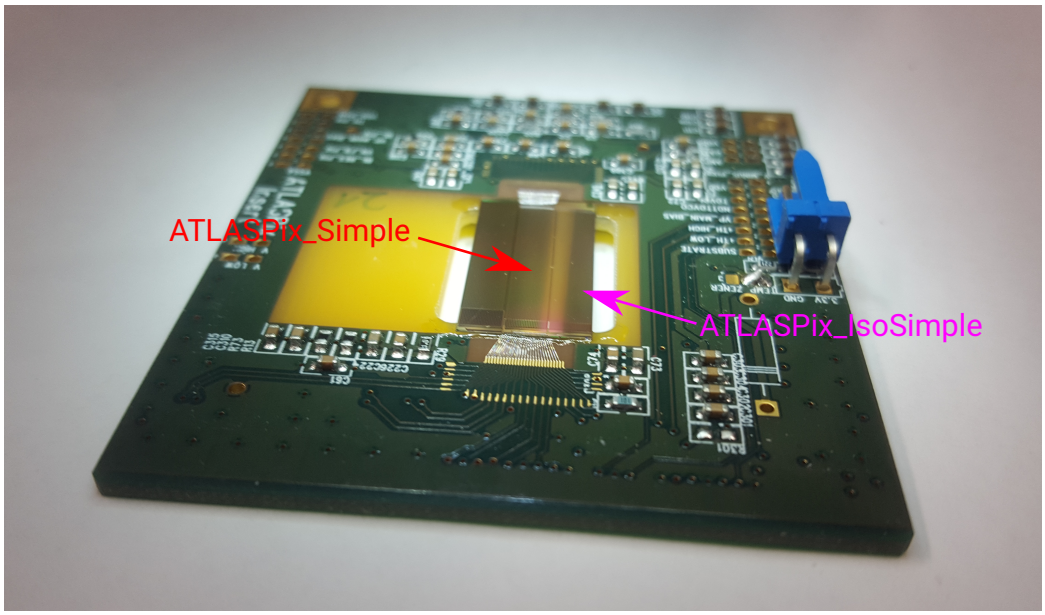

Figure 5.2: Photo of an insert PCB with bonded ATLASPix_Simple [69]

The reticle is glued to the PCB only at its top and bottom edges. Underneath most part of it there is a hole in the PCB. The metal layers are kept out of this part of the PCB. The hole reduces the scattering of particles for testbeam measurements. Furthermore, it enables the cooling of the sensor using the method described in section 5.5.2.
The ATLASPix1 insert PCB is populated only with passive components. ATLASPix_Simple requires the external supply of the voltage VGatePix = 2.2 V. The maximum voltages that are supplied to the edge connector by the mother PCB are VDD and VDDA (1.9 V). Therefore, the insert PCB features a two-pin connector and a simple voltage divider to supply 3.3 V directly from the mother PCB via a cable and generate the required 2.2 V. Besides that the PCB features protective and filtering circuitry as well as testpoints.

Mother PCB

Figure 5.3 [69] is a photo of a mother PCB with a connected ATLASPix1 insert PCB. To fully operate a sensor, it has to be connected to power supplies via three SMA connectors. One of them gets connected to the HV power supply. The connection is simply routed through to the chip. The other two inputs both require 5 V. They are used to power all the active components on the PCB, i.e. voltage regulators, DACs, LVDS receivers and repeaters. The connection to the FPGA card inside the back-end PC is realized via SCSI-3 (Small Computer System Interface).
The main supply voltages for the sensor, VDD, VDDA, and VSSA, are generated by voltage regulators, where VDD and VDDA can be adjusted via potentiometers. Alternatively, when setting the corresponding solder jumpers accordingly, the three voltages can be directly applied to the chip via an external power supply, bypassing the voltage regulators. Separate voltage regulators are used to create reference voltages from which BLPix, VMinusPix, and VDD_RAM are generated via adjustable voltage dividers. A 3.3 V reference voltage is connected via a cable to the insert PCB to generate VGatePix, as mentioned above.
ThPix is generated by a DAC. So are the injection pulses with configurable height, length, and frequency.
The LVDS slow control signals coming from the FPGA are transformed by the LVDS receivers into single-ended signals, as required by the sensor. The data coming from the chip is driven over the SCSI cable by the LVDS repeater.
The mother PCB features a cutout which is aligned with that of the insert PCB.

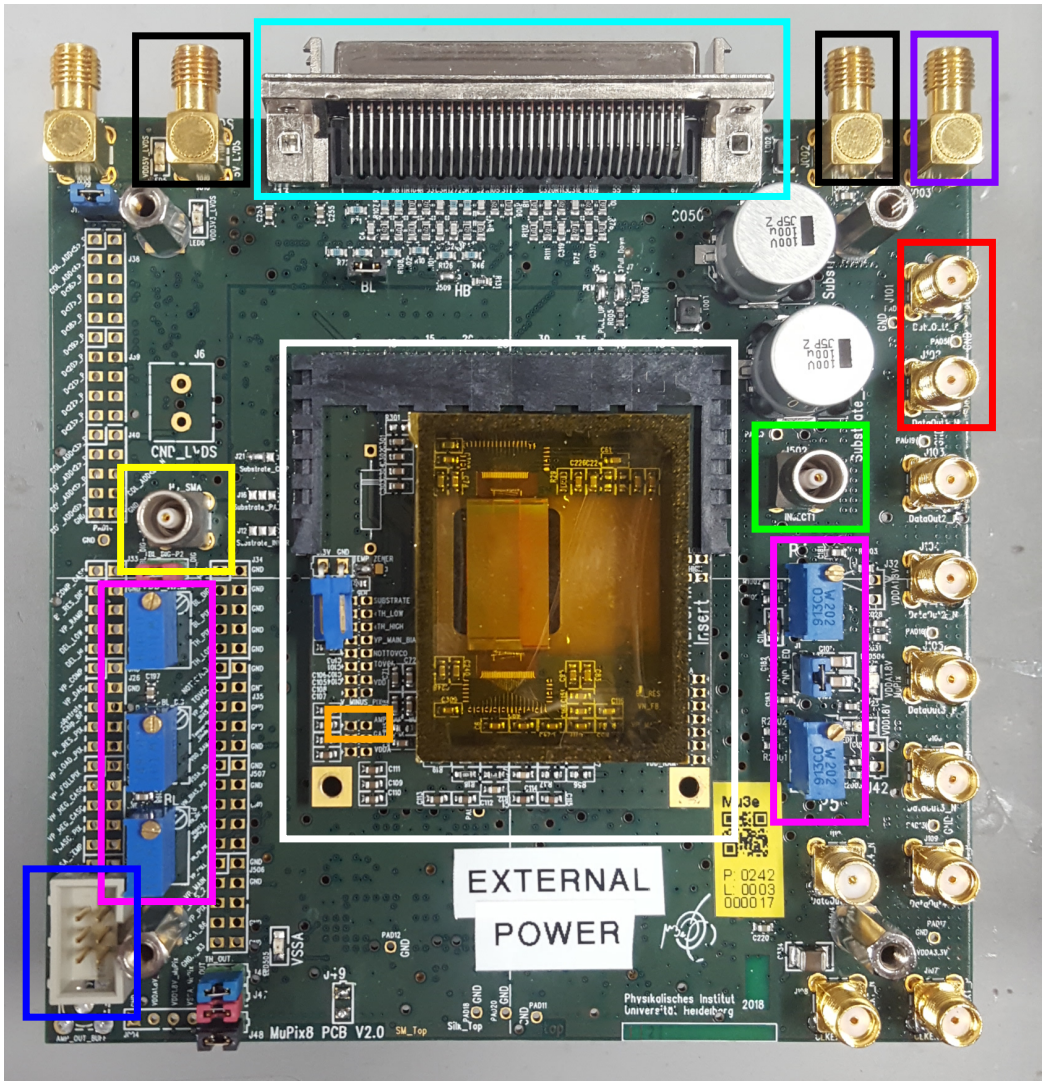

Figure 5.3: Photo of the mother PCB with ATLASPix1 insert PCB plugged in (white), SCSI-3 connector (cyan), SMA connector for HV (purple), SMA connectors for 5 V (black), potentiometers to adjust reference voltages (magenta), connector for optional direct power supply (blue), injection output connector (green), Hitbus output connector (yellow), AmpOut testpoint (orange), optional LVDS data output connectors (red) [69]

SCSI/HSMC adapter card

The SCSI/HSMC adapter card is required for interfacing the SCSI-3 connection from the mother PCB and the HSMC (High Speed Mezzanine Card) port on the FPGA board. Note that there are two SCSI ports per card to connect two mother PCBs to one HSMC port in parallel. This is relevant for the telescope setup described in section 5.1.3. The card also features four NIM inputs for timing detector signals for the reference time measurement (see section 5.1.2) and an RJ45 connector that is required for the interface with a EUDET-type telescope (see section 5.4.1).

FPGA board and firmware

A commercial Stratix IV GX FPGA development board [71] is used for slow control and data acquisition (DAQ). The board has two HSMC connectors, i.e. up to four sensors can be connected via two SCSI/HSMC adapter cards. The communication with the back-end PC via PCIe (Peripheral Component Interconnect Express) is controlled by a custom driver. Data from one or more sensors is received, deserialized and 8 bit/10 bit-decoded by the FPGA. The hit data of one readout cycle of one sensor is combined to a data block. The sensor ID is added to the data of each hit. A header is added to each block. It contains a 64-bit timestamp with a bin size of 2 ns, which is generated on the FPGA. Up to 500 Mbit of data can be buffered using the on-board DDR3 RAM.
The FPGA also receives the bit streams for sensor configuration from the PC and sends them further to the sensors with selectable frequency.
A detailed description of the firmware can be found in [72].

5.1.2 Reference time measurement

To measure the time resolution of a sensor, the time of arrival of a particle has to be known, which requires a precise reference measurement. As mentioned above, the SCSI/HSMC adapter card features NIM inputs for this purpose. A discriminated signal pulse from any timing detector can trigger the sampling of a 500 MHz timestamp counter running on the FPGA. There are four inputs and one can chose to either assign a hit to every individual signal or to the coincidence signal, which is generated directly on the FPGA. In between data blocks of sensor hits (see previous section 5.1.1), the FPGA sends blocks of timing detector hits to the PC. In the context of this thesis, plastic scintillators read out with photomultiplier tubes (PMTs) or silicon photomultipliers (SiPMs) were used as timing detectors. Most measurements

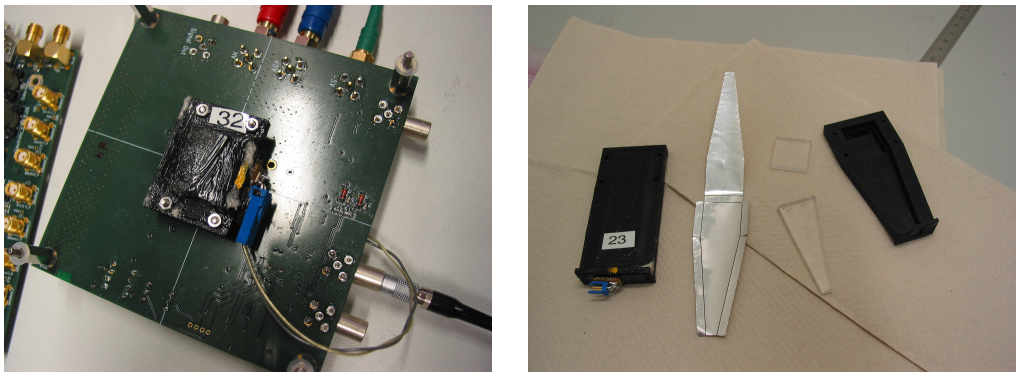

(a) (b)

Figure 5.4: Photos of the scintillator tile PCB (a) and a dismounted tile with light guide, wrapping foil, and mouting shell (b) [74]

were performed using a scintillating tile together with a SiPM, mounted to a custom PCB, which contains a discriminator and the required power and signal connections. The PCB is designed such that it can be integrated in the mechanical setup of the MuPix telescope, which is discussed in the following section 5.1.3. Figure 5.4 [74] shows photos of (a) the PCB with a mounted tile and (b) a dismounted tile, a lightguide, the reflective foil they get wrapped in, and the shell they get enclosed in together with a SiPM. The time resolution of the system is approximately 2 ns [74].

5.1.3 Telescope setup

This section introduces the telescope setup that was used for most testbeam measurements discussed in this thesis. Before that, the concept of a beam telescope is introduced.

Concept of a beam telescope

The terms beam telescope or tracking telescope refer to a system of several layers of pixelated particle detectors that are placed consecutively in a particle beam as illustrated in figure 5.5 [72]. The arrow depicts the track of a single beam particle, which can be reconstructed from the positions of the pixels that are hit. The track information is used to characterize a DUT, which is usually placed in between the telescope layers. To measure the point on the DUT where a hit should occur as precise as possible, a high spatial resolution of the telescope (pointing resolution) is required. This is achieved by a small pixel size in combination with a low material budget to minimize

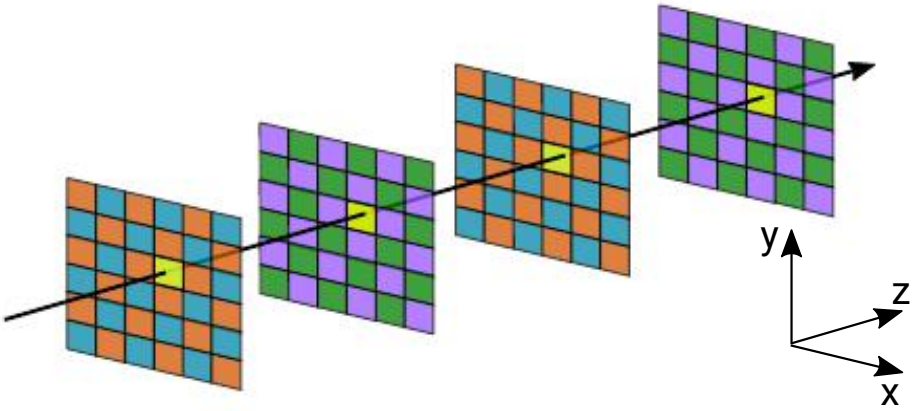

Figure 5.5: Illustration of the concept of a beam telescope [72]

multiple scattering. Furthermore, it is desirable to know the exact time when a particle traverses the DUT, which requires a high time resolution of the telescope.

The MuPix telescope

The so-called MuPix telescope (see figure 5.6) is a scaled-up version of the setup used to operate ATLASPix_Simple (see section 5.1.1). It was used for most testbeam measurements discussed in this thesis.
The input/output connections of the FPGA board allow for connecting four mother PCBs via two SCSI/HSMC adapter cards. Therefore, three telescope layers plus the DUT are connected in the standrad configuration. During data taking, all four sensors are treated the same. The FPGA simply sends blocks of hit data to the PC for each sensor. Only when performing the data analysis, the DUT has to be specified. In general, every layer can be chosen as DUT.
The described setup is referred to as MuPix telescope because it was developed using MuPix prototypes. As mentioned before, the same system can be used to operate different MuPix/ATLASPix-like sensors. It is also possible to operate the MuPix telescope with mixed sensor types. Typically, MuPix8 sensors are used as telescope layers to characterize ATLASPix_Simple. Their active area is larger than that of ATLASPix_Simple, ensuring a full overlap. HV-MAPS are generally suited for building tracking telescopes due to their small thickness, high rate capability, and comparatively high time resolution. Their drawback, up to the time of writing this thesis, is a comparatively large pixel size. It results in a pointing resolution sufficient to perform sensor stud-

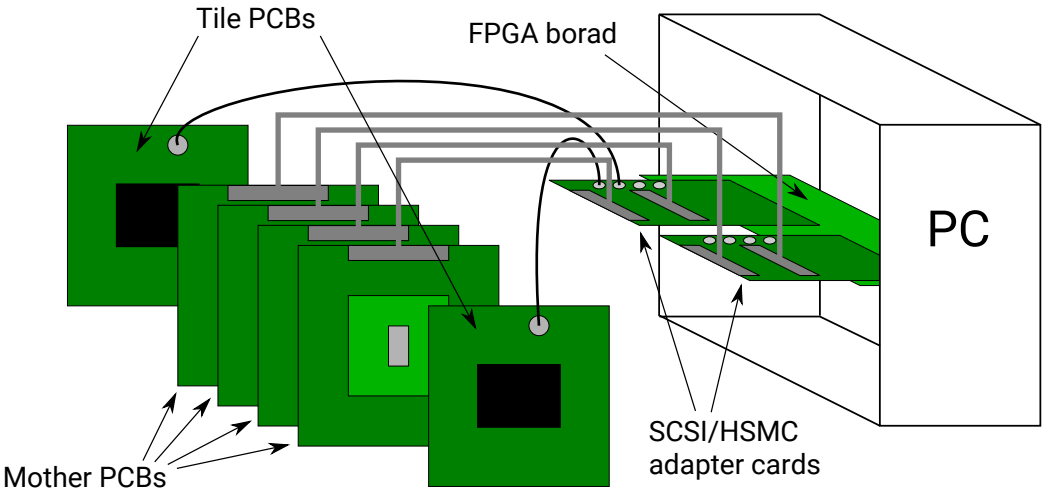

Figure 5.6: Schematic of the MuPix telescope setup

ies on a single pixel but not on a sub-pixel level.
To achieve a reference time measurement with a better resolution, the MuPix telescope is complemented by timing detectors, as described in the previous section 5.1.2.

Mechanical setup: One advantage of the MuPix telescope is its transportability and modularity due to its mechanical setup. It is realized using custom aluminum frames that both the mother PCB and the scintillator PCB can be mounted to. The frames feature micrometer screws for shifts in both directions orthogonal to the beam axis for mechanical alignment. The remaining parts of the setup are built from commercial components by Thorlabs (post holders mounted to a bottom plate).
Figure 5.7 shows a photo of multiple MuPix telescopes set up in a row at a testbeam.

5.1.4 Software

There is one software package to operate both a single sensor and the MuPix telescope. Note that the DAQ software includes several features like online efficiency calculation and direct memory access (DMA), which were not used within the scope of this thesis and are therefore not discussed here. A detailed description of the software package can be found in [73]. A conceptual overview is given in the following.

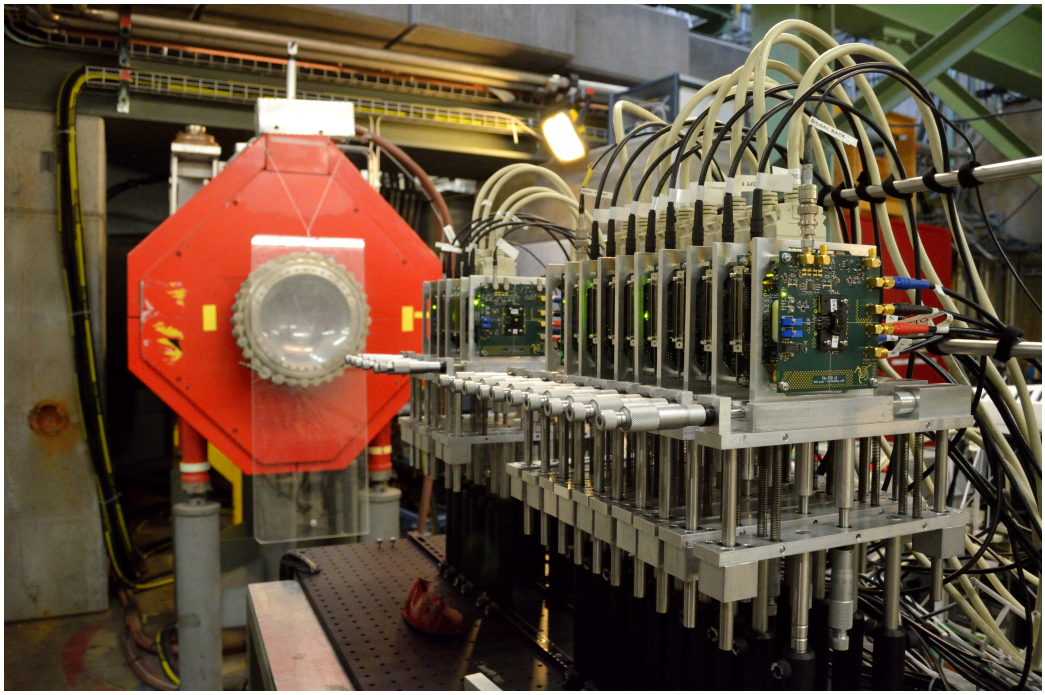

Figure 5.7: Photo of multiple MuPix telescopes set up in a row at a testbeam

DAQ

The multi-threaded DAQ software handles data readout, reformatting, and storage. The data transfer from the FPGA to the PC's FPGA-writable memory via PCIe is polling-based. A readout thread constantly checks for fully written data events, splits such events into the different block types, and copies them to a different memory location. Pointers to the data are forwarded to the so-called filewriter thread. The latter merges blocks of sensor hits and timing detector hits with similar timestamps and creates the final data object called telescope frame, which is stored on disk for offline analysis. In addition, an online-monitoring thread fills the data into hitmaps for all sensors that can be displayed by the graphical user interface (GUI) during data taking.

Sensor configuration

The sensor configuration can be manually entered in the GUI or read from a configuration file by DAC name. The mapping between DAC names and the position of the according bits in the configuration bit string is handled by a dedicated software class. The bits are sent to the FPGA, where they are written to a shift register. The mother PCB contains several DACs as well, e.g. for supplying the sensor's comparator threshold externally. These DACs are configured in the same way.

5.2 Testbeam facilities

All testbeam measurements discussed in this thesis were performed either at the testbeam facility at DESY or at PSI. Both facilities are briefly introduced in the following.

5.2.1 DESY

The testbeam facility at DESY [75] in Hamburg operates three beam lines at the electron/positron synchrotron DESY II. A bremsstrahlung beam is created by a carbon fibre target in the synchrotron. The photons are in turn converted into electron-positron pairs in a metal plate converter. The beam is dispersed horizontally with a dipole magnet, separating different particle momenta and polarities. The final electron or positron beam is cut out with a collimator while the beam energy and polarity are selected by setting the magnet current accordingly. The energy can be chosen within the range of 1 GeV to 6 GeV. The particle rate depends on several factors, e.g. the selected beam energy, the carbon fibre target, the collimator, and the frequency that bunches are injected with. Typical rates are $\mathcal{O}(10\,\mathrm{kHz/cm^2})$.
In addition to the beamline and the necessary infrastructure, the DESY testbeam facility provides users with EUDET-type beam telescopes, which are permanently installed in the beam areas (see section 5.4.1).

5.2.2 PSI

The Paul Scherrer Institute (PSI) in Switzerland operates a cyclotron in which protons are accelerated to a kinetic energy of 590 MeV. The so-called πE1 and πM1 secondary beam lines [76] were used for testbeam measurements in the context of this thesis. The main proton beam produces positive and negative pions and muons as well as positrons/electrons in the production targets E and M. Both beams consist of all three particle species with selectable polarity and pion momenta up to 500 MeV/c.
For the testbeam measurements at PSI that are discussed in this thesis, the data storage rate was limited to approximately 50,000 hits/($\mathrm{cm^2 \cdot s}$) per sensor. The data had to be buffered first and then written to disk due to the high beam rates that can go up to $\mathcal{O}(100\,\mathrm{MHz})$.

5.3 Basic sensor performance

In this section, results of measurements with unirradiated ATLASPix_Simple samples are presented. Current-voltage characteristics, power consumption, analog performance, noise and threshold dispersion, cluster size and crosstalk between signal lines, efficiency, noise, and time resolution are studied.

5.3.1 Current-voltage characteristic

The current-voltage characteristic of the reverse bias was measured using two samples with the nominal substrate resistivities of 80 Ωcm and 200 Ωcm. The sensors were powered during the measurements, which were performed once with active cooling and once without. The cooling setup is described in section 5.5.2. The sensor temperature was ca. 43 °C without cooling and ca. 0 °C with cooling.
The results are plotted in figure 5.8. They look as expected in that they show a small reverse leakage current of the order of 0.1 µA until the breakdown occurs und the current increases rapidly. The breakdown starts at an HV (U) of approximately −70 V. The production process used for ATLASPix_Simple is specified for voltages down to −120 V. It is not exactly kown what causes the "ealy" breakdown. The process had not been officially released at the time that ATLASPix1 was produced and it could be that the specification is not correct. Alternatively, it could be that design rules were violated by the design of the chip. At the time of writing, the observed breakdown behavior is being studied using TCAD (technology computer-aided design) simulations in the scope of a PhD thesis [78].

5.3.2 Power consumption

The results presented in this subsection were obtained in the scope of and presented first in a Master thesis [69].
There are three main power domains on the chip (excluding the reverse bias): VDDA (1.9 V), VSSA (1.0 V), and VDD (1.9 V). VSSA is only used in the active pixel matrix, VDD only in the periphery. VDDA is used in the active matrix and additionally in the periphery to power a custom-designed block that uses differential current mode logic (DCL) instead of CMOS logic. The contributions to the power consumption P_{VDDA} can be disentangled by switching off parts of the chip's components via the available DACs. The individual contributions to the chip's overall power consumption for a "default" sensor configuration (see appendix A1) are listed in table 5.1.

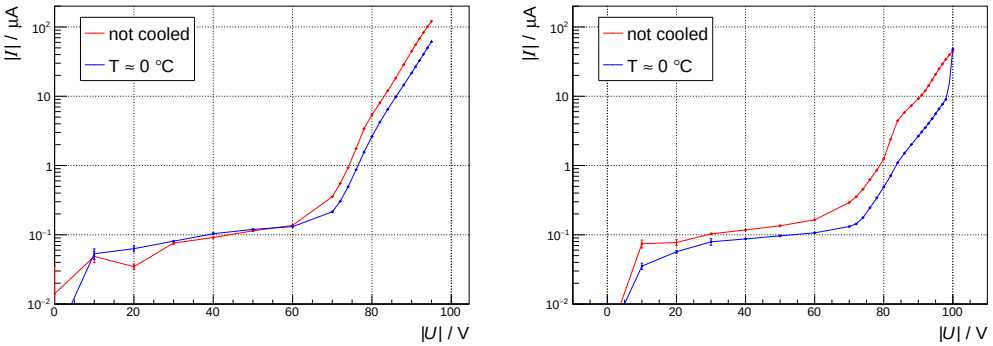

(a) 80 Ωcm (b) 200 Ωcm

Figure 5.8: Current-voltage characteristics of the reverse bias of ATLASPix_Simple, cooled and uncooled

	P_{VDDA} / mW	P_{VSSA} / mW	P_{VDD} / mW
Active pixel matrix	65.6	34.4	-
State machine	-	-	8.3
DCL	20.5	-	14.8
LVDS link	-	-	22.8

Table 5.1: Individual contributions to the overall power consumption of ATLASPix_Simple

The readout cells are powerded via VDD as well but no change in power consumption is observed when setting the corresponding DACs to zero or varying the hit rate.
The power consumption is measured by reading off the current at the power supply with a precision of 0.1 mA.
The individual contributions add up to power consumption of 166.4 mW. The power consumption of the active pixels scales with the size of the pixel matrix, while the other contributions don't. The contribution of the readout cells is negligibly small. On the basis of the above values the power consumption of a full size sensor with an active area of $2 \times 2\,\mathrm{cm}^2$ and four LVDS links is estimated to be $P_{\text{full-size}} \approx 904\,\mathrm{mW}$.

5.3.3 Influence of DAC settings on pulse shaping and power consumption

The results presented in this subsection were obtained in the scope of and presented first in a Master thesis [69].
The AmpOut and Hitbus outputs (see section 4.1) are used to study the sensor's analog performance. They are representative of the outputs of the amplifier and the receiver in the readout cell but in both cases the drivers of the test outputs result in additional signal shaping. Therefore, absolute values of the studied pulse shape parameters are of less interest than their relative changes for varying DAC settings.
The signals were analyzed using an oscilloscope and a passive probe. The signal source was a test pulse injection into pixel (0,1). Figure 5.9 shows a screenshot of the oscilloscope with the injection, Hitbus, and AmpOut signals. Note that the baseline of the injection signal is the high level. Its trailing edge is not visible. The following pulse shape parameters are investigated:

- The **amplitude** is the maximum value of the pulse minus the low level s_{low}, which is defined here as the most probable value of the baseline. The amplitude is studied for the AmpOut.

- The **slew rates** are measures for the steepness of the leading and trailing edges. They are defined here as:

$$\text{rise/fall} = 0.8 \cdot \frac{\Delta s}{\Delta t_{\text{rise/fall}}}\,, \tag{5.1}$$

  where Δs is the difference between s_{low} and the analogously defined high level s_{high} and Δt is the time difference between the signal crossing

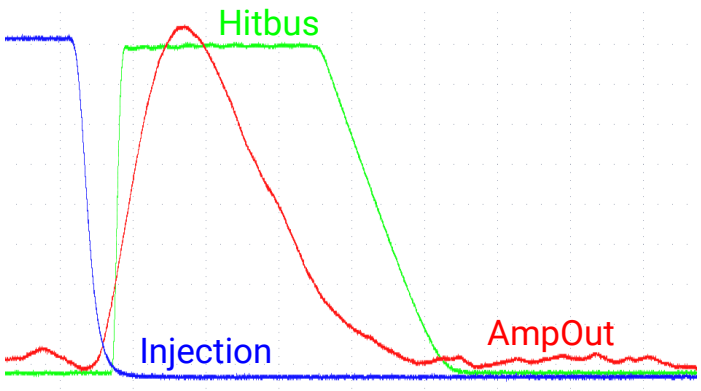

Figure 5.9: Oscilloscope screenshot

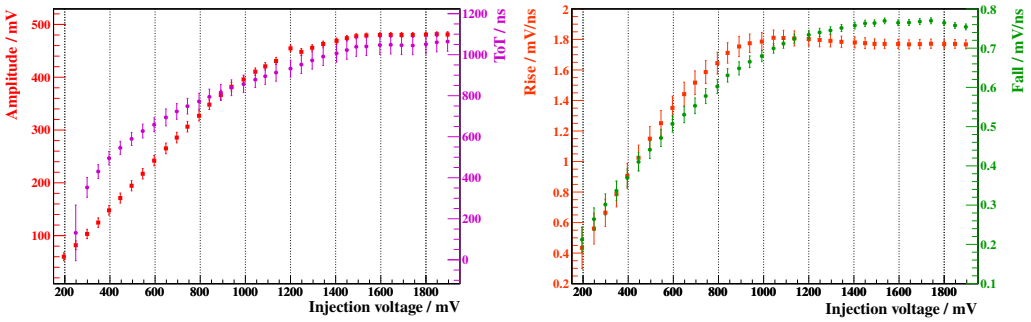

(a) Amplitude and ToT

(b) AmpOut rise and fall

Figure 5.10: Pulse shape parameters vs injection voltage [69]

$(s_{\text{low}} + 0.1 \cdot \Delta s)$ and $(s_{\text{low}} + 0.9 \cdot \Delta s)$. The slew rates are studied for the AmpOut.

- The **ToT** is measured with the Hitbus. It is defined here as the time difference between the leading and the trailing edge crossing $(s_{\text{low}} + \frac{\Delta s}{2})$.
- The signal **delay** is defined here as the time difference between the leading edges of the injection and the Hitbus signal crossing $(s_{\text{low}} + \frac{\Delta s}{2})$.

Figure 5.10 [69] shows the pulse shape parameters plotted against the injection voltage. The same "default" sensor configuration was used as for the determination of the power consumption discussed in the previous section 5.3.2 (see appendix A1).

An injection voltage of 600 mV was chosen for the measurement series presented below. One DAC was scanned at a time while the others were kept

at the default value. Note that some DACs can interfere with each other but the set of all possible DAC combinations is too large to scan.
For all scans, the power consumption of the sensor was monitored in addition to the pulse shape parameters. Note that the plotted power consumption includes a contribution from the AmpOut and Hitbus drivers of ca. 30 mW, which was not taken into account for the calculation of the chip's power consumption in section 5.3.2 because the drivers are switched off during regular operation.

VPPix

VPPix regulates the amplifier current. In general, a high signal amplitude and a fast rise are desired to achieve good detection efficiency and time resolution. Figure 5.11 [69] shows that the amplitude has a plateau for VPPix values between 7 and 20. The rise has its maximum around 20. The power consumtion of the amplifier makes up a large part of the overall power consumption of the chip and it increases linearly with VPPix.

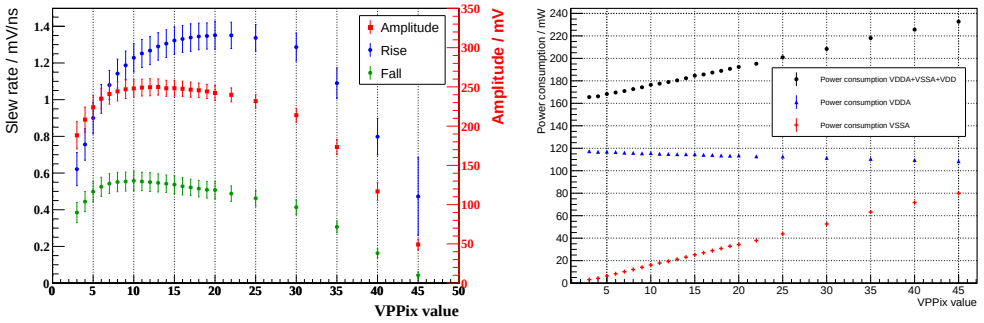

(a) AmpOut amplitude and slew rates (b) Power consumption

Figure 5.11: AmpOut pulse shape parameters and power consumption vs VPPix (default value: 20) [69]

VNFBPix

VNFBPix adjusts the amplifier's resistive feedback, which increases the steepness of the trailing edge and enables a more stable operation. Figure 5.12 [69] shows that the slew rate of the trailing edge increases with higher VNFBPix values, while the amplitude decreases. The DAC has no signicant impact on the power consumption.

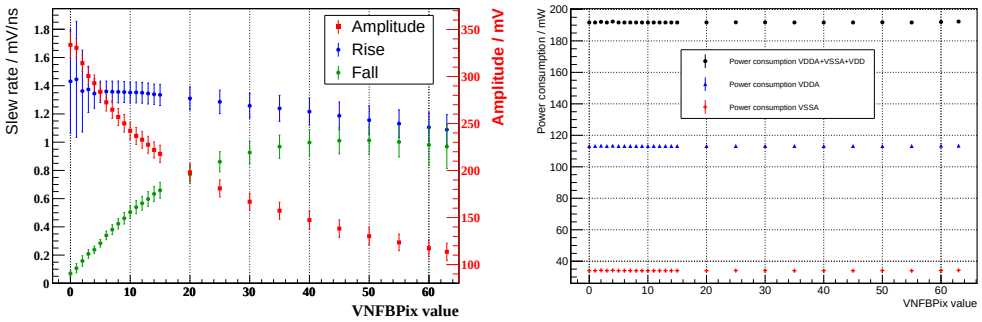

(a) AmpOut amplitude and slew rates (b) Power consumption

Figure 5.12: AmpOut pulse shape parameters and power consumption vs VNFBPix (default value: 10) [69]

VPLoadPix

Varying VPLoadPix changes the resistive load and the feedback capacitance of the amplifier. Figure 5.13 [69] shows that this has a significant effect on the signal amplitude and the slew rates. They all have a maximum at VPLoadPix values of approximately 10. The power consumption increases linearly with VPLoadPix.

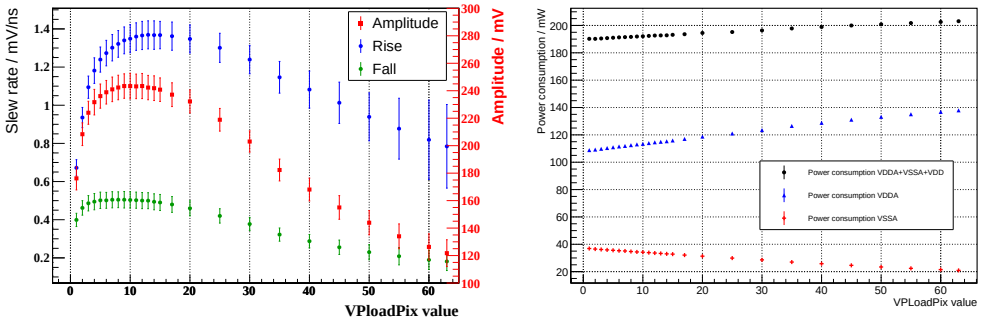

(a) AmpOut amplitude and slew rates (b) Power consumption

Figure 5.13: AmpOut pulse shape parameters and power consumption vs VPLoadPix (default value: 10) [69]

VNFollPix

VNFollPix determines the current of the source follower at the amplifier output (see figure 4.4). The power consumption shows a steep liner rise with

increasing VNFollPix, while above a value of 10 no significant effect on the pulse shape parameters is observed anymore (see figure 5.14 [69]).

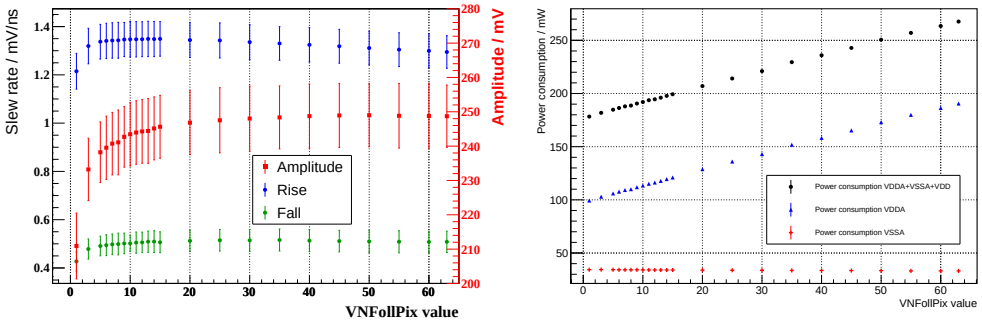

(a) AmpOut amplitude and slew rates (b) Power consumption

Figure 5.14: AmpOut pulse shape parameters and power consumption vs VNFollPix (default value: 10) [69]

BLResPix

The baseline restoration of the comparator circuit is adjusted via BLResPix. The Hitbus output is used to study the effect. Higher BLResPix values result in smaller ToTs, as it is expected because the gate voltage of the comparator's input transistor can be pulled down to the baseline faster. Figure 5.15 [69] shows that the DAC has no significant influence on the delay and the power consumption.

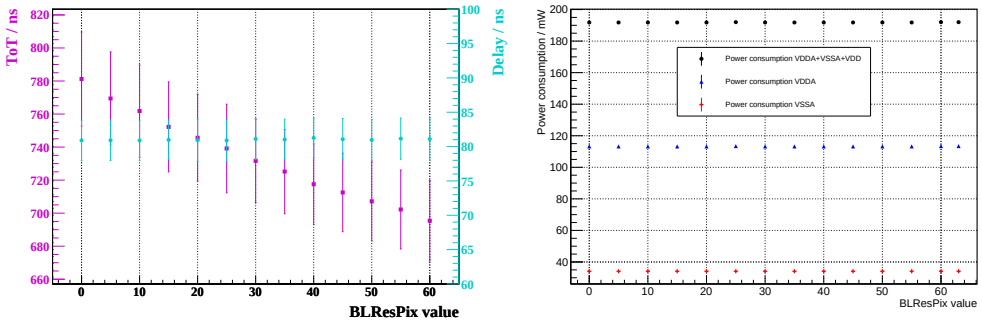

(a) ToT and delay (b) Power consumption

Figure 5.15: Hitbus pulse shape parameters and power consumption vs BLResPix (default value: 10) [69]

VNCompPix

VNCompPix is the DAC that controls the comparator current. Figure 5.16 [69] shows that there is an operation region between VNCompPix values of 5 and ca. 40. The power consumption increases linearly with VNCompPix until it saturates for large DAC values.

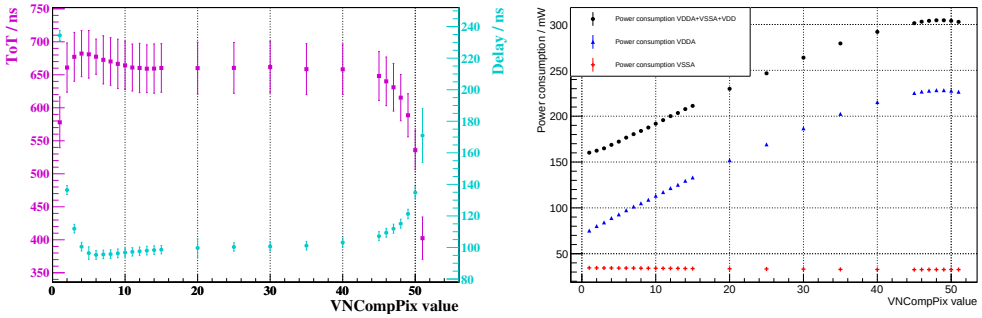

(a) ToT and delay (b) Power consumption

Figure 5.16: Hitbus pulse shape parameters and power consumption vs VNCompPix (default value: 10) [69]

5.3.4 Noise and threshold dispersion

This section mainly focuses on the measurement of the dispersion of noise and the comparator threshold among pixels. Due to process variations in the sensor production, the applied threshold value does effectively not result in the same actual threshold for every pixel. The data that was taken for the according studies also allows for determining a signal to noise ratio (SNR) and a calibration of the comparator threshold to the number of signal charges (electrons). The signal of a mono-energetic source is measured for varying thresholds, which would ideally result in a step function with the position of the step at the threshold that corresponds to the signal size. However, noise smears the edge of the function, which results in an s-curve shape. Figure 5.17a shows the result of a threshold[1] scan performed for pixel (0,1) with ^{55}Fe used as signal source. The function

$$f_{\mathrm{s}}(x) = \frac{a}{2}\left(1 + \mathrm{erf}\left(-\frac{x-\mu}{\sqrt{2}\sigma_{\mathrm{n}}}\right)\right) \tag{5.2}$$

[1]Note that in this section the term threhold is used to denote the absolte threshold voltage that is supplied to the comparator, whereas this value minus the baseline voltage of the comparator is referred to as effective threshold. For all other measurement results presented in this thesis, the term threshold refers to the effective threhold.

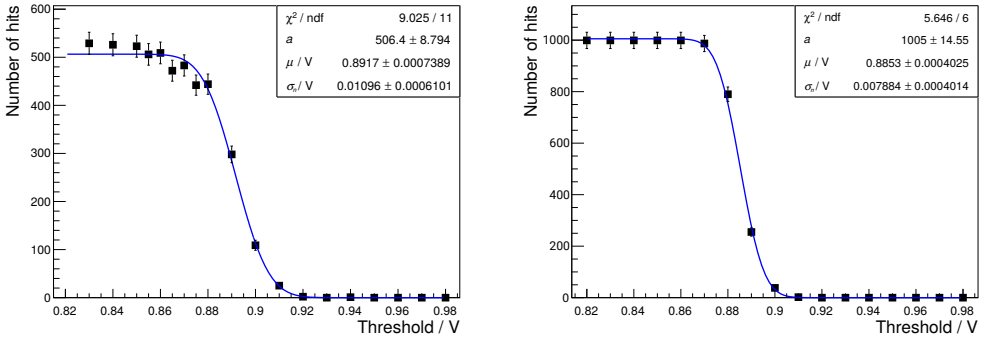

(a) ^{55}Fe X-rays (b) 0.25 V test pulse injection

Figure 5.17: Exemplary results of threshold scans for pixel (0,1) with fitted s-curves; signals were created by X-rays from an ^{55}Fe source (a) and a test pulse injection of 0.25 V (b)

is fitted to the data, where erf denotes the error function

$$\mathrm{erf}(x) = \frac{1}{\sqrt{\pi}} \int_{-x}^{x} \mathrm{e}^{-t^2} \, \mathrm{d}t. \tag{5.3}$$

About 25 % of all ^{55}Fe decays lead to the emission of X-rays with an energy of approximately 5.9 keV. This energy is fully absorbed by the sensor. Therefore, ^{55}Fe can be considered a mono-energetic signal source. In reality, sometimes not all of the resulting signal charges end up in the detection volume of a single pixel. This is one reason why the data does not perfectly fall on the s-curve. An alternative mono-energetic signal source is the test pulse injection. However, it has the disadvantage that results for different pixels are less comparable due to pixel-to-pixel variations in the injection capacitance caused by process variations. Figure 5.17b shows again a threshold scan for pixel (0,1) with an s-curve fit, but here a test pulse injection of 0.25 V was used as signal source.
The measurement with ^{55}Fe was performed simultaneously for all pixels without threshold tuning. The fit parameters μ and σ_n represent the threshold for the ^{55}Fe signal and the pixel's noise level, respectively. Figure 5.18 shows them plotted as pixel maps and histograms. There is a slight trend towards larger μ values at the top of the sensor, which can be related to a slightly non-uniform power distribution. The histograms show normal distributions. The μ distribution has a mean $\overline{\mu}$ of approximately 912.3 mV and an RMS of approximately 14.2 mV. The σ_n distribution has a mean $\overline{\sigma}_\mathrm{n}$ of approximately 10.8 mV and an RMS of approximately 1.3 mV.
Figure 5.19 shows the correlation of μ and σ_n. A high μ value corresponds

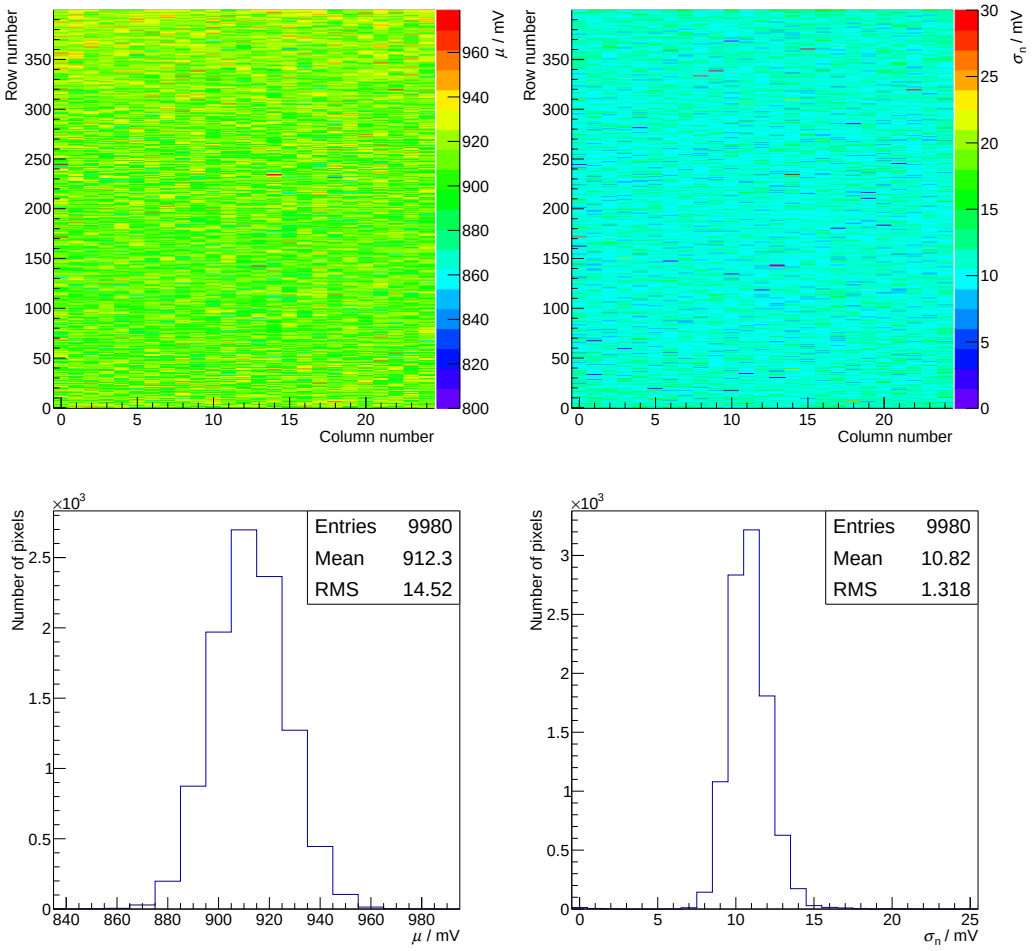

Figure 5.18: Threshold (a) and noise (b) dispersion measured with an ^{55}Fe source plotted as pixel maps and histograms

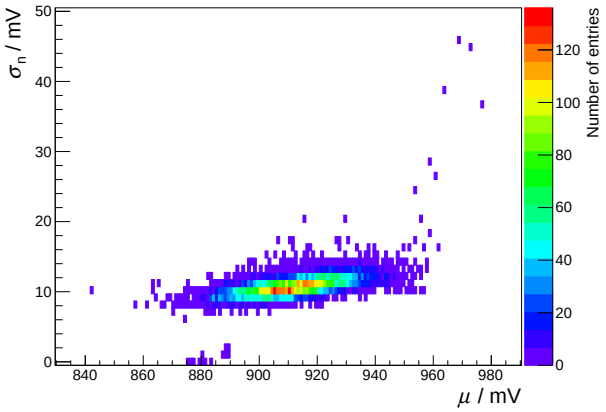

Figure 5.19: Correlation of μ and σ_n

to the applied threshold value resulting effectively in a comparatively low threshold. Generally, the corresponding pixels have a higher probability to detect noise at the applied threshold value.
Dividing the difference of $\overline{\mu}$ and the nominal baseline value (800 mV), i.e. the effective threshold, by $\overline{\sigma}_n$ yields an average SNR for an ^{55}Fe signal of

$$\overline{\mathrm{SNR}} = \frac{\overline{\mu} - \mathrm{baseline}}{\overline{\sigma}_n} \approx 10.4 \pm 1.8 \tag{5.4}$$

The number of electron-hole pairs created in silicon through the absorption of a 5.9 keV photon is about 1640. This means an effective threshold of ca. 912 mV corresponds to a signal of 1640 electrons. Note that this threshold value depends on the DAC settings, especially the VPPix value, which is 20 in this case. Assuming a linear relation between the number of signal electrons and the corresponding threshold, the measured noise level ($\overline{\sigma}_n$) corresponds to approximately 160 electrons.

5.3.5 Efficiency

The probability for detecting a particle traversing the sensor is one of the most important quantities for evaluating the sensor performance. The efficiency is generally defined as the ratio between detected particle hits and the number of particles traversing the sensor. A reference measurement is required to determine the latter. A beam telescope (see section 5.1.3) can be used to reconstruct reference tracks and select the ones that go through the DUT. The efficiency ϵ can then be defined as

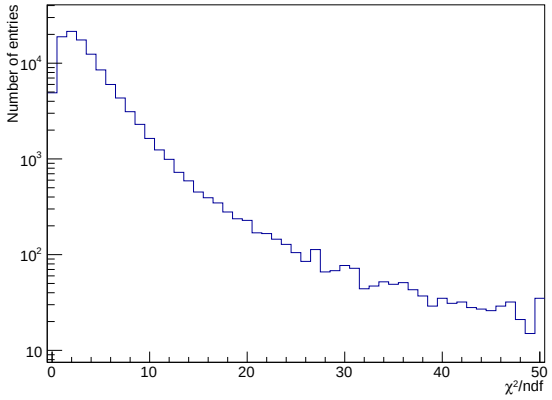

Figure 5.20: Exemplary χ^2 distribution of straight track fits to MuPix8 telescope data

$$\epsilon = \frac{\text{number of tracks with a matching DUT hit}}{\text{number of reference tracks}}. \tag{5.5}$$

The efficiencies presented in this section were measured using the MuPix8 beam telescope described in section 5.1.3. Its spatial resolution is sufficient to resolve the efficiency on a single pixel but not on sub-pixel level. For studies with sub-pixel spatial resolution, see section 5.4. In the following, the analysis procedure for the determination of the efficiency is described before the measurement results are presented.

Analysis procedure

The analysis presented here is based on readout frames that are usually one timestamp cycle (1024 timestamp bins) long to avoid ambiguities. Particle tracks are reconstructed by fitting straight lines to the hits in the three reference layers. The mathematical description of the straight track fit can be found in appendix A2. It is required that there is at least one hit in every reference layer in a frame. A cut on the timestamp differences of the hits in the reference layers is applied before the track is fitted to reject accidental combinations. After the fit, a χ^2-cut is applied for the same reason and, in addition, to reject tracks in which a large amount of scattering occured. Figure 5.20 shows an exemplary distribution of χ^2 divided by the number of degrees of freedom (ndf). Typically, a cut at a value of $\chi^2/\text{ndf} = 20$ is applied.
The relative sensor positions have to be known. Therefore, a software alignment is performed iteratively, where shifts of the sensors (including the DUT)

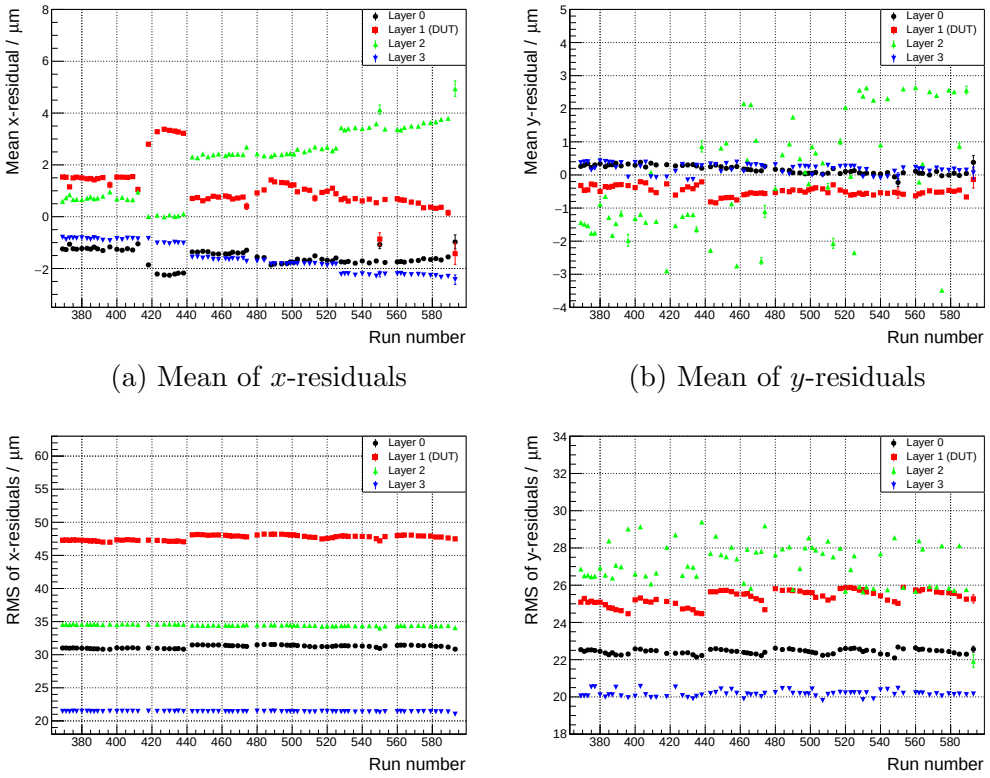

(a) Mean of x-residuals

(b) Mean of y-residuals

(c) RMS of x-residuals

(d) RMS of y-residuals

Figure 5.21: Mean and RMS of residuals in x- and y-direction vs run number

are applied in x- and y-direction (i.e. orthogonal to the beam direction) until the means of the residual[2] distributions for both dimensions equal approximately zero. Figure 5.21 shows the mean and the RMS of the residual distributions of individual measurement runs. One run contains $\mathcal{O}(10^6)$ tracks. Note that here the residuals of the DUT are biased, i.e. the DUT is included in the track fit, which is obviously not the case when fitting the tracks for the efficiency determination. The values of the mean are smaller than 5 µm and the RMS is approximately half the size of the respective pixel dimension or smaller. Note that ATLASPix_Simple and MuPix8 have different pixel sizes[3].

For every reference track, matching DUT hit clusters (see section 5.3.6) are searched for within the corresponding readout frame. At least one pixel of the

[2]One-dimensional distance from the hit position (pixel center) to the fitted track

[3]$130 \times 40\,\mu m^2$ for ATLASPix_Simple and $81 \times 80\,\mu m^2$ for MuPix8 reference layers

cluster has to partially overlap with a spatial matching window around the point of the track's intersection with the DUT plane. The spatial matching window is defined by a circle in the global coordinate system that is extrapolated onto the DUT plane, which, in the case of a rotated DUT, results in an ellipse. Furthermore, the difference of the timestamp of the matching hit and the track timestamp has to be smaller than a certain time interval, referred to as matching time window. The track timestamp is defined as the average of the individual timestamps of the three hits in the reference layers. The sizes of the spatial and the time matching window are given below in the scope of the discussion of the results.
Tracks with a timestamp close to the readout frame edge are disregarded because in such instances the matching DUT hit cluster might have ended up in the adjacent frame.
The efficiency is calculated according to formula 5.5 for each individual pixel. For the calculation of the average efficiency of the whole sensor, a region of interest (ROI) is defined. It excludes the outermost pixel columns and rows to disregard false inefficiencies due to scattering or alignment effects. The determination f the efficiency error is discussed in appendix A3.
Every DUT hit that is not part of a matched cluster is counted as noise. Consequently, the noise rate is typically overestimated by counting real particle hits that have no associated track due to tracking inefficiencies or scattering.
Figure 5.22 shows exemplary pixel maps of the track intersection with the DUT layer (a), the efficiency (b), and the noise rate (c). At the edges of the efficiency map, inefficiencies are visible that stem from a slight rotation of the DUT around the z-axis. Only the pixels inside the indicated ROI are taken into account for the calculation of the sensor's average efficiency. The spots of lower efficiency inside the ROI correspond to masked pixels. They are not excluded for the calculation. The increased noise rates in certain areas above row 300 are discussed in section 5.3.7.

Results

Figure 5.23 shows the average efficiency and noise rate plotted vs the threshold for different HV values and the two different substrate resistivities 80 Ωcm (a) and 200 Ωcm (b). The data was taken at PSI. The polarity of the beam particles was positive and the beam momentum was set to approximately 300 MeV/c. The radius of the spatial matching window is 300 µm. The matching time window is 2×30 MuPix8 timestamp bins, i.e. 480 ns. It is chosen to be fairly wide because the time of arrival before offline corrections (see section 5.3.8) is used to perform the matching. It is shown below that generally no matching of noise hits occurs.

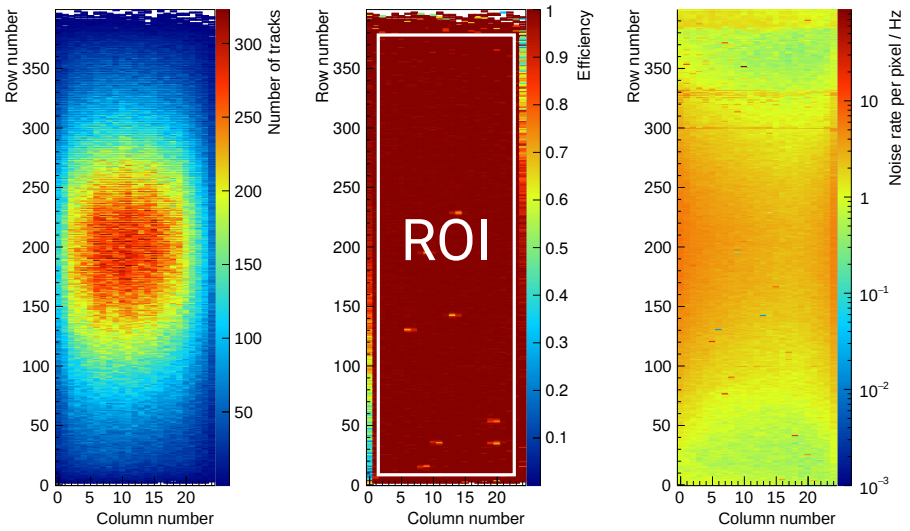

(a) (b) (c)

Figure 5.22: Examplary pixel maps of extrapolated track position (a), efficiency (b), and noise rate(c)

In general, the efficiency is expected to increase with the HV due to an increase of the width of the depletion region W (see section 3.1), which leads to larger signals. Furthermore, a higher efficiency is expected for the higher substrate resistivity, which also leads to a larger W. At the lowest tested thresholds, an average efficiency of above 99 % is reached for all HV values, except for HV = −10 V for the substrate resistivity of 80 Ωcm. The effect of the HV and the substrate resistivity can be observed in the range of thresholds over which a high efficiency is achieved. For the substrate resistivity of 80 Ωcm, the efficiency significantly decreases above thresholds of ca. 100 mV and it decreases faster for lower HV values. For the substrate resistivity of 200 Ωcm, the efficiency is still close to 100 % at a threshold of 200 mV for the maximum HV.

Going down in the threshold value, the average noise rate per pixel stays at approximately 2 Hz for the most part. Only below a threshold of 80 mV it rapidly increases, limiting the minimum threshold at which the chip can be operated sensibly. This behavior is the same for all tested combinations of HV and substrate resistivity. Therefore, especially the sensor with the substrate resistivity of 200 Ωcm has a large operating range of threshold values that result in a high efficiency and a low noise rate.

The error of the noise rate is determined by taking the square root of the av-

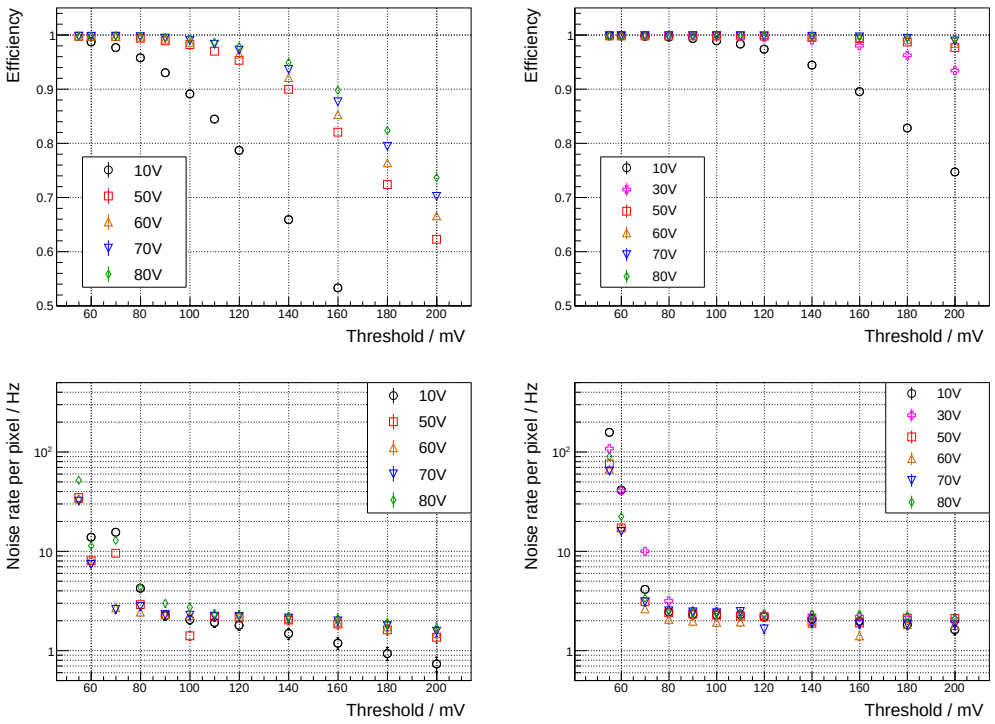

(a) 80 Ωcm (b) 200 Ωcm

Figure 5.23: Average sensor efficiency and noise rate vs threshold for different HV values and substrate resistivities

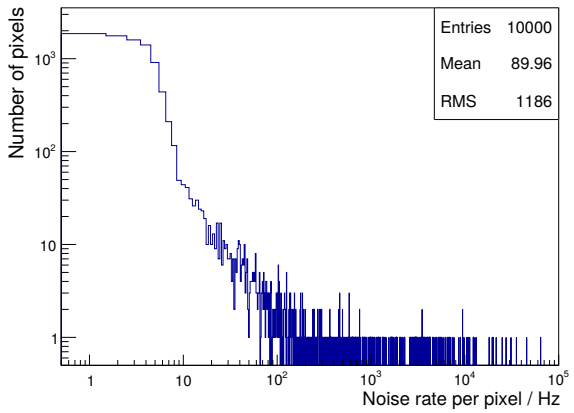

Figure 5.24: Distribution of the noise rates of all pixels for a threshold of 55 mV and HV = −80 V

erage number of unmatched hits and then dividing by the runtime. This does not reflect the fact that the noise is usually dominated by a few hot pixels. Figure 5.24 shows the distribution of all noise hits at a threshold of 55 mV and HV = −80 V. It is discussed in section 5.3.4 that the applied threshold value does effectively not result in the same actual threshold for every pixel. Generally, the hot pixels are those for which the applied threshold results in a comparatively low actual threshold (see figure 5.19). To compensate for this, the possibility of tuning the threshold of every individual pixel is implemented in ATLASPix_Simple. The feature was however not used within the scope of this thesis.

Figure 5.25 shows the average sensor efficiency and noise plotted vs the number of pixels masked in software for a threshold of 55 mV and HV = −80 V. n masked pixels means that hits in the n pixels with the highest noise rates are not allowed to be matched to tracks in the data analysis. This sets the efficiency of these pixels to zero. $\mathcal{O}(1)$ pixels were already switched off on chip during data taking and are not counted here. They add to the total inefficiency also at $n = 0$. A linear relation is expected between the efficiency and n if only the correct hits are matched to tracks. The ROI includes 8085 pixels, i.e. switching off one pixel should decrease the efficiency by $8.085 \cdot 10^{-5}$. The pixel masking is performed on the whole sensor. Assuming that the pixels with the highest noise rates are distributed homogeneously over the sensor, a fraction of $\frac{8085}{10000} = 0.8085$ of the masked pixels is located in the ROI. Correcting the slope of the linear fit accordingly yields $\frac{(-6.627 \pm 0.1) \cdot 10^{-5}}{0.8085} \frac{1}{\text{pixel}} \approx (-8.2 \pm 0.1) \cdot 10^{-5} \frac{1}{\text{pixel}}$. The result is in good agreement with the expected value. The point at 0 masked pixels is excluded from the

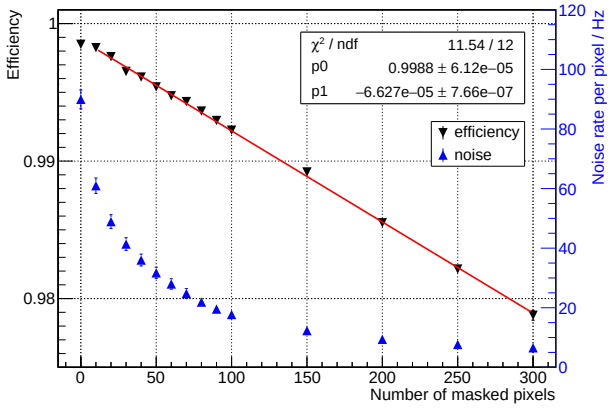

Figure 5.25: Average sensor efficiency and noise rate vs number of masked pixels for a threshold of 55 mV and HV = −80 V with linear fit to the efficiency data

fit because pixels with very high noise rates have increased inefficiencies due to many dead times. Extrapolating the fit function to zero yields an efficiency of approximately 99.95 %. The inefficiency of 0.05 % can be ascribed to the pixels that were masked during data taking.

5.3.6 Hit clusters

Hit cluster distributions can be investigated to study charge sharing effects, i.e. the distribution of signal charges among several pixels. This is relevant, for example, to specify the required bandwith of a detector. A cluster is defined here as a set of adjacent hits within a readout frame. Figure 5.26 shows examples of possible clusters. The types of clusters shown are the only ones that are assumed to occur due to charge sharing for particles traversing the sensor perpendicularly because the drift of the signal charges in the depletion region dominates over lateral diffusion.
Figure 5.27 shows the distribution the of sizes of all clusters matched to a track. The measurement was performed with an ATLASPix_Simple sample with a substrate resistivity of 200 Ωcm, operated with a reverse bias voltage of −60 V. The polarity of the beam at PSI was positive and the beam momentum was ca. 300 MeV/c. The ratios of the number of single hits n_1 and two-hit n_2, three-hit n_3, and four-hit clusters n_4 are $\frac{n_2}{n_1} \approx 0.136$, $\frac{n_3}{n_1} \approx 0.015$, and $\frac{n_4}{n_1} \approx 0.005$. Cluster sizes larger than four can occur, for example, due to particles hitting the sensor under an angle or delta electrons, high energetic ionization electrons that are able to travel a significant distance inside the

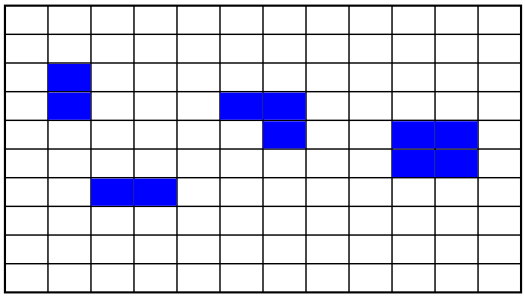

Figure 5.26: Examples of cluster shapes and sizes

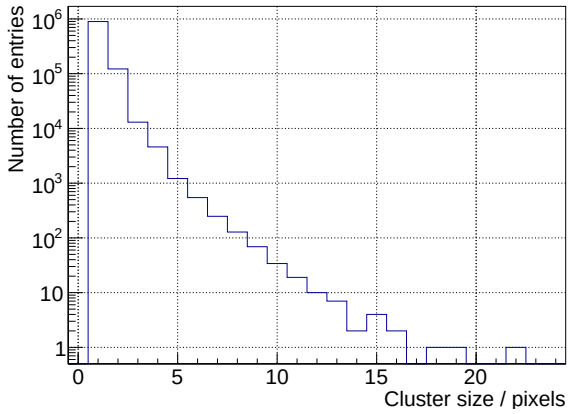

Figure 5.27: Exemplary measured distribution of cluster sizes

sensor while creating further ionization charges.
The asymmetric pixel dimensions of ATLASPix_Simple allow to draw conclusions on the probability of the occurence of two-hit clusters through charge sharing while distinguishing them from crosstalk hits (see next section 5.3.7). Assuming that charge sharing occurs only when a pixel is hit in an area close to the edges with a width w and three-hit and four-hit clusters only for hits in the pixel corners, the ratio of the number of horizontal (extension in x-direction) and vertical (extension in y-direction) two-hit clusters $r_{\mathrm{y,x}}$ is given by the ratio of the areas colored in red and blue in figure 5.28:

$$r_{\mathrm{x/y}} = \frac{n_{2,\mathrm{x}}}{n_{2,\mathrm{y}}} = \frac{40 - 2w}{130 - 2w} \tag{5.6}$$

The difference $n_{2,\mathrm{y}} - n_{2,\mathrm{x}}$ normalized by $n_{2,\mathrm{y}}$ is then given by

$$\frac{n_{2,\mathrm{y}} - n_{2,\mathrm{x}}}{n_{2,\mathrm{y}}} = 1 - r_{\mathrm{x/y}}. \tag{5.7}$$

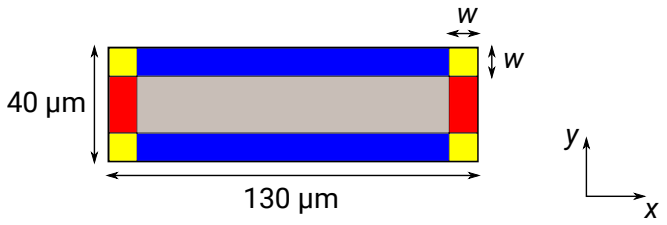

Figure 5.28: Illustration of the areas within a pixel where a hit leads to charge sharing

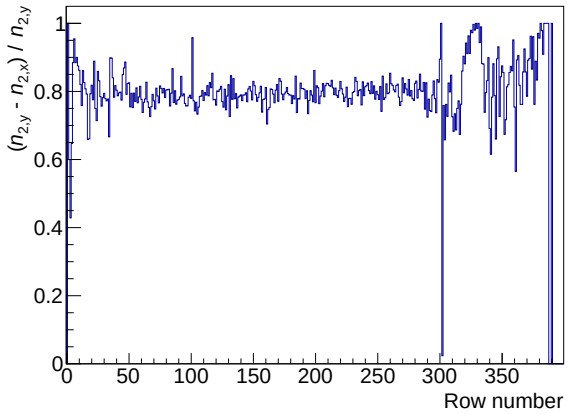

Figure 5.29: $(n_{2,\mathrm{y}} - n_{2,\mathrm{x}})/n_{2,\mathrm{y}}$ vs row number

Figure 5.29 shows a histogram of $\frac{n_{2,\mathrm{y}}-n_{2,\mathrm{x}}}{n_{2,\mathrm{y}}}$ for individual rows. The peak at row 101 and the structures at row 300 and above are discussed in the next section 5.3.7 on line crosstalk. The mean and the RMS of the entries between rows 50 and 280 are used togther with equations 5.6 and 5.7 to calculate w. The peak at row 101 is omitted. This is done for different reverse bias voltages. The results are shown in figure 5.30.
The results can be interpreted in the following way: w decreases with increasing reverse bias voltage because the resulting stonger electric field leads to less lateral diffusion within the charge collection time. This is consistent with results presented in section 5.4.3 on the location of inefficiencies within a pixel at a low reverse bias voltage. The latter occur mostly along the short edge of the pixel. When a pixel is hit in this region, it is likely that the charge is shared between three or four pixels, whereas for most hits close to the long edge, the charge shared among only two pixels.
If, for small reverse bias voltages, the assumption doesn't hold that there is one width w for both dimensions, unsufficient depletion at the short pixel edges could also explain the results. Figure 5.30a shows that for small reverse

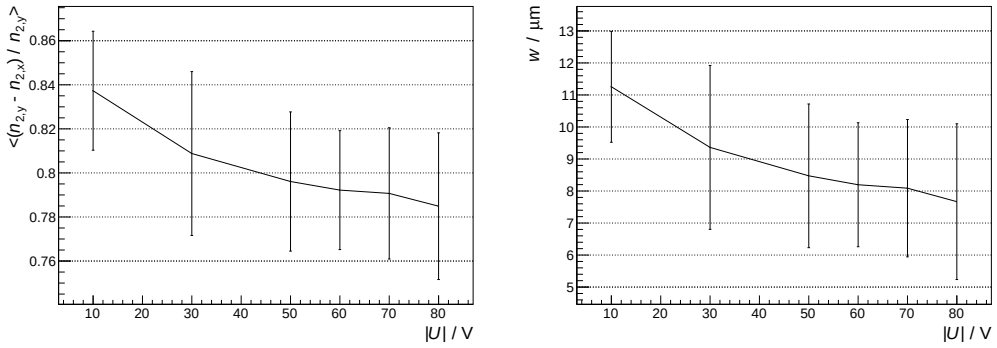

(a) (b)

Figure 5.30: $< (n_{2,\mathrm{y}} - n_{2,\mathrm{x}})/n_{2,\mathrm{y}} >$ (a) and w (b) vs reverse bias voltage

bias voltages there are less horizontal two-hit clusters relative to the amount of vertical two-hit clusters than for large reverse bias voltages. The results were obtained with a threshold of 70 mV, where the sensor is almost fully efficient even at a reverse bias voltage of only -10 V. However, it could be that the signals are small enough so that only the main hit of a potential horizontal double cluster is detected. This would also be consistent with the results presented in section 5.4.3.

5.3.7 Line crosstalk

Each pixel of ATLASPix_Simple has its own direct signal line to the periphery. Consequently, their routing (see figure 4.6) is very dense, which can cause crosstalk between lines. This can in turn lead to fake hits that occupy bandwidth and/or cost computational power for clustering algorithms.
With the routing scheme implemented in ATLASPix_Simple, line crosstalk can either induce two-hit or three-hit clusters along one pixel column as illustrated in figure 5.31. When the pixel marked in blue detects a particle hit, the signal on the corresponding line can induce a crosstalk signal in one or both of the neighboring lines. If the crosstalk signals are large enough, one or both of the readout cells marked in red detect fake hits.
Two-hit clusters can also occur due to charge sharing as discussed in the previous section 5.3.6. The probability for charge sharing is the same for all pixels. The probability for crosstalk on the other hand depends, for example, on the capacitance of two neighboring transmission lines. The capacitance depends in turn on the line length. The length of the transmission lines of ATLASPix_Simple increases with the row number. Therefore, plotting the number of two-hit and three-hit clusters against the row number can be use-

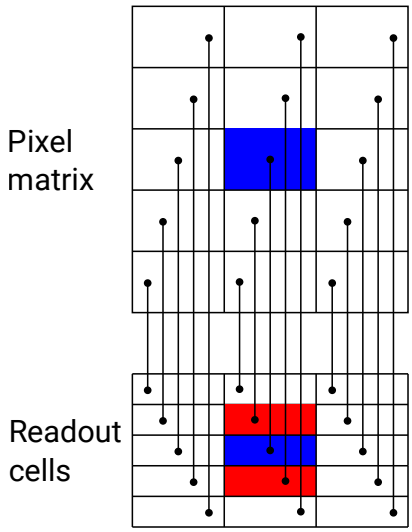

Figure 5.31: Illustration of the pattern of line crosstalk hits

ful to identify crosstalk.
In the case of MuPix8, an HV-MAPS prototype similar to ATLASPix_Simple, crosstalk is in fact very prominent. Figure 5.32 [73] shows the difference between the number of horizontal and vertical two-hit and three-hit clusters normalized by the number of all clusters (including single hits) and plotted against the row number. This equals the probability for crosstalk because MuPix8 has almost the same pixel pitch in both dimensions. Also for MuPix8 the length of the signal lines increases with the row number, hence, the crosstalk probability does so as well. The peaks and gaps in the crosstalk probability correspond to lines with particularly small or large distances between them.
While MuPix8 has its comparators inside the readout cells, ATLASPix_Simple has them implemented inside the active pixels. Consequently, MuPix8 transmits analog signals with varying amplitudes over the signal lines while ATLASPix_Simple transmits already discriminated signals, i.e. signals with a normalized height. The receivers in the readout cells can to an extent be optimized such that the crosstalk signals are not detected as hits. Figure 5.33 shows the same plots as figure 5.32 but for ATLASPix_Simple. Here, the result for two-hit clusters is not exactly equal to the crosstalk probability due to the asymmetric pixel dimensions, as discussed in the previous section 5.3.6.
Up to row 301 the two-hit cluster distribution shows only three peaks at rows 101, 199, and 301. The corresponding lines are the only ones that have only one neighbor at the standard line distance while they have a larger distance

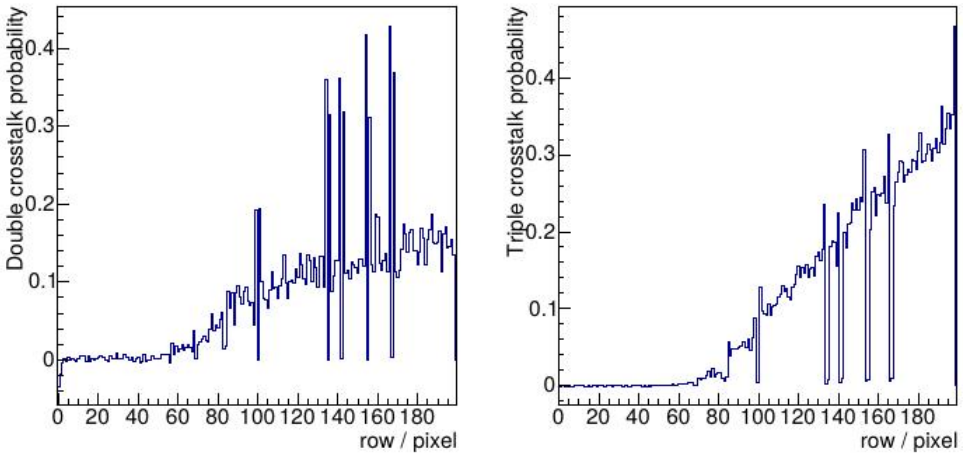

Figure 5.32: Probability for crosstalk-induced two-hit (left) and three-hit (right) clusters vs row number for MuPix8 [73]

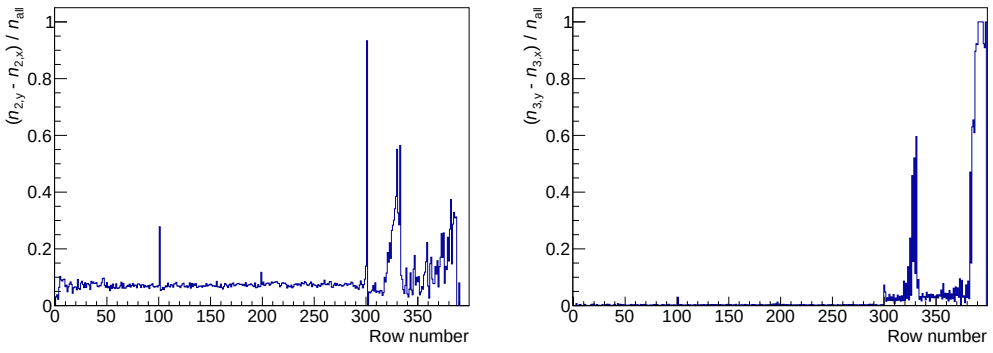

(a) Two-hit clusters

(b) Three-hit clusters

Figure 5.33: $(n_{2,\mathrm{y}} - n_{2,\mathrm{x}})/n_{\mathrm{all}}$ and $(n_{3,\mathrm{y}} - n_{3,\mathrm{x}})/n_{\mathrm{all}}$ vs row number (for ATLASPix_Simple, VMinusPix = 700 mV)

to their second neighbor. Larger crosstalk signals are incuced in the closer neighbor than for all other lines.
There are almost no crosstalk-induced three-hit clusters below row 300. Above row 300 crosstalk occurs with high probability. Around row 330 every hit leads either to a crosstalk-induced two-hit or three-hit cluster. The corresponding lines are the only ones that have metal layers for power and ground above them, which changes the capacitance.
Above row 350 the capacitance between the lines gets large enough to induce some two-hit clusters up to around row 390, where the threshold to always detect the crosstalk signlas in both neighbors is reached.
The amount of crosstalk is sensitive to the voltage VMinusPix, the low level of the driver of the signal line (see section 4.1). The results discussed above were obtained with VMinusPix = 700 mV. Figure 5.34 shows the same plots as shown in figure 5.33 for different VMinusPix values. Note that these measurements were performed at a different testbeam campaign, where the probability to detect crosstalk was overall lower because different sensor supply voltages were used: VDD = 2.0 V (instead of 1.9 V) and VSSA = 1.2 V (instead of 1.0 V). The low level of the amplifier output decreases with increasing VSSA while the high level stays constant. Therefore, a higher VSSA results in pulses with smaller amplitudes at the amplifier output. While the lines to the periphery transmit already discriminated signals with a normalized height, larger pulses at the comparator input still result in a steeper rising edge of the comparator output. Line crosstalk is induced by the high-frequency components of the signal [73], which are more prominent in signals with a steeper rise.
Figure 5.35 shows time-over-threshold (ToT) distributions (see section 5.3.8) measured at the two different testbeam campaigns discussed above with the corresponding supply voltages. A larger ToT corresponds to larger signal amplitudes (at the amplifier output). The peaks around zero correspond to the crosstalk hits.

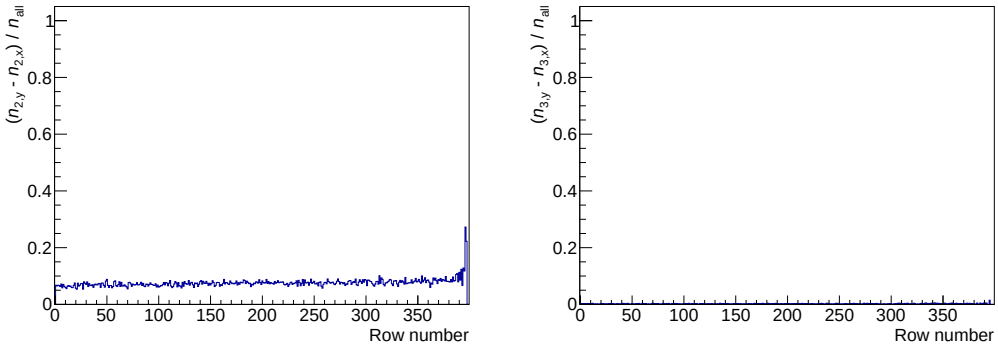

(a) VMinusPix = 800 mV

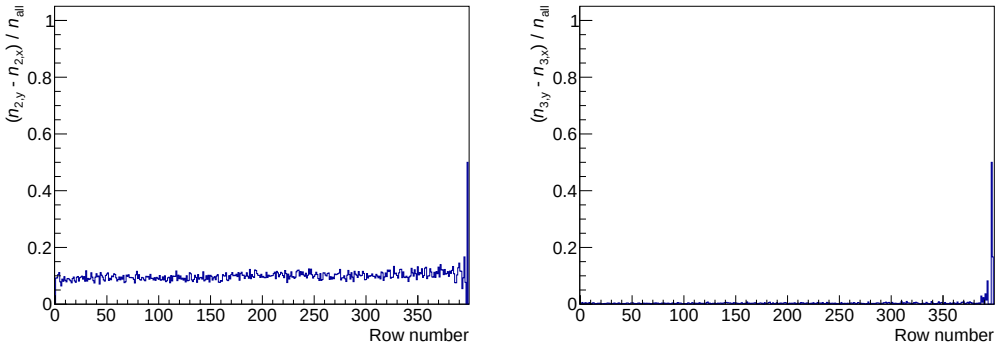

(b) VMinusPix = 700 mV

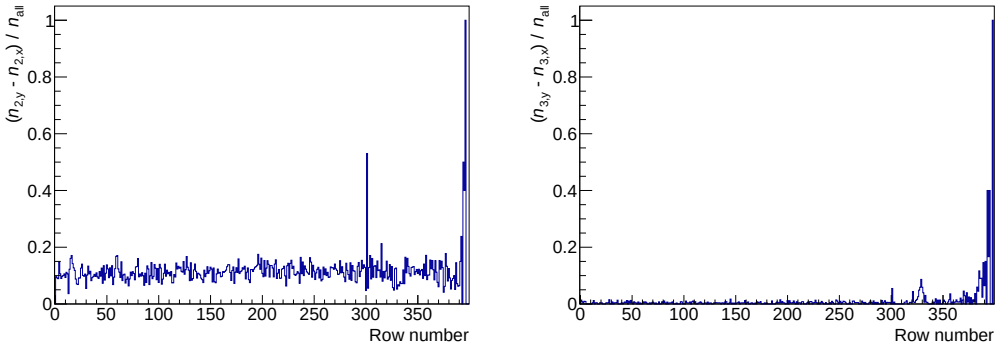

(c) VMinusPix = 650 mV

Figure 5.34: $(n_{2,\mathrm{y}} - n_{2,\mathrm{x}})/n_{\mathrm{all}}$ and $(n_{3,\mathrm{y}} - n_{3,\mathrm{x}})/n_{\mathrm{all}}$ vs row number for VPPix = 40 and different VMinusPix values

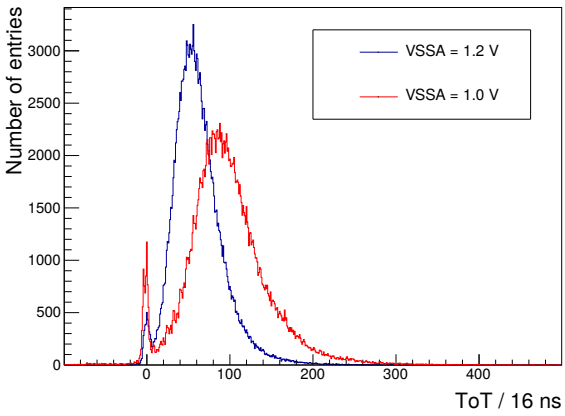

Figure 5.35: ToT distributions measured with VSSA values of 1.0 V and 1.2 V

5.3.8 Time resolution

Time resolution is one of the most critical criteria for the suitability of the HV-MAPS technology for the use in future high pile-up environments. Unambiguous bunch crossing identification and fast trigger decisions are desired to make optimal use of the limited readout bandwidth of detectors. The bunch spacing at the LHC is 25 ns. ATLASPix_Simple measures the time of arrival of each hit (TS1, see section 4.1.4). As an example, 99 % of all timestamps of the hits detected at the time of a bunch crossing lie within a 25 ns window when the standard deviation σ of the corresponding normal distribution equals approximately 4.8 ns.
The time resolution of ATLASPix_Simple is measured with the help of the setup introduced in section 5.1.2. It uses one or more scintillators to measure a reference time t_{ref}.
The time resolution is determined by fitting the probability density function of the normal distribution

$$f(x) = \frac{b}{\sqrt{2\pi\sigma^2}} \, \mathrm{e}^{-\frac{1}{2}(\frac{x-\mu}{\sigma})^2} \tag{5.8}$$

with the mean μ, the standard deviation σ, and a normalization coefficient b to the distribution of $\text{TS1} - t_{\text{ref}}$.
ATLASPix_Simple has the following unintended design feature. $\text{TS1} - t_{\text{ref}}$ depends significantly on the position of the hit cluster on the sensor. The effect is shown in figure 5.36a, where the mean of the $\text{TS1} - t_{\text{ref}}$ distribution of a set of five consecutive pixel rows is plotted against the mean row number. It is an effect of the varying capacitance of the signal lines from the pixels to the periphery due to their different lengths that increase with the row number.
All time resolutions presented in the following are corrected offline for this shift of $\text{TS1} - t_{\text{ref}}$. The plot shown in figure 5.36a is done for every measurement and the correction is performed by fitting a polynomial function of third order to the data. The according function value is substracted from every $\text{TS1} - t_{\text{ref}}$ value. Figure 5.36b shows the same plot after the correction. Figure 5.37 shows the $\text{TS1} - t_{\text{ref}}$ distribution of the whole sensor before and after the correction. $\text{TS1} - t_{\text{ref}}$ is calculated for every hit cluster that is matched to a telescope track and every scintillator hit inside the same readout frame. The smallest TS1 of a hit cluster is used. A fit of the function defined in equation 5.8 yields the time resolution, defined as $1\,\sigma$ of the normal distribution. In this example, it is approximately 6.9 ns after the correction. The measurement was performed using a DUT with a substrate resistivity of 200 Ωcm. The HV was −60 V, and the threshold value was 50 mV.

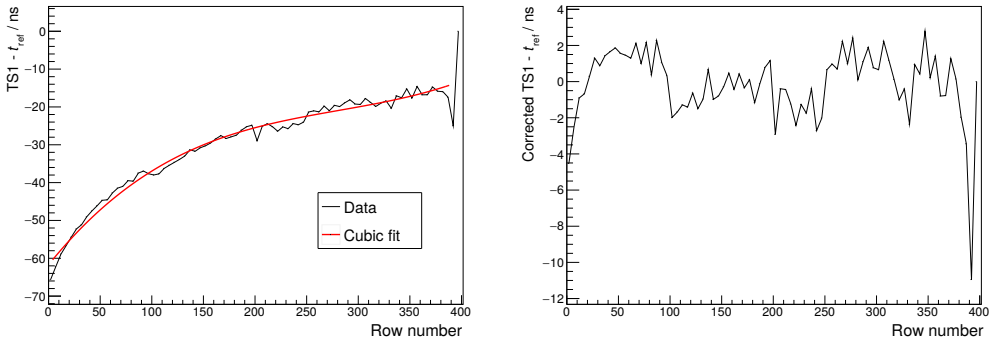

(a) Before correction (b) After correction

Figure 5.36: Example of mean of TS1 $- t_{\text{ref}}$ distribution vs row number before correction with fitted third-order polynomial function (a) and after correction (b)

In general, larger signals are expected to have a steeper rise and therefore lead to an earlier crossing of the threshold. This effect is referred to as timewalk. It is illustrated in figure 5.38, which shows two signal pulses with different amplitudes. The amount of energy that a charged particle deposits in a sensor - and consequently also the signal amplitude - follows the Laundau probability distribution, which is reflected in the ToT distributions shown in figure 5.35. Varying signal amplitudes in combination with timewalk deteriorate the time resolution. A large mean signal size and a low threshold help to minimize the effect. Figure 5.39 shows the time resolution for different substrate resistivities and HV valus plotted against the threshold. The data that these plots are based on is the same that was used to obtain the results on efficiency and noise shown in figure 5.23. The matching of DUT hits to tracks is performed with the same sizes of matching windows. A better time resolution is achieved for lower thresholds, higher substrate resistivity, and higher HV. The best result is $\sigma = (6.82 \pm 0.04)\,\text{ns}$.

Figure 5.40 shows the influence of the DAC settings on time resolution. One DAC was varied at a time. The values that the DACs were set to when another DAC was scanned are given in the caption. Note that all measurements were performed using a sensor with a substrate resistivity of 200 Ωcm and a threshold value of 70 mV except for the VNCompPix scan, which was performed using a sensor with a substrate resistivity of 80 Ωcm and a higher threshold value of 100 mV. The functions of the DACs are explained in section 5.3.3. VNFBPix and BLResPix affect only the falling edge of the signal pulse and have no effect on the time resolution, as expected. VPPix, VN-

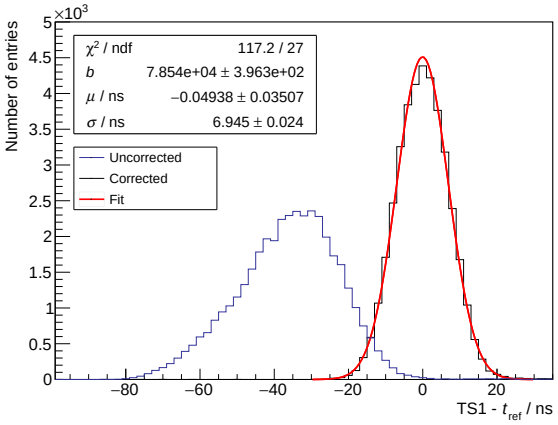

Figure 5.37: Examplary distributions of TS1 $-$ t_{ref} before and after offline correction of row dependence

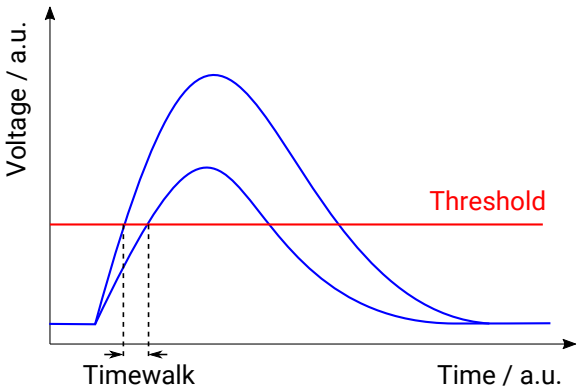

Figure 5.38: Illustration of timewalk

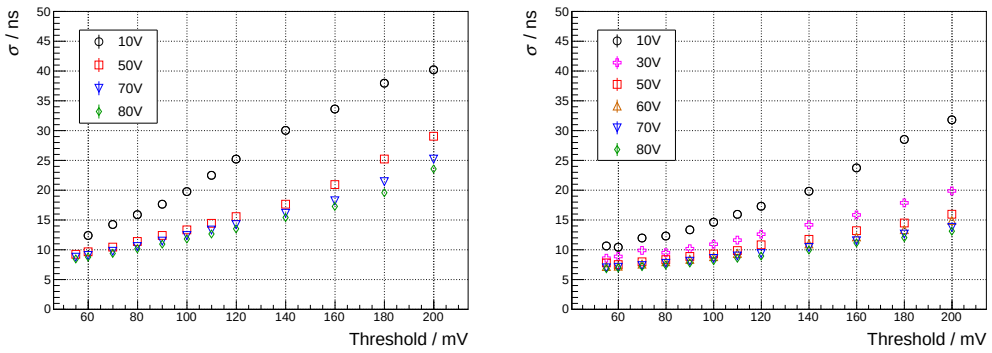

(a) 80 Ωcm (b) 200 Ωcm

Figure 5.39: Time resolution vs threshold for different HV values and substrate resistivities

FollPix, VPLoadPix and VNCompPix all have a large range of values for which the time resolution is at its optimum.
The results presented in figure 5.39 are based on measurements performed at the same testbeam campaign. Here, the default DAC settings given in appendix A1 were used (VPPix = 20, VNFBPix = 10, VNFollPix = 10, VPLoadPix = 10, BLResPix = 10, VNCompPix = 10).

A significant impact of the voltage level VMinusPix on the time resolution of ALTASPix_Simple is observed. VMinusPix is the low level of the driver for the signal line from the pixel to the readout cell (see figure 5.41 (modified from [69]) and section 4.1.1). Figure 5.42a shows σ plotted against the threshold for different VMinusPix values. The data was taken at a testbeam campaign at DESY. The beam energy was set to approximately 3 GeV. The supply voltages VDD and VSSA were increased - compared to their nominal values - to 2.0 V and 1.2 V, respectively. The matching time window is increased by a factor of two compared to the previous analyses because the time resolution is significantly worse for higher VMinusPix values. The results shown above in figures 5.39 and 5.40 were obtained with VMinusPix = 0.7 V.

In general, σ improves with lower VMinusPix values, while noise (see figure 5.42b) and line crosstalk (see section 5.3.7) increase. For VMinusPix values below 0.65 V, the noise saturates the DAQ system at low thresholds. At very low threshold values of ca. 45 mV noise deteriorates the time resolution independent of VMinusPix. The better time resolution for a high threshold and VMinusPix = 0.9 V can be explained by discrimination of small signals with a large TS1 $- t_{\text{ref}}$ either by the threshold or by the matching time window.

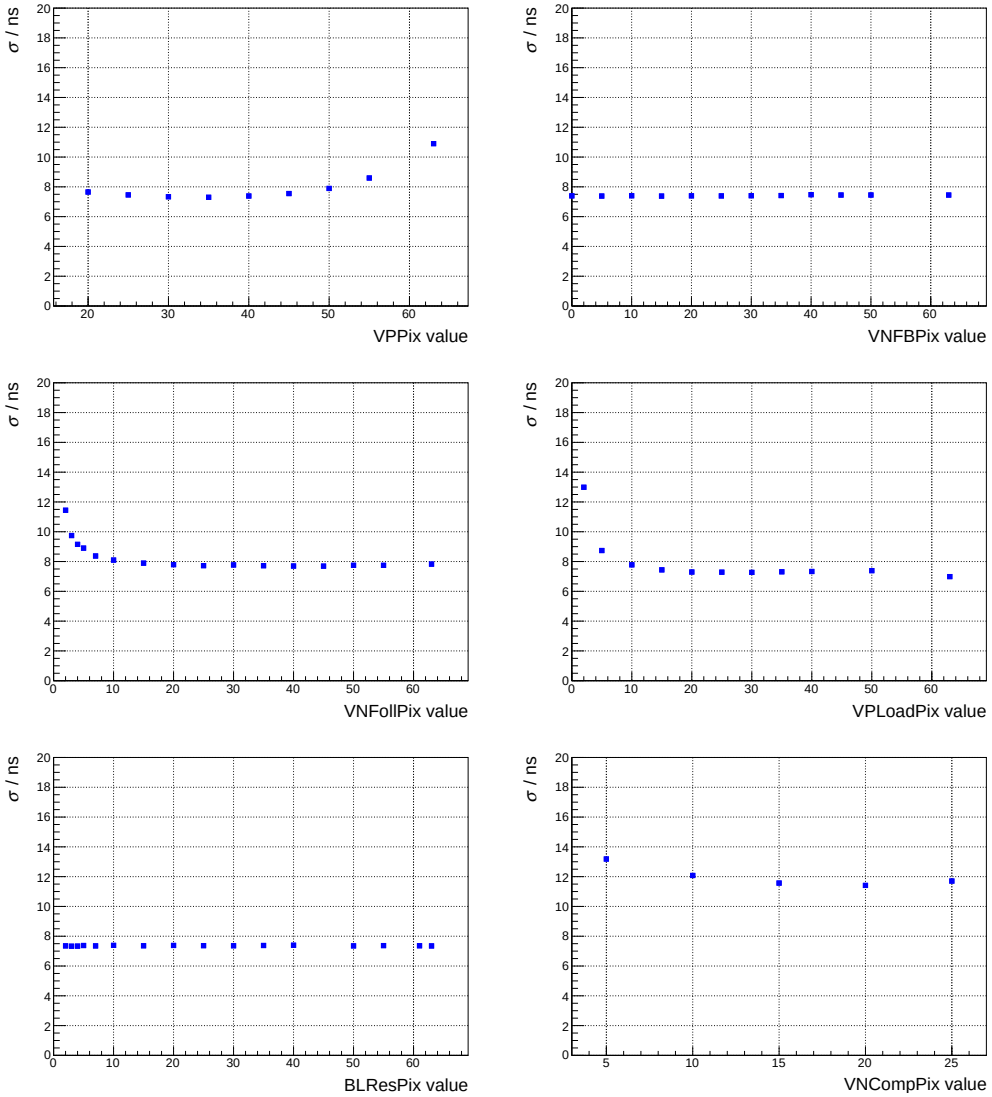

Figure 5.40: Time resolution vs DAC value for VPPix (40), VNFBPix (5), VNFollPix (20), VPLoadPix (10), BLResPix (5), and VNCompPix (10); values in brackets correspond to the settings that the DAC was set to when another DAC was scanned

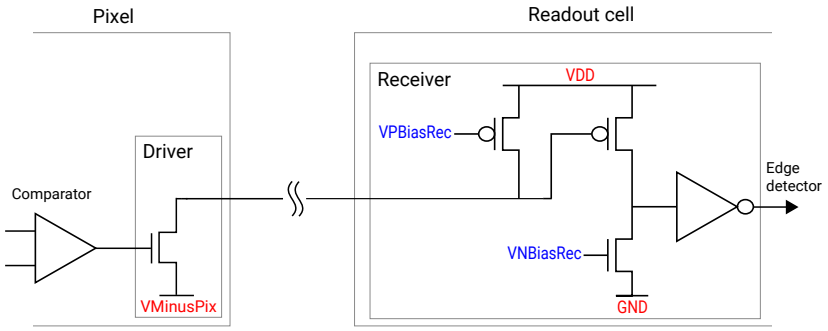

Figure 5.41: Schematic of the driver for the signal line from the pixel to the periphery and the receiver in the readout cell; modified from [69]

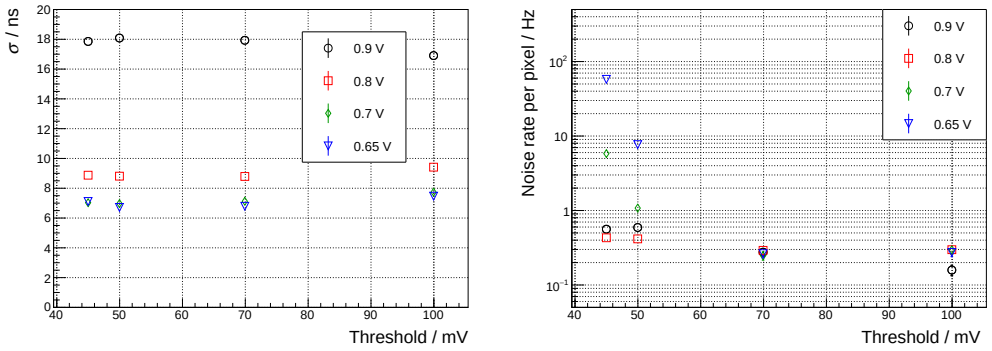

(a) Time resolution (b) Noise

Figure 5.42: Time resolution (a) and noise (b) vs threshold for different VMinusPix values

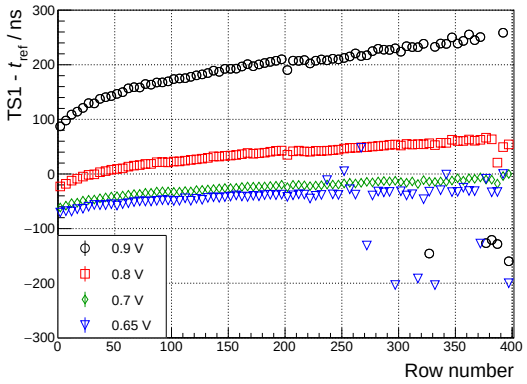

Figure 5.43: Mean of TS1 $-$ t_{ref} distribution vs row number for different VMinusPix values

The effect of VMinusPix on the time resolution is connected to the dependence of TS1$-t_{\text{ref}}$ on the hit position on the sensor, which is more pronounced for large VMinusPix values. This can be seen in figure 5.43, in which the mean of the TS1 $-$ t_{ref} distribution is plotted against the row number for different VMinusPix values.

Timewalk correction

The results presented in this subsection were obtained in the scope of and presented first in a Master thesis [69].
The timewalk correction method discussed in the following makes use of the second timestamp of ATLASPix_Simple, TS2, which is sampled upon the crossing of the comparator threshold by the trailing edge of a signal pulse. An unintended design feature of ATLASPix_Simple is that, at full readout speed, hits are partially read out before TS2 is sampled. This can be avoided by slowing down the on-chip state machine. The chip allows for introducing extra clock cycles and waiting states for this purpose by setting according configuration bits. However, measurements on testbeam campaigns were usually carried out at full readout speed. Therefore, dedicated laboratory measurements were performed to study timewalk correction, which are discussed in this subsection.
^{90}Sr was used as signal source, which does not allow for the use of a reference telescope since the electrons are not collimated and their energy is too low for them to penetrate several consecutive sensor layers without a large amount of scattering. The measurement setup consists of the DUT and one scintillator. Since there is no track information available, the correlations

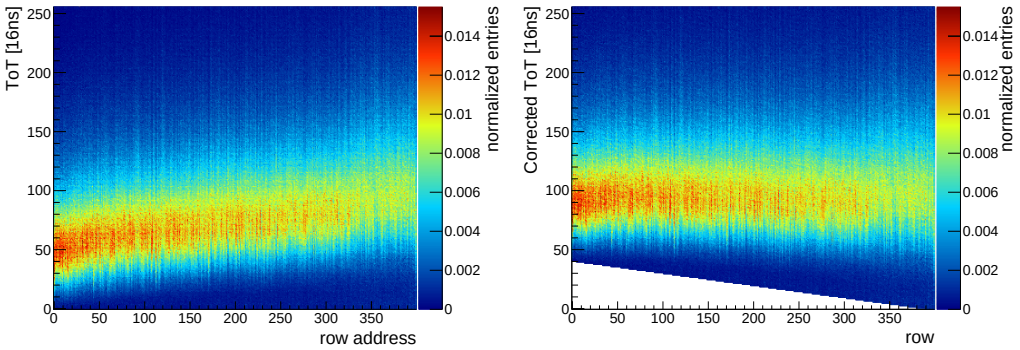

(a) Before correction for row dependence

(b) After correction for row dependence

Figure 5.44: ToT spectra vs row number before (a) and after (b) correction for row dependence [69]

of all DUT hits with all scintillator hits within one readout frame are taken into account. The result is a triangular-shaped background in the TS1 $- t_{\text{ref}}$ distribution. It is accounted for by the modified fit function:

$$f_{\text{bg}}(x) = f(x) + c(d - |x|) \tag{5.9}$$

The function $f(x)$ is defined in equation 5.8 as the probability density function of the normal distribution, c is a scaling parameter and d is the maximum difference between TS1 and t_{ref}.
As discussed above, timewalk (see figure 5.38) is a key limiting factor for a good time resolution. Therefore, ATLASPix_Simple is able to measure the ToT, wich can be used to correct the measured time resolution offline for timewalk. The ToT is the difference of the two timestamps TS1 and TS2 (see section 4.1.4).
Before the ToT is used to correct for timewalk, an offline correction is performed on the ToT itself. There is a drift of the ToT along the row number towards larger values, which can be seen in figure 5.44a [69]. To correct for this effect, the ToT spectrum of each row is shifted by its maximum value. Figure 5.44b [69] shows the ToT spectra of every row after the correction.
ToT spectra of the full sensor are shown in figure 5.35. They resemble the shape of the Landau probability distribution, as expected.
Timewalk can be visualized by plotting the ToT against TS1 $- t_{\text{ref}}$. Smaller signals have a larger timewalk and at the same time they have a smaller ToT, resulting in the typical shape of the correlation plot in figure 5.45a [69]. The data plotted here was taken with a large threshold value of 150 mV

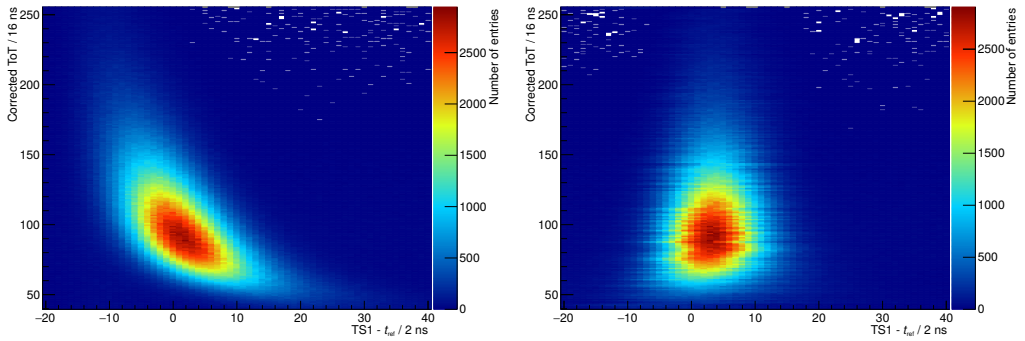

(a) Before timewalk correction (b) After timewalk correction

Figure 5.45: 2D-histogram of ToT vs TS1 $- t_{\text{ref}}$ before (a) and after (b) timewalk correction [69]

to increase the effect for illustration. The timwalk correction is realized by shifting the TS1 $- t_{\text{ref}}$ distributions for individual ToT bins by the value of the TS1 $- t_{\text{ref}}$ bin with the maximum number of entries. Figure 5.45b [69] shows the plot for the corrected TS1 $- t_{\text{ref}}$ values.

Figure 5.46 [69] shows the time resolution plotted against the threshold with and without timewalk correction. The improvement in time resolution due to the correction is of the order of several ns for high thresholds but it is not significant for the lowest usable thresholds with approximately 0.3 ns. This is expected since timewalk increases with the threshold.

The laboratory measurement setup was also used to collect data samples with large statistics, which allows for investigating the time resolution of single pixels. A threshold value of 80 mV and an HV of -80 V were used. Figure 5.47 [69] shows the time resolutions of all individual pixels plotted as pixel maps and histograms with and without timewalk correction. Several effects can be observed. First, the ^{90}Sr source was placed centrally above the sensor at a small distance. As a result, pixels in the center of the chip are hit by the β-electrons perpendicularly while at the top and at the botton of the sensor pixels are hit under an angle, leading to an increased amount of charge sharing. Consequently, the signals are on average smaller in these regions, which deteriorates the time resolution (see figure 5.47c [69]). Note that the ratio of the sensor edges is not drawn to scale in the pixel maps. The pixel matrix is 3.25 mm times 16 mm in size. The effect is much more pronounced along the longer edge. The effect results in the second peak at around 10 ns in the uncorrected time resolution histogram (figure 5.47a [69]) and it is compensated by the timewalk correction (see figure 5.47d). The structure of larger σ for

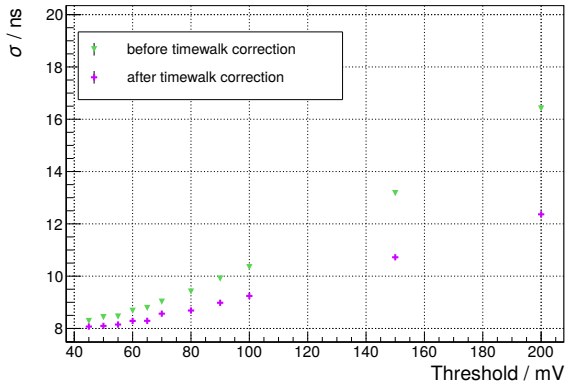

Figure 5.46: Time resolution vs threshold with (a) and without (b) timewalk correction [69]

row numbers above 350 that still remains after timewalk correction is most probably due to line crosstalk (see section 5.3.7). The corresponding signals have a small ToT and at the same time a fast rise [73]. Therefore, timewalk correction does not treat them properly.
The timewalk correction yields an average time resolution of approximately 5.9 ns, a most probable value of approximately 5.8 ns, and an RMS of approximately 0.3 ns.

All time resolution results presented in this section include the timestamp binning contribution of ATLASPix_Simple, $\frac{16\,\text{ns}}{\sqrt{12}}$. A faster timestamp counter could be implemented in the next sensor iteration. It has already been demonstrated with MuPix8 that a timestamp bin size of 8 ns is feasible. With this bin size a time resolution of, for example, $\sigma = 6.8\,\text{ns}$ should improve to

$$\sqrt{(6.8\,\text{ns})^2 - \frac{(16\,\text{ns})^2}{12} + \frac{(8\,\text{ns})^2}{12}} \approx 5.5\,\text{ns}. \tag{5.10}$$

5.4 Studies with sub-pixel resolution

To resolve spatial structures in the sensor performance (e.g. efficiency, time resolution, and cluster distributions) within a pixel (i.e. on a "sub-pixel" level), a beam telescope with a high pointing resolution is required. The Mupix telescope is not suited for this purpose due to the comparatively large pixel size of MuPix8 ($81 \times 80\,\mu\text{m}^2$). Instead, the EUDET-type beam telescope DURANTA was used, which is provided by the DESY testbeam facility to

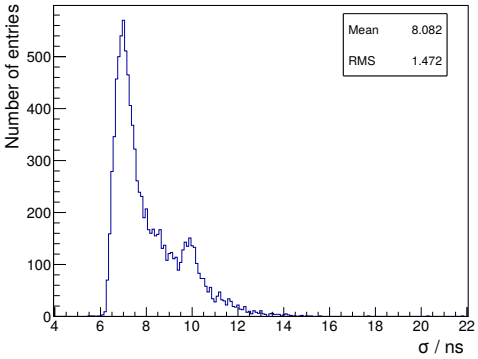

(a) Pixel time resolution histogram without timewalk correction

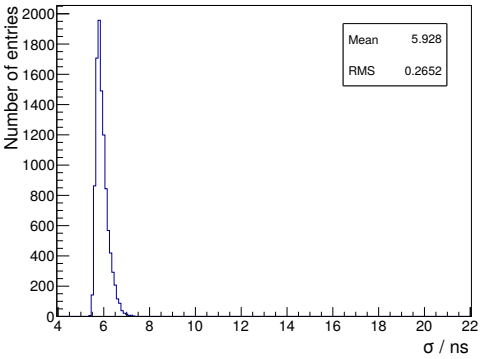

(b) Pixel time resolution histogram with timewalk correction

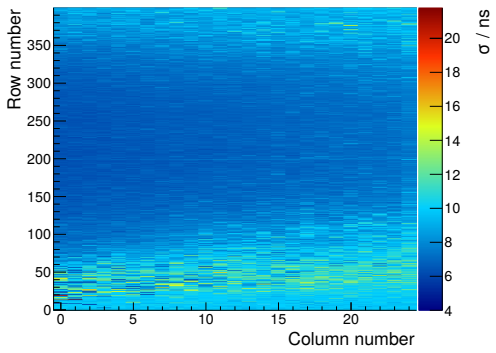

(c) Pixel map of time resolution without timewalk correction

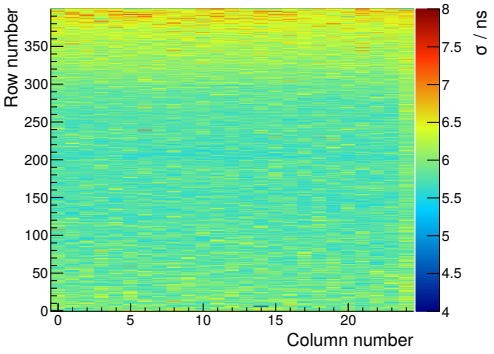

(d) Pixel map of time resolution with timewalk correction

Figure 5.47: Pixel maps and histograms of the time resolution of all individual pixels with and without timewalk correction [69]

users.
In the following sections, the DURANTA beam telescope and the according DAQ system, including ATLASPix_Simple as DUT, are discussed, the pointing resolution of the telescope is investigated, and measurement results are presented.

5.4.1 Description of DURANTA telescope setup and DAQ

The EUDET-type beam telescope called DURANTA [77] is permanently installed at the DESY testbeam facility. It features six layers of MIMOSA-26 pixel sensors and it is integrated into the generic EUDAQ DAQ framework, which allows for the integration of any DUT. The MIMOSA-26 sensors are MAPS (see section 3.5.2) featuring on-chip hit digitization and zero-suppression [79]. They have 1152×576 pixels with a pitch of 18.4 µm in both dimensions, resulting in an active area of approximately $2 \times 1\,\mathrm{cm}^2$. The sensor is read out in a rolling shutter mode: Continuously, the whole pixel matrix is read out row by row. One readout cycle takes 112 µs.
Four scintillators, two placed upstream and two placed downstream of the telescope layers, are read out via photomultiplier tubes (PMTs) and their signals are sent to a trigger logic unit (TLU). Upon coincident signals from all four scintillators, the TLU sends a trigger to all hardware components and optionally an ID that can be used for event building. Only after all hardware components have processed their data of the according event, a new trigger signal can be received by the TLU.
The ATLASPix_Simple DUT is operated with the setup introduced in section 5.1.1. A modified version of the DAQ software interfaces the EUDAQ framework and forwards run start and stop signals and hit data that is buffered on the ATLASPix side until the arrival of a TLU-ID, upon which it is added to the EUDAQ data stream.
The EUDAQ framework does not provide a precise time information. To be able to perform timing studies, the scintillator signals used as TLU triggers are also transmitted to the ATLASPix DAQ system to perform a reference time measurement in the way discussed in section 5.1.2. The timing data is added to the EUDAQ data stream together with the ATLASPix data.
More details on the integration of MuPix-like sensors into the EUDAQ framework can be found in [73].

5.4.2 Software alignment, track fit, and pointing resolution

The DUT was placed between the central two telescope layers with a distance of ca. 10 cm to each of them. The distance between two telescope layers was also ca. 10 cm.
To achieve the pointing resolution required for studies of sub-pixel effects, a more evolved software alignment procedure than for the MuPix telescope is used for the MIMOSA-26 layers. It uses a general broken lines (GBL) fit and it is based on the alignment software for the Mu3e detector [80], which is in turn based on Millepede-II [81].
The alignment of the DUT and the data analysis are performed using a different track fit. Here, the upstream parts and the downstream parts of the tracks are fitted saperately using straight lines (see appendix A2) to take into account scattering in the DUT. The track position is defined as the midpoint of the two intersection points of an upstream and a downstream track with the DUT plane. A cut on the distance between the two intersection points of the order of $\mathcal{O}(10\,\mu\text{m})$ is used to select good tracks. The distribution of this distance is plotted in figure 5.48. The residuals of the DUT are calculated using the pixel center of the matched hit that is clostest to the track. Figure 5.49 shows the four combinations of x- and y-residuals plotted against row and column number after the software alignment. Shifts of the DUT in x- and y-direction as well as rotations around all three axes were performed iteratively until all offsets and slopes were minimal. The highest 20 rows were disregarded due to insufficient statistics in this region. The most significant misalignment that could not be be compensated is a shift of the x-residual of about 2 µm over the full length of the pixel matrix (1.6 mm). It has an impact on the pointing resolution but compared to the pixel pitch in x-direction of 130 µm it is small enough so that sub-pixel structures can be resolved.
Figure 5.50 shows the distribution of the difference of the track position in the DUT plane and the pixel center of the matched hit. Only single hits and no clusters were taken into account because the latter would result in discrete effects at the pixel edges. Ideally, the plot would show a rectangle with the dimensions equal to those of one pixel. Due to a finite pointing resolution, the rectangle is smeared. Figure 5.51 shows the according projections onto the x- and the y-axis. The function

$$f_{\text{box}}(x) = \frac{a}{2}\Big(1 + \text{erf}\Big(-\frac{|x+c| - \mu}{\sqrt{2}\sigma_{\text{p}}}\Big)\Big)\,, \tag{5.11}$$

which is similar to the s-curve defined in equation 5.2, is fitted to both distributions. The result for σ_{p} gives the pointing resolution in the according

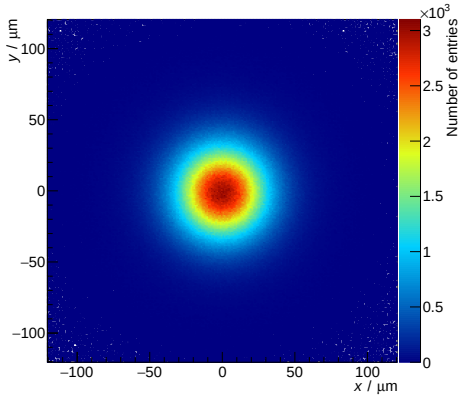

Figure 5.48: Distribution of the difference of the two intersection points of the upstream and the downstream track fits with the DUT plane

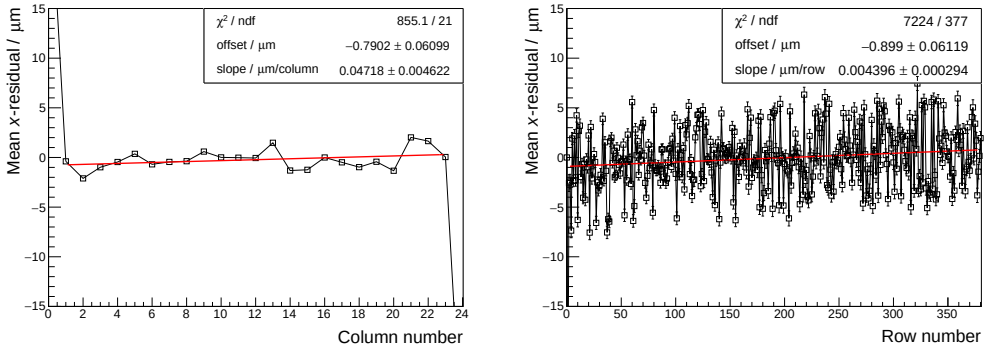

(a) x-residual vs column number

(b) x-residual vs row number

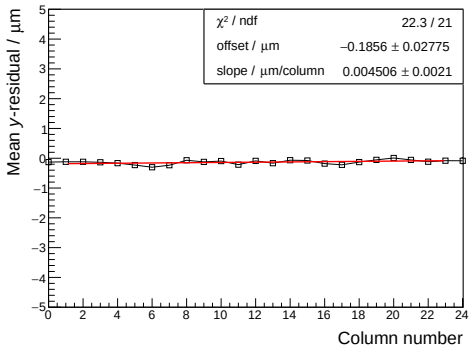

(c) y-residual vs column number

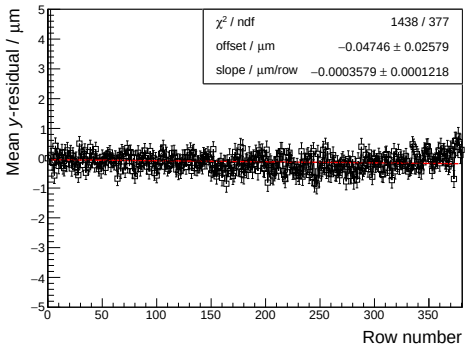

(d) y-residual vs row number

Figure 5.49: Means of x- and y-residual distributions of DUT plotted against row and column number with linear fits

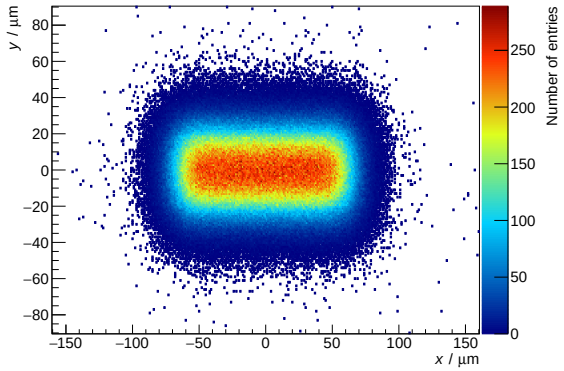

Figure 5.50: Difference between the track position on the DUT and the pixel center of matched single hit

dimension. In x, i.e. along the larger edge of the pixel, it is $\sigma_{\mathrm{p,x}} \approx (10.3 \pm 0.1)\,\mu\mathrm{m}$ and in y, along the short edge of the pixel, it is $\sigma_{\mathrm{p,y}} \approx (10.9 \pm 0.1)\,\mu\mathrm{m}$. The fit parameter μ corresponds to half the pixel pitch. The results are $\mu_{\mathrm{x}} = (64.08 \pm 0.04)\,\mu\mathrm{m}$ and $\mu_{\mathrm{y}} = (18.96 \pm 0.05)\,\mu\mathrm{m}$. They are systematically to small because clusters, which occur for roughly 10 % of all hits and mainly at the pixel edges, were not taken into account. For the same reason, it is possible that σ_{p} is overestimated. This is discussed further in the section on sub-pixel cluster studies (5.4.4).

5.4.3 Sub-pixel efficiency

The efficiency is determined analogously to the way described in section 5.3.5. Instead of one straight line fit through all telescope layers, tracks are reconstructed using the method described in the previous subsection (5.4.2). The radius of the spatial matching window is chosen to be 100 µm. It is much narrower than for the studies with the MuPix telescope due to the increased pointing resolution. The MIMOSA-26 hits do not have any timing information except for the TLU ID. Therefore, no time cut is applied for the DUT hit matching. Readout frames are constructed from two consecutive MIMOSA-26 readout cycles that have one TLU ID assigned to them [82]. DUT hits can end up in one readout frame before and one readout frame after the one that contains the track. Consequently, matching hits are searched for within three readout frames.
An ATLASPix_Simple sample with a nominal substrate resistivity of 200 Ωcm and a nominal thickness of 100 µm was used as DUT for the studies presented in the following. Two different sensor configurations were investigated: One

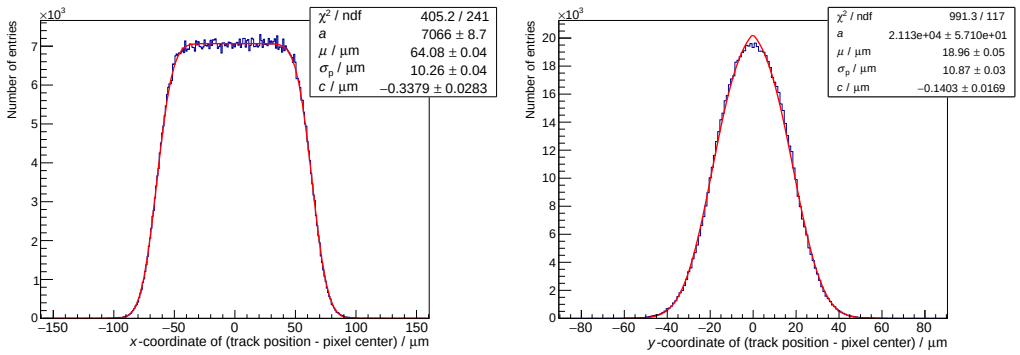

(a) (b)

Figure 5.51: Distributions of the x- (a) and y-coordinates (b) of the difference of the track position on the DUT and the pixel center of a matched single hit

with a threshold of 70 mV and an HV of −60 V, which is expected to yield high efficiencies, and one with a higher threshold of 150 mV and an HV of −15 V. Based on the results presented in section 5.3.5, one expects an efficiency of around 90 % for the second configuration. Figure 5.52 shows pixel maps of the efficiency, measured with the two configurations. The average efficiency is ca. 99.95 % for the fist setting and ca. 90.6 % for the second one.

Figure 5.53a shows the efficiency of the second (less efficient) setting mapped onto an area of 2×2 pixels and plotted with sub-pixel resolution. The ratio of the pixel edges is approximately drawn to scale. The inefficient regions are mostly located around the pixel edges and especially in the pixel corners. Subfigures (b) and (c) show the projections of the plot in subfigure (a) onto the x-axis for two different y-ranges, one covering the more efficient regions going through the pixel centers ($10\,\mu\text{m} < y < 30\,\mu\text{m}$), the other covering the region around the long pixel edge ($35\,\mu\text{m} < y < 45\,\mu\text{m}$). Subfigures (d) and (e) show the analog plots for projections onto the y-axis. The respective x-regions are $30\,\mu\text{m} < x < 100\,\mu\text{m}$ and $120\,\mu\text{m} < x < 140\,\mu\text{m}$.
The average efficiency in the pixel center is ca 95 %, while in the pixel corners it is ca. 89 %. In the region along the long pixel edge, the efficiency has a maximum of about 94 %, which represents only a slight deterioration compared to the pixel center. Along the short edge of the pixel the efficiency reaches only a maximum of approximately 85 %.
When a pixel is hit close to one of its short edges, it is likely that the signal charge is shared among three or four pixels, leading to relatively small signals

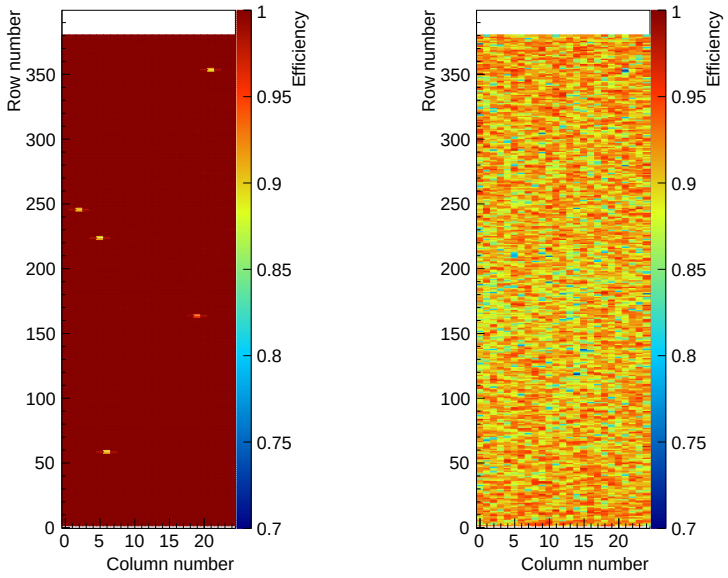

(a) Threshold = 70 mV, HV = −60 V

(b) Threshold = 150 mV, HV = −15 V

Figure 5.52: Pixel maps of efficiency for two different threshold/HV settings

in the individual involved pixels. Hits in most part of the region around the long edge of the pixel lead to charge sharing among only two pixels, which results only in a small inefficiency. The results are consistent with those on hit clusters presented in the following section 5.4.4 and in section 5.3.6.

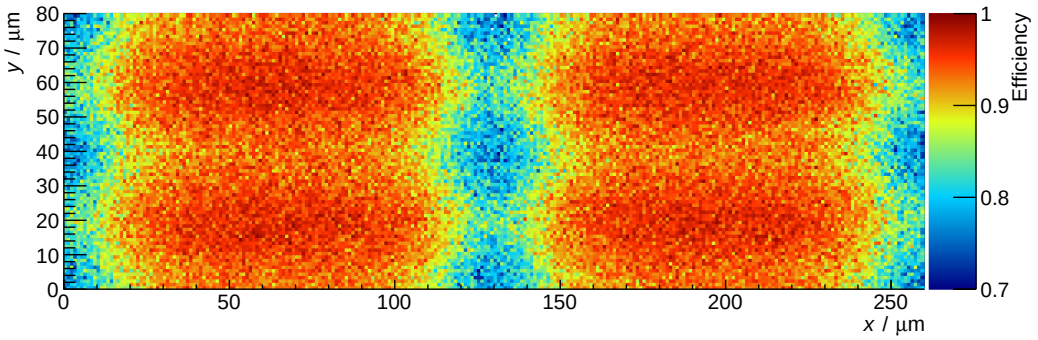

(a) Efficiency mapped onto 2×2 pixels

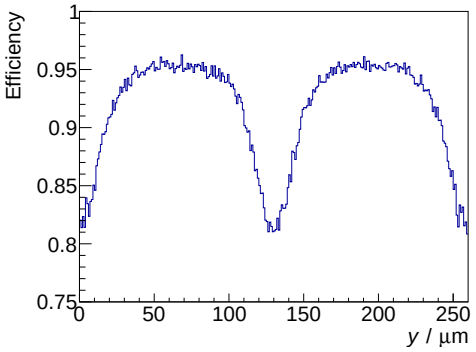

(b) x-projection for $10\,\mu\text{m} < y < 30\,\mu\text{m}$

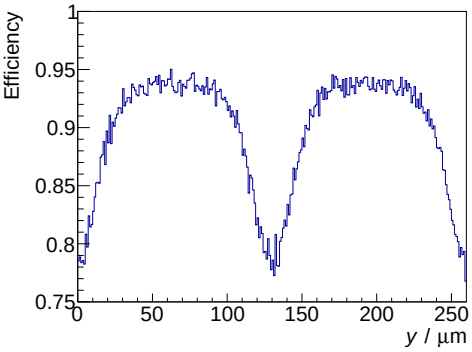

(c) y-projection for $35\,\mu\text{m} < y < 45\,\mu\text{m}$

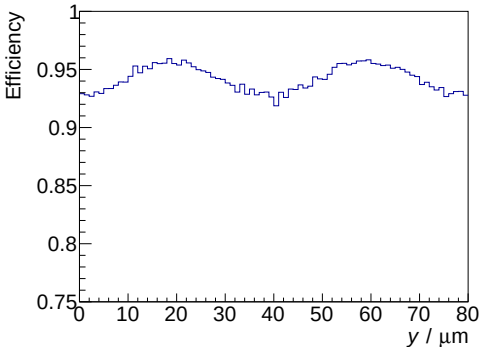

(d) y-projection for $30\,\mu\text{m} < x < 100\,\mu\text{m}$

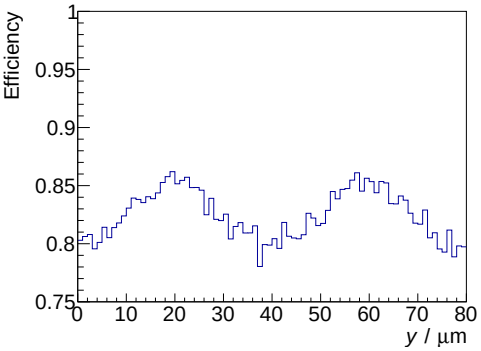

(e) y-projection for $120\,\mu\text{m} < x < 140\,\mu\text{m}$

Figure 5.53: Efficiency mapped onto an area of 2×2 pixels (a) and different projections on x- and y-axis (b)-(e)

5.4.4 Sub-pixel studies of hit clusters

The occurence of hit clusters due to charge sharing is discussed in section 5.3.6. Clustering is studied with sub-pixel resulution based on the data taken with the sensor configuration discussed in the previous section 5.4.3 that leads to a high efficiency. The threshold value is 70 mV and the HV is −60 V.
Figure 5.54 shows the extrapolated track positions in the DUT plane of tracks with matched (a) single hits, (b) two-hit clusters, (c) three-hit clusters, and (d) four-hit clusters mapped onto an area of 2×2 pixels.
Subfigures (a) and (b) are consistent with each other. When a pixel is hit in its center, the signal charge is expected to be collected within this pixel alone. When a pixel is hit close to an edge, charge sharing occurs mostly among two pixels.
Figure 5.55 shows the x-projection of subfigure (b) for $15\,\mu\text{m} < y < 25\,\mu\text{m}$ after subtracting a constant offset of 185 entries from each bin. An s-curve is fitted simultaneously to both edges of the central peak, analogously to figure 5.51. The parameter of the s-curve called μ in equation 5.11 corresponds here to the width w of the region where hits result in double clusters. In section 5.3.6, w is determined to equal $(8.2 \pm 1.9)\,\mu\text{m}$ for HV = −60 V, based on the ratio of the numbers of vertical and horizontal two-hit clusters. σ_{dc} should equal $\sigma_{\text{p,x}} = (10.3 \pm 0.1)\,\mu\text{m}$.
Subfigure (a) shows the fit for the free parameters σ_{dc}, w, a, and c. It yields $\sigma_{\text{dc}} = (4.9 \pm 0.3)\,\mu\text{m}$, which is significantly smaller than the $\sigma_{\text{p,x}}$ determined above (see figure 5.51a). The fit yields $w = (12.9 \pm 0.4)\mu\text{m}$.
When fixing the value $\sigma_{\text{dc}} = \sigma_{\text{p,x}} = 10.3\,\mu\text{m}$, the fit yields $w = (4.5 \pm 0.4)\,\mu\text{m}$. As discussed above (section 5.4.2), $\sigma_{\text{p,x}}$ might be overestimated. When fixing $w = 8.2\,\mu\text{m}$ instead of σ_{dc}, the resulting fit looks similar to that in subfigure (b) and the fit result for σ_{dc} is $(8.1 \pm 0.2)\,\mu\text{m}$.
Hits in a pixel corner can result in charge sharing between three and four pixels. Subfigures (b) and (c), for which a coarser binning is used than for subfigures (a) and (b), show the accoring distributions of 3-hit and 4-hit clusters. The effect is clearly resolved in the x-dimension but not as clearly in the y-dimension due to the corresponing small pixel pitch.

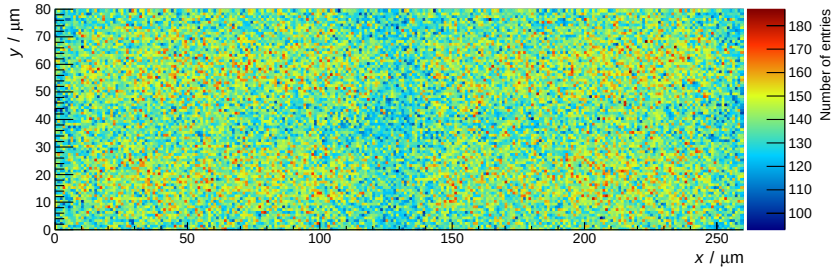

(a) Single hits (4581448 entries)

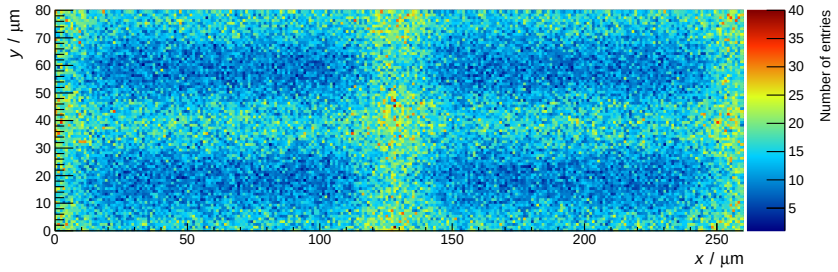

(b) Two-hit clusters (442216 entries)

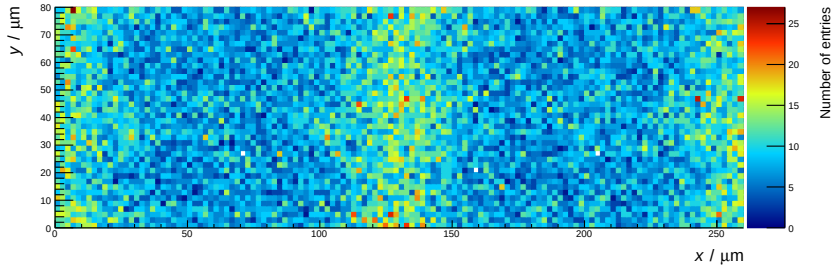

(c) Three-hit clusters (43736 entries)

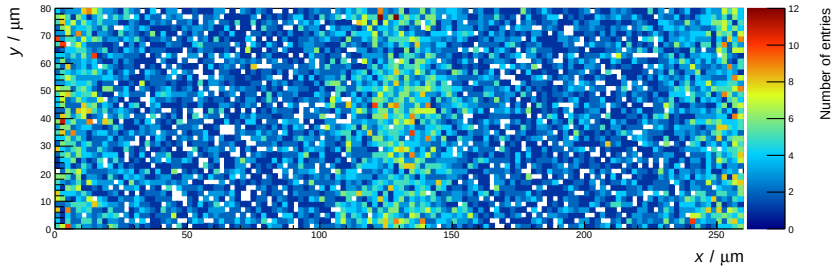

(d) Four-hit clusters (12798 entries)

Figure 5.54: Track position on the DUT mapped onto the area of 2×2 pixels for different sizes of the matched cluster

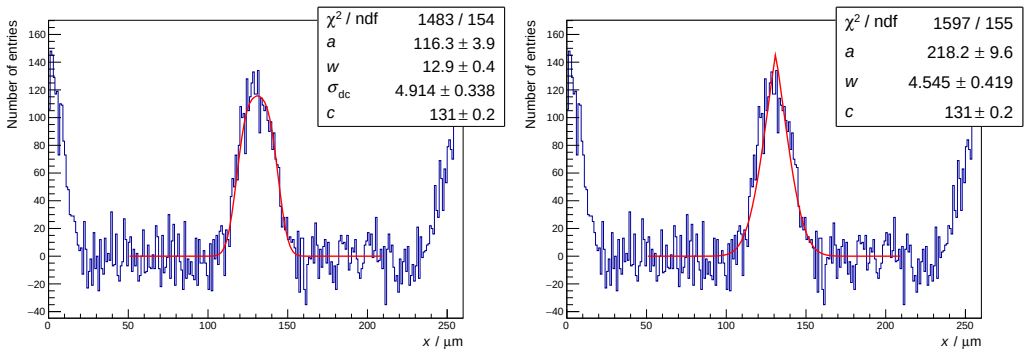

(a) s-curve fit with free parameter σ_{dc} (b) s-curve fit with $\sigma_{\mathrm{dc}} = 10.3\,\mu\mathrm{m}$ fixed

Figure 5.55: x-projection of distribution of two-hit clusters for $15\,\mu\mathrm{m} < y < 25\,\mu\mathrm{m}$ minus a constant offset

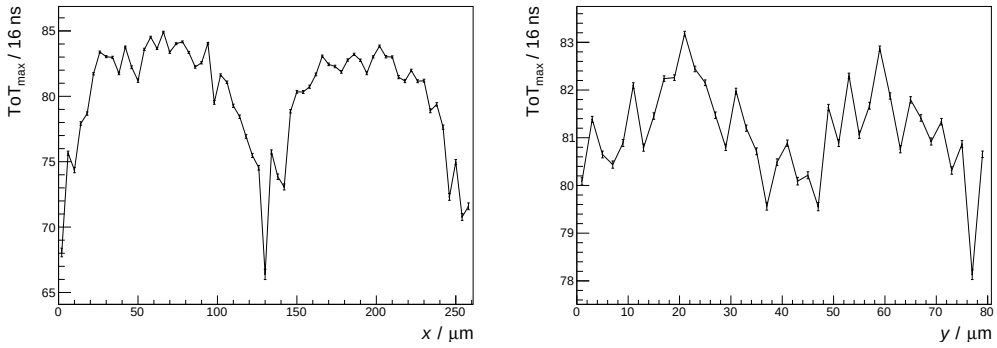

(a) (b)

Figure 5.56: Peak position of ToT distribution vs one-dimensional track position mapped onto two times one pixel length in x (a) and y (b)

5.4.5 Sub-pixel timing

The results presensted in this section are based again on the high-efficiency dataset discussed in section 5.4.3 (threshold = 70 mV, HV = −60 V).
The peak positions of the ToT distribution and the TS1 − t_{ref} distribution as well as the time resolution (σ) of matched clusters are plotted against the track position. All track positions in the ROI are mapped onto a distance of two times the pixel size in both dimensions separately. The data is analyzed and plotted in 4 µm slices and 2 µm slices in x and y, respectively. For each cluster, the earliest time of arrival and the largest ToT are used. ToT and TS1 − t_{ref} are corrected for their dependence on the row number as described in section 5.3.8.
Figure 5.56 shows the peak of the ToT distribution plotted against both the x- and the y-coordinate of the track position. The resluts are consistent with what is observed for efficiency and cluster distributions. The signal charge from a hit in the central pixel region is collected within one pixel. Hits close to a pixel edge lead to charge sharing among two or more pixels, leaving each pixel with a comparatively small signal. Smaller signals correspond to smaller ToTs. For the projection onto the y-axis in subfigure (b), the effect is less pronounced because the data is averaged over the x-dimension, where, for the most part, no three-hit and four-hit clusters occur.
Figure 5.57 shows the peak position of the TS1−t_{ref} distribution and σ plotted against the x-coordinate of the extrapolated track position before (a) and after (b) timewalk correction. Due to the correction for the variation of TS1 − t_{ref} over the row number, the plotted values are around zero. This does not correspond to the absolute TS1 − t_{ref} values. Only variations within a pixel

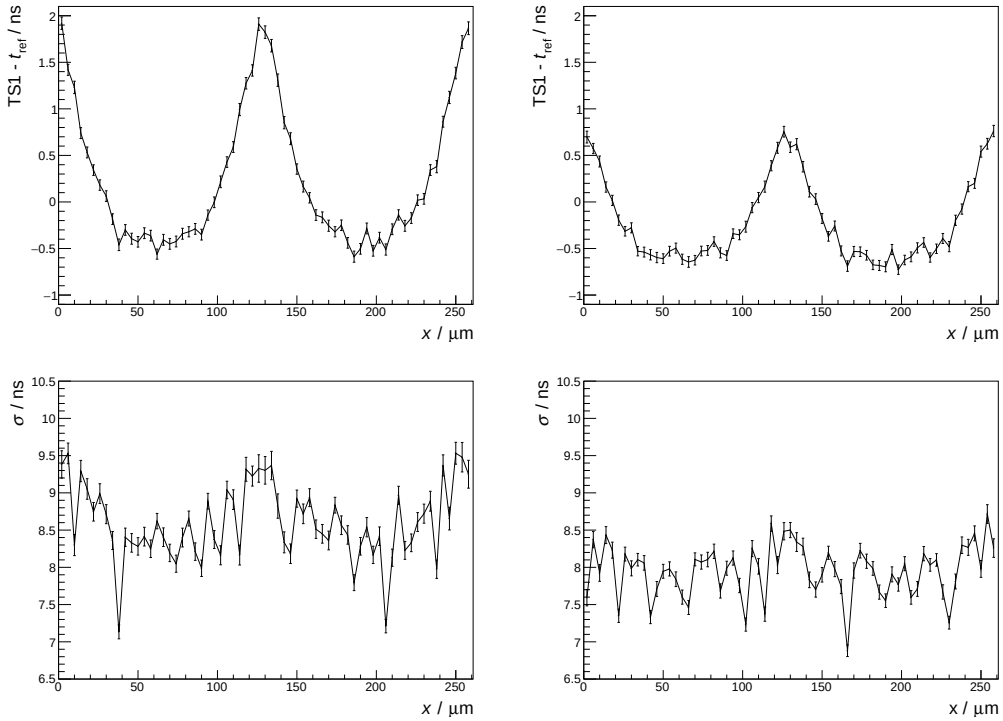

(a) Not corrected for timewalk (b) Corrected for timewalk

Figure 5.57: Peak position of TS1 $- t_{\text{ref}}$ distribution and σ vs x-coordinate of track position mapped onto two times one pixel length with (b) and without (a) timewalk correction

are studied. Before timewalk correction, TS1 $- t_{\text{ref}}$ is ca 2.5 ns smaller in the pixel center than at the pixel edges. With timewalk correction, the difference becomes smaller. This is expected because the smaller signals resulting from charge sharing have a larger timewalk. However, the distribution is still not flat after timewalk correction. This implies that the charge collection is more efficient in the pixel center, independent of the signal size. The σ distributions are consistent with the above observations. Besides an overall decrease after timewalk correction, the distribution becomes flatter. Still, the time resolution remains ca. 0.5 ns worse at the pixel edges than in the pixel center.

Figure 5.58 shows the analog plots for the y-dimension. In the delay distribution, one can observe a clear structure that corresponds to alternating pixel rows. The pixels that are projected to the left side of the plot show a minimum of ca. -0.7 ns at the y-value that corresponds to the pixel center. The pixels that are projected to the right side of the plot show a plateau of

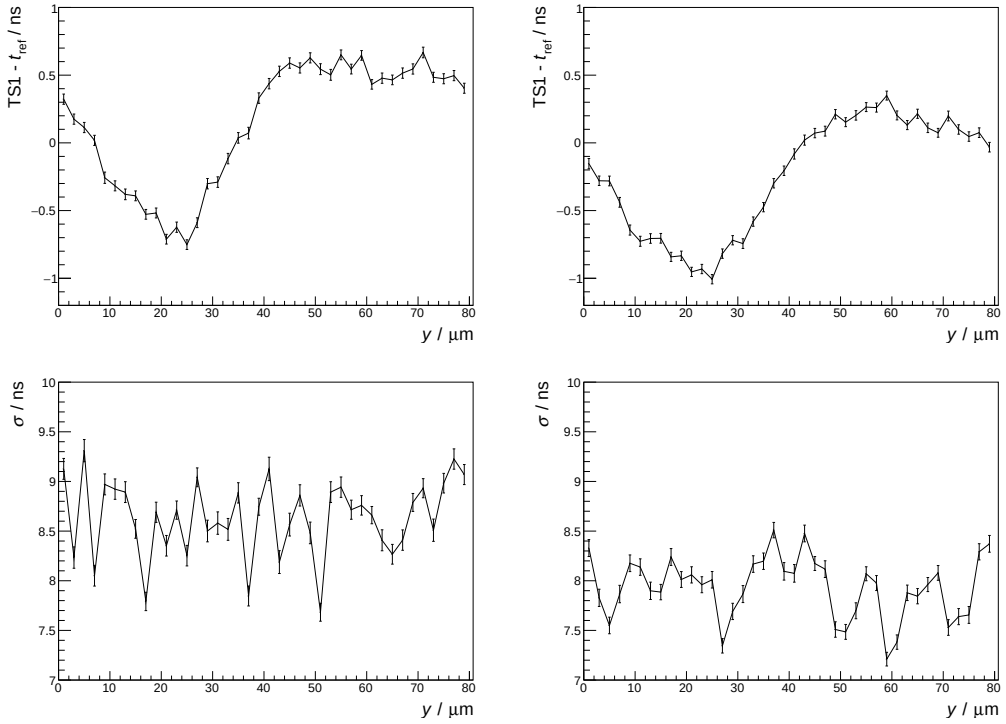

(a) Not corrected for timewalk (b) Corrected for timewalk

Figure 5.58: Peak position of TS1 $- t_{\text{ref}}$ distribution and σ vs y-coordinate of track position mapped onto two times one pixel length with (b) and without (a) timewalk correction

ca. 0.5 ns. The layout of the readout cells is in fact differnt for every second row. The readout cells of two consecutive rows are mirrored with respect to the x-axis. It is not known what exactly causes the effect. It is excluded that it is caused by crosstalk because it is still present when only taking into account hits within the regions on the sensor where the crosstalk probability is small. The opposite orientation of the transistors with respect to the silicon crystal and the resulting opposite direction of the current through them can have an effect on their conductivity, which could be an explanation.
Timewalk correction reveals a sub-pixel structure in the σ- distribution that is similar for the left and the right half of the according plot (subfigure (b), bottom).

5.5 Studies on radiation tolerance

The sensors of layer 4 of the ITk are expected to be exposed to a 1 MeV neutron equivalent fluence of approximately $1 \cdot 10^{15}\,\mathrm{n_{eq}/cm^2}$ and a TID of approximately $5 \cdot 10^5\,\mathrm{Gy}$ over the full runtime of the detector (see section 2.2.3). Several ATLASPix1 samples were irradiated with different neutron and proton fluences to test the sensor performance after irradiation. During such so-called irradiation campaigns, the sensors are irradiated with the respective fluence in a short time (typically of the order of minutes or hours) compared to the detector runtime. This is achieved by using high rate particle beams or nuclear reactors. All irradiated samples tested within the scope of this thesis are listed in section 5.5.1 together with information on the corresponding irradiation campaigns. Since the irradiation, the samples have been stored in refrigerators at $\leq -20\,^\circ\mathrm{C}$ to prevent annealing. They were glued and wire-bonded to the insert PCB after irradiation, for which they had to be at room temperature for ca. two hours. During measurements, the samples are cooled with nitrogen gas flow using the cooling setup described in section 5.5.2. For mounting the samples into the cooling setup before measurements and dismounting them afterwards, they are heated up to room temperature for approximately 15 minutes in total. During transport, irradiated samples are cooled either with ice, dry ice, or refrigerant gel packs.

5.5.1 Irradiated samples

The studies presented in this section are based on two irradiation campaigns. One was carried out at the TRIGA Mark II research reactor operated by the Jožef Stefan Institute (JSI) in Ljubljana [83]. Here, ATLASPix1 samples were irradiated with reactor neutrons. In the second campaign, samples were irradiated using an 18 MeV proton beam at the cyclotron laboratory in Bern [84]. The fluences are given by both irradiation facilities directly as 1 MeV neutron equivalent. There is one sample available per combination of fluence and particle species. All samples are listed in table 5.2.

The samples were not powered during irradiation. They were glued and bonded to the insert PCB afterwards.
At JSI, samples with both available nominal substrate resistivities (80 Ωcm and 200 Ωcm) were irradiated with the 1 MeV neutron equivalent fluences of $1 \cdot 10^{14}$, $5 \cdot 10^{14}$, $1 \cdot 10^{15}$, and $2 \cdot 10^{15}\,\mathrm{n_{eq}/cm^2}$. One of the eight samples turns out not to be fully functional due to an unusually high reverse-bias leakage current of $> 500\,\mu\mathrm{A}$ already for an HV of $-1\,\mathrm{V}$. However, the sample can

Particles	Fluence / n_{eq}/cm^2	80 Ωcm	200 Ωcm
Neutrons (JSI)	$1 \cdot 10^{14}$	✓	non-operational
	$5 \cdot 10^{14}$	✓	✓
	$1 \cdot 10^{15}$	✓	✓
	$2 \cdot 10^{15}$	✓	✓
Protons (Bern)	$1 \cdot 10^{14}$	-	non-operational
	$5 \cdot 10^{14}$	-	✓

Table 5.2: List of irradiated samples

still be configured. There is one cluster of $\mathcal{O}(10)$ very noisy pixels. All other pixels behave normally and are able to detect electrons from a ^{90}Sr source. Only two samples are available that were irradiated with protons. Both have a substrate resistivity of 200 Ωcm and the 1 MeV neutron equivalent fluences are $1 \cdot 10^{14}$ and $5 \cdot 10^{14}$ n_{eq}/cm^2. The sample that was irradiated with the lower fluence cannot be configured. Consequently, it is not operable. The proton fluence of $5 \cdot 10^{14}$ n_{eq}/cm^2 corresponds to a TID of $4.8 \cdot 10^5$ Gy (according to the irradiation facility).

5.5.2 Cooling setup

The irradiated samples are tested using the same setups as for unirradiated sensors (see section 5.1), extended by a cooling system for the DUT. It is based on a cool nitrogen gas flow, which is in direct contact with the backside of the sensor. The purpose of actively cooling the sensor during operation is twofold: First, it reduces annealing. A powered sensor that is not actively cooled has a temperature between 40 °C and 60 °C, depending on the chip configuration. Cooling with the setup described below keeps the sensor temperature approximately between 0 °C and 5 °C. This temperature difference changes the rate of annealing by several orders of magnitude [47]. Secondly, the leakage current in the sensor diode significantly increases with radiation damage for the fluences under investigation (see section 5.5.3). Cooling reduces the effect such that the sensors can still be operated at high reverse bias voltages.
Figure 5.59 shows how the nitrogen gas cooling is realized. The sensor is enclosed by a plastic cooling box along with the insert and the mother PCB. The box is designed such that it can be mounted to the aluminum frames of the MuPix telescope. It has beam windows on both sides of the sensor that are covered with thin polyimide foil. The box features feed-throughs for all

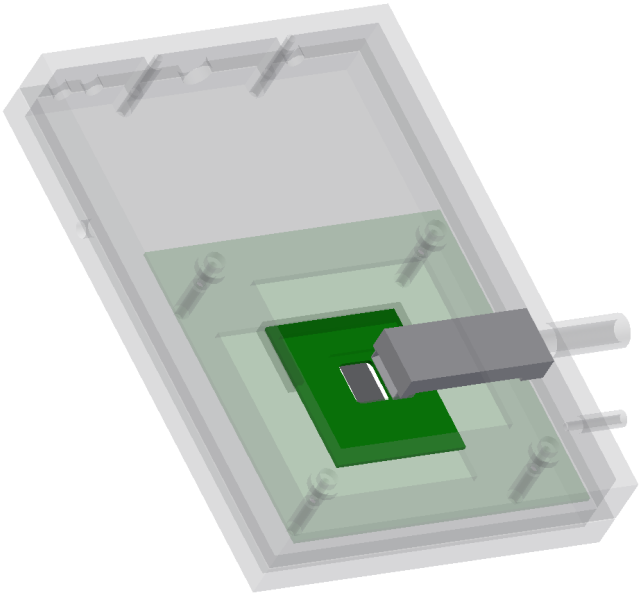

Figure 5.59: Drawing of gas cooling box for irradiated sensors including mother PCB, insert PCB, and sensor (view from backside)

cable connections of the mother PCB as well as connections to the cooling gas line and to a second gas line that is used for flushing the box with dry gas before cooling. Inside the box the gas flow is directed onto the backside of the sensor. This is possible due to cutouts underneath the sensor in both the insert and the mother PCB (see section 5.1.1).
The gas is cooled down to about $-20\,°C$ with a laboratory chiller. The gas line between chiller and cooling box is kept as short as possible and wrapped in pipe insulation. Still, the gas warms up again to approximately $-10\,°C$ before reaching the cooling box.
A gas flow of $2\,m^3/h$ is applied and monitored using a float-type flowmeter. The system is not closed, i.e. the nitrogen is led into the surrounding air on the outlet side.
During long periods of operation, the whole telescope is placed inside a dry nitrogen atmosphere to prevent condensation and ice on the outside of the cooling box and on close-by electronics. The nitrogen atmosphere is realized by an acrylic glass box, again, with polyimide beam windows on both sides. It features a patch panel for all required BNC connections and the gas inlets for flushing as well as feed-throughs for the SCSI cables and the thermally insulated cold gas line.
One advantage of the this cooling setup is that it requires only pressurized nitrogen, which is usually available at testbeam facilities either in gas cylinders or as boil-off of a liquid nitrogen reservoir. The handling of liquid nitrogen is avoided. Furthermore, no heat sink and therefore extra material has to be placed in the beam, which would increase the amount of multiple scattering.

Sensor temperature determination: It is not straight forward to get a good estimate on the sensor temperature during the operation of the cooling system. A contactless temperature measurement can be performed with an infrared (IR) camera, but not during normal operation. The lid of the cooling box needs to be left open for the camera to point directly onto the sensor with no obstacles in between and the camera needs to be placed inside the dry atmosphere together with the sensor.
To estimate the temperature that the sensors had at the testbeam campaigns discussed below (see section 5.5.5), reference measurements were performed in the laboratory under conditions that reproduced those at the testbeam as well as possible. The chiller was set to the temperature it had at the corresponding testbeam campaign and the same length for the thermally insulated gas line between chiller and sensor was used. However, there could still have been differences, e.g. in ambient temperature.
The reference measurements were performed for chiller temperatures of $-16\,°C$

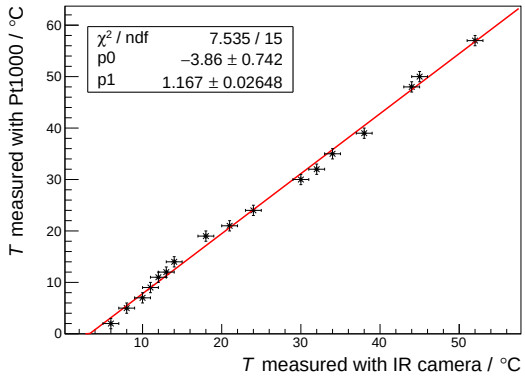

Figure 5.60: Calibration curve for the measurement of the sensor temperature with an IR camera

and −17 °C. A measurement without cooling was performed in addition. The chiller temperatures correspond to the respective minimum chiller temperatures that could be reached with the maximum cooling power on two of the three testbeam campaigns. −17 °C is also the minimum chiller temperature that was reached in the laboratory where the reference measurements were performed. At the third testbeam campaign, the minimum reachable chiller temperature was ca. −18 °C due to a lower ambient temperature. The corresponding sensor temperature is therefore specified as an upper limit. The actual sensor temperature is assumed to be $\mathcal{O}(1\,°C)$ below.
The IR camera measurement was performed at two points on the sensor, one in the center of the pixel matrix ($T_{IR,\,pix}$) and one on the periphery ($T_{IR,\,per}$). The IR camera needed to be calibrated for the sensor surface, which introduces systematic uncertainties. The calibration was performed by placing an unbonded sensor either on a Peltier element for cooling or on a resistive heater. The temperature was measured with the IR camera and a Pt1000 temperature sensor on the chip's surface. The resulting calibration curve is shown in figure 5.60.
The calibration curve is used to convert the temperature values obtained with the IR camera during the reference measurements discussed above to the actual sensor temperatures T_{pix} and T_{per}. The results are shown in table 5.3. The given errors result from the fit errors and the reading error of the IR measurement.

	$T_{IR,\,pix}$ / °C	$T_{IR,\,per}$ / °C	T_{pix} / °C	T_{per} / °C
no gas flow	40.0 ± 1.0	40.0 ± 1.0	42.8 ± 1.7	42.8 ± 1.7
$T_{chiller} = -16\,°C$	6.5 ± 1.0	8.0 ± 1.0	3.7 ± 1.4	5.5 ± 1.4
$T_{chiller} = -17\,°C$	3.0 ± 1.0	5.0 ± 1.0	-0.4 ± 1.4	2.0 ± 1.4

Table 5.3: Temperatures measured with IR camera and deduced sensor temperatures

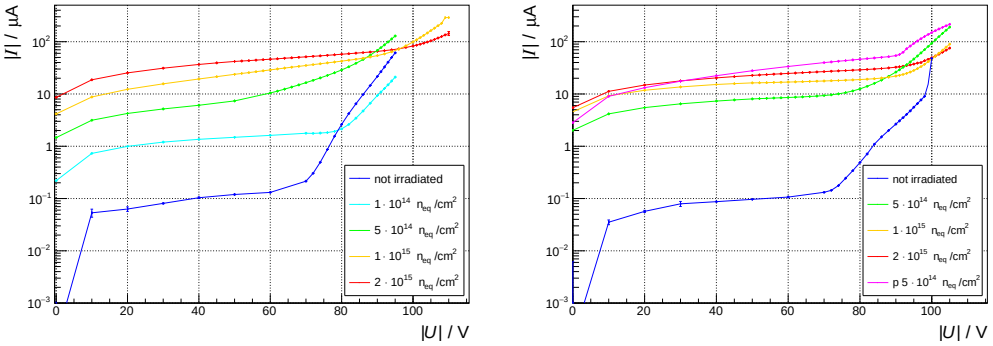

(a) 80 Ωcm (b) 200 Ωcm

Figure 5.61: Current-voltage characteristics after irradiation with different fluences; the proton fluence is labeled with 'p'

5.5.3 Leakage current after irradiation

The current-voltage characteristic of the reverse bias was measured for all normally functioning irradiated samples at a temperature of ca. 0 °C. The results are shown in figure 5.61. As expected, the leakage current increases with the fluence.

Figure 5.62 shows the leakage current plotted against the neutron fluence at HV = −40 V. It is discussed in section 3.3.2 that the leakage current is expected to be proportional to first order to the fluence and to the width W of the depletion region. Assuming that this is true, the non-linearities in this plot result from a change in the width of the depletion region W due to changes in the effective doping concentration. For the substrate resistivity of 200 Ωcm, it would mean that W decreases above a fluence of $1 \cdot 10^{15}\,n_{eq}/cm^2$. For the substrate resistivity of 80 Ωcm, it would mean that W increases first and then stabilizes or decreases above a fluence of $1 \cdot 10^{15}\,n_{eq}/cm^2$.

This would be consistent with measurements performed to study acceptor removal with sensors that have a p-type bulk and substrate resistivities of $\mathcal{O}(10\,\Omega cm)$. It has been found that N_{eff} decreases for fluences between

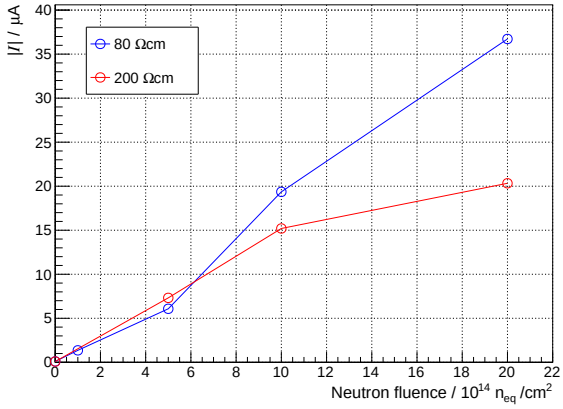

Figure 5.62: Reverse-bias leakage current vs neutron fluence at HV = −40 V

$5 \cdot 10^{14}\,\mathrm{n_{eq}/cm^2}$ and $1 \cdot 10^{15}\,\mathrm{n_{eq}/cm^2}$ [51].
In principal, the width of the depletion region can be measured with the edge transient-current technique (TCT). However, this was not possible within the scope of this thesis.
Around the breakdown regime of the unirradiated sensors, the initially lower curves in figure 5.61 cross the higher curves. The breakdown occurs at a larger bias for higher fluences or at least not as abrupt.
At least up to a fluence of $1 \cdot 10^{15}\,\mathrm{n_{eq}/cm^2}$, an increase of W, as discussed above, and the resulting smaller electric field could explain this effect. Furthermore, the increased probability of charge trapping at high fluences could suppress an avalanche breakdown.
The sample that was irradiated with a proton fluence of $5 \cdot 10^{14}\,\mathrm{n_{eq}/cm^2}$ has a comparatively high leakage current. The studies on acceptor removal mentioned above showed that the fraction of removed acceptors is larger for proton irradiation than for neutron irradiation [50]. The observed higher leakage current for proton irradiation than for neutron irradiation at a fluence of $5 \cdot 10^{14}\,\mathrm{n_{eq}/cm^2}$ would be consistent with that due to the resulting larger W.
Figure 5.63 shows the leakage current plotted against the neutron fluence for HV = −60 V, a substrate resistivity of 80 Ωcm, and two different temperatures. The measurements were taken at two of the testbeam campaigns discussed below (section 5.5.5). For one of the campaigns, no exact temperature reference measurement could be performed (see section 5.5.2). The sensor temperature was estimated to be $\mathcal{O}(1\,^\circ\mathrm{C})$ below 0 °C. The above results are in accordance with the rule of thumb that the leakage current increases by a factor of two for a temperature increase of 8 K (see section 3.1) if the

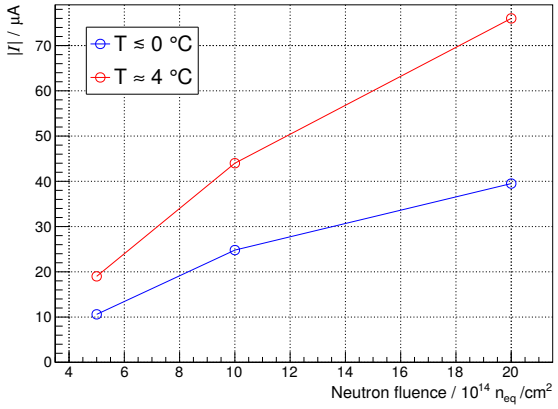

Figure 5.63: Reverse-bias leakage current vs fluence for a substrate resistivity of 80 Ωcm and two different temperatures (HV = −60 V)

according sensor temperature equals ca. −3 °C.

5.5.4 Threshold dispersion and SNR after irradiation

The threshold dispersion and the SNR of the sample with a nominal substrate resistivity of 200 Ωcm that was irradiated with a neutron fluence of $1 \cdot 10^{15}\,\mathrm{n_{eq}/cm^2}$ is determined in the same way as those of an unirradiated sample (see section 5.3.4). The signals were created by mono-energetic photons from an ^{55}Fe source. The HV was −60 V. A VPPix value of 40 was used and the sensor was cooled to ca. 0 °C. The measurement was repeated with an unirradiated sample under the same conditions for comparison. Figure 5.64 shows the μ and σ_n parameters of the s-curves of all pixels of the irradiated sample. Both pixel maps show uniform distributions.
Figure 5.65 shows both parameters histogrammed for the irradiated and the unirradiated sample, yielding the noise and the threshold dispersion. Charge trapping leads to smaller signals for the irradiated sample, i.e. to a shift of the μ-distribution to smaller values compared to those of the unirradiated sample. The noise level represented by σ_n is significantly higher after irradiation. The mean values, RMS, and the resulting SNR are listed in table 5.4.

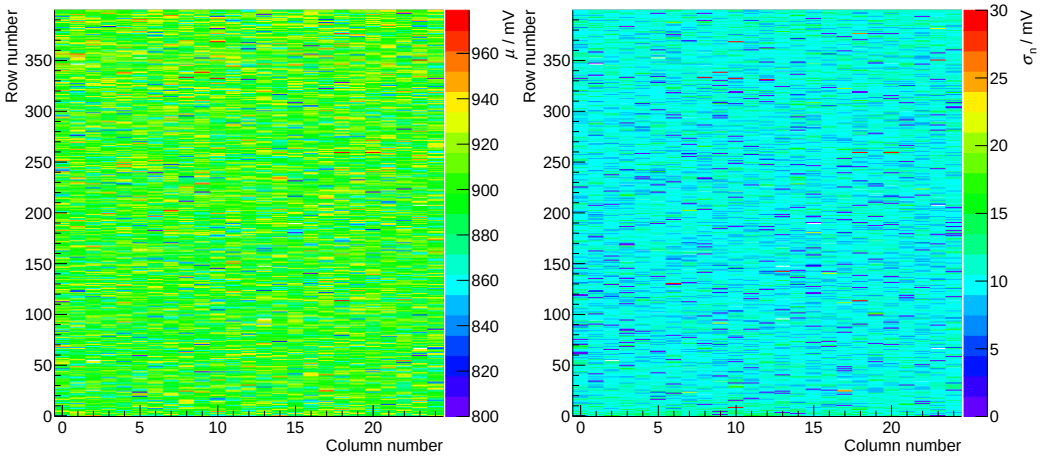

Figure 5.64: Pixel maps of the μ and σ_{n} parameters of the s-curve fits to threshold-scan data measured with a 200 Ωcm sensor irradiated with a neutron fluence of $1 \cdot 10^{15}\,\mathrm{n_{eq}/cm^2}$; the signal source was ^{55}Fe

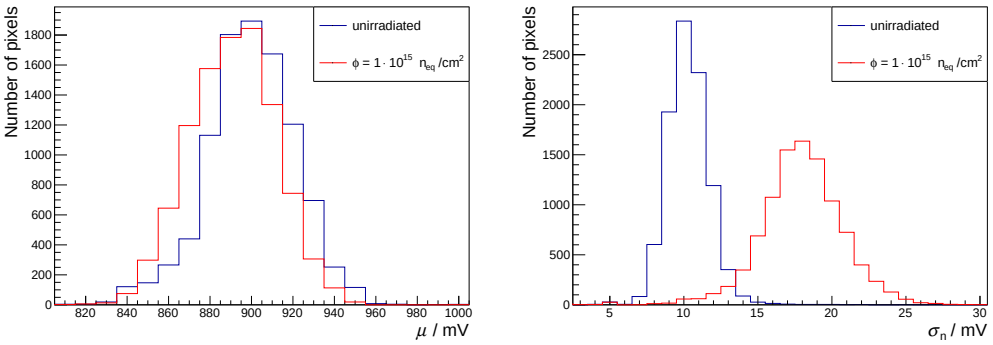

Figure 5.65: Histograms of the μ and σ_{n} parameters of the s-curve fits to threshold-scan data measured using an ^{55}Fe source

ϕ / $\mathrm{n_{eq}/cm^2}$	$\overline{\mu}$ / mV	$\mathrm{RMS_{\mu}}$ / mV	$\overline{\sigma}$ / mV	$\mathrm{RMS_{\sigma}}$ / mV	SNR
0	899.6	21.6	10.1	2.2	9.9 ± 3.0
$1 \cdot 10^{15}$	891.0	20.4	17.9	3.2	5.1 ± 1.5

Table 5.4: Comparison of SNR without irradiation and after irradiation with a neutron fluence of $1 \cdot 10^{15}\,\mathrm{n_{eq}/cm^2}$

	PSI, Aug 2018	DESY, Sep 2018	PSI, Oct 2018
VDD / V	1.9	2.0	1.9
VSSA / V	1.0	1.2	1.0
VMinusPix / V	0.9	0.7	0.7
VPPix value	40	40/63	20
Temperature / °C	$\sim 4\,°C$	$\lesssim 0\,°C$	$\sim 0\,°C$
Tested samples:	200, $5 \cdot 10^{14}$, n	80, $5 \cdot 10^{14}$, n	80, $1 \cdot 10^{14}$, n
resistivity / Ωcm,	200, $1 \cdot 10^{15}$, n	80, $1 \cdot 10^{15}$, n	80, $1 \cdot 10^{15}$, n
fluence / n_{eq}/cm^2,		80, $2 \cdot 10^{15}$, n	80, $2 \cdot 10^{15}$, n
neutrons/protons		200, $2 \cdot 10^{15}$, n	
		200, $5 \cdot 10^{14}$, p	

Table 5.5: List of testbeam campaigns with irradiated samples

5.5.5 Testbeam measurements

The testing of the various irradiated samples in a particle beam was done at three different testbeam campaigns. A different sensor configuration was used at every campaign but within one campaign the same configuration was used for all samples. Table 5.5 lists the testeam campaigns together with the according sensor configurations and the tested samples. The beam momentum at PSI was set to approximately 300 MeV/c and at DESY to approximately 3 GeV/c. The given sensor temperatures are those discussed in section 5.5.2. The temperature of the pixel matrix is given, not that of the periphery. All results were obtained without threshold tuning for individual pixels, but the noisiest pixels were switched off. The higher the fluence and substrate resistivity, the more pixels were switched off to be able to operate the sensor at low thresholds. In the most exreme case, approximately 80 pixels were switched off.

The data analysis for irradiated samples is performed in the same way as for unirradiated samples (see section 5.3).

Figures 5.66 to 5.68 show the average efficiency, the average noise rate per pixel, and the time resolution (σ) for one irradiated sample per subfigure. Every plot includes threshold scans performed for various HV values. The plots in figure 5.67 include results for the same samples from different testbeam campaigns, which allows for comparing the different sensor configurations. The matching windows are chosen to be of the same sizes as for unirradiated samples (see section 5.3.5).

Qualitatively, the irradiated samples behave similar to unirradiated ones (see sections 5.3.5 and 5.3.8). Efficiency and time resolution improve slightly with

the HV. The noise rate does depend on the HV at low thresholds to the extent that there are typically $\mathcal{O}(1)$ more noisy pixels at the same threshold for larger HV values. Those pixels were then masked.
The high noise rates at the lowest thresholds lead to a deterioration of the time resolution (see for example figure 5.68a, bottom). The drop of the noise rate in figure 5.67 at low thresholds is due to saturation of the DAQ system.
The comparison of the different sensor configurations shows that the sensor performance benefits from the configuration used at DESY (see table 5.5). The time resolution is better than with the configuration used at PSI, possibly due to the higher VPPix value. Furthermore, the noise rate is significantly lower due to the increased supply voltage VSSA, as discussed in section 5.3.7.
The proton-irradiated sample (see figure 5.68b) behaves differently than the neutron irradiated samples. The fact that, at thresholds as low as 15 mV, the noise rate is still only 10 Hz per pixel suggests that the working point of the readout electronics has shifted. Only the nMOS transistors, which are considered most critical, are gate-enclosed. TID effects could have occured elsewhere. The sensor is still very efficient (99.6 % at HV = −60 V). It is discussed in section 5.5.3 that acceptor removal might have resulted in a large W for this sensor. At times, the sensor showed an unstable operation, which lead to a noise rate that saturated its readout, using the same sensor configuration that lead to the measured very low noise rates. Charge-up effects could be a reason for that but it is not known where exactly on the chip they would occur. Unstable operation could also explain the efficiency measurements at HV = −60 V and threshold values of 50 mV and 70 mV.

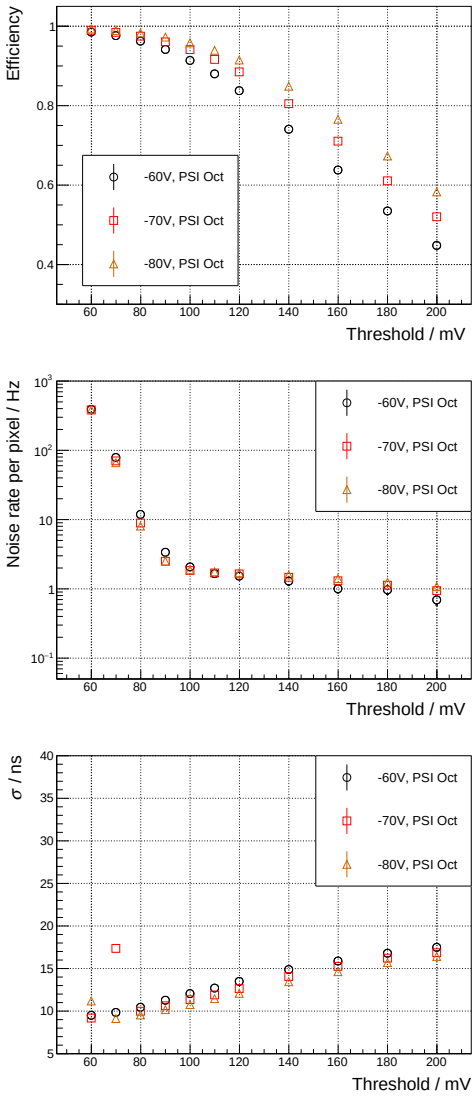

Figure 5.66: Average efficiency (top), average noise rate (middle), and time resolution (bottom) vs threshold for an 80 Ωcm sample irradiated with a neutron fluence of $1 \cdot 10^{14}\,\mathrm{n_{eq}/cm^2}$ measured for different HV values

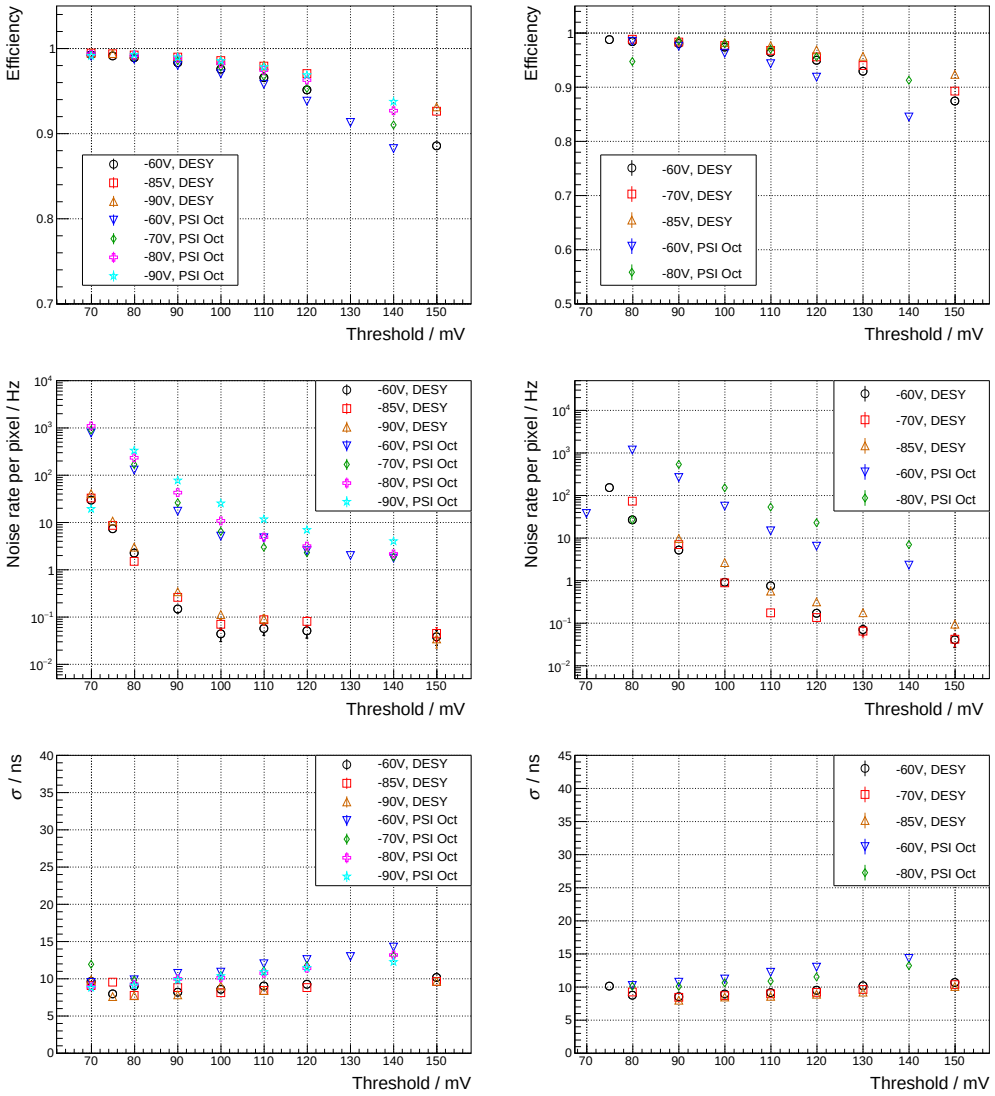

(a) 80 Ωcm,
$1 \cdot 10^{15}\,\mathrm{n_{eq}/cm^2}$ neutrons

(b) 80 Ωcm,
$2 \cdot 10^{15}\,\mathrm{n_{eq}/cm^2}$ neutrons

Figure 5.67: Average efficiency (top), average noise rate (middle), and time resolution (bottom) vs threshold for two 80 Ωcm samples irradiated with different neutron fluences ($1 \cdot 10^{15}\,\mathrm{n_{eq}/cm^2}$ (a) and $2 \cdot 10^{15}\,\mathrm{n_{eq}/cm^2}$ (b)); all scans performed for various HV values on two different testbeam campaigns

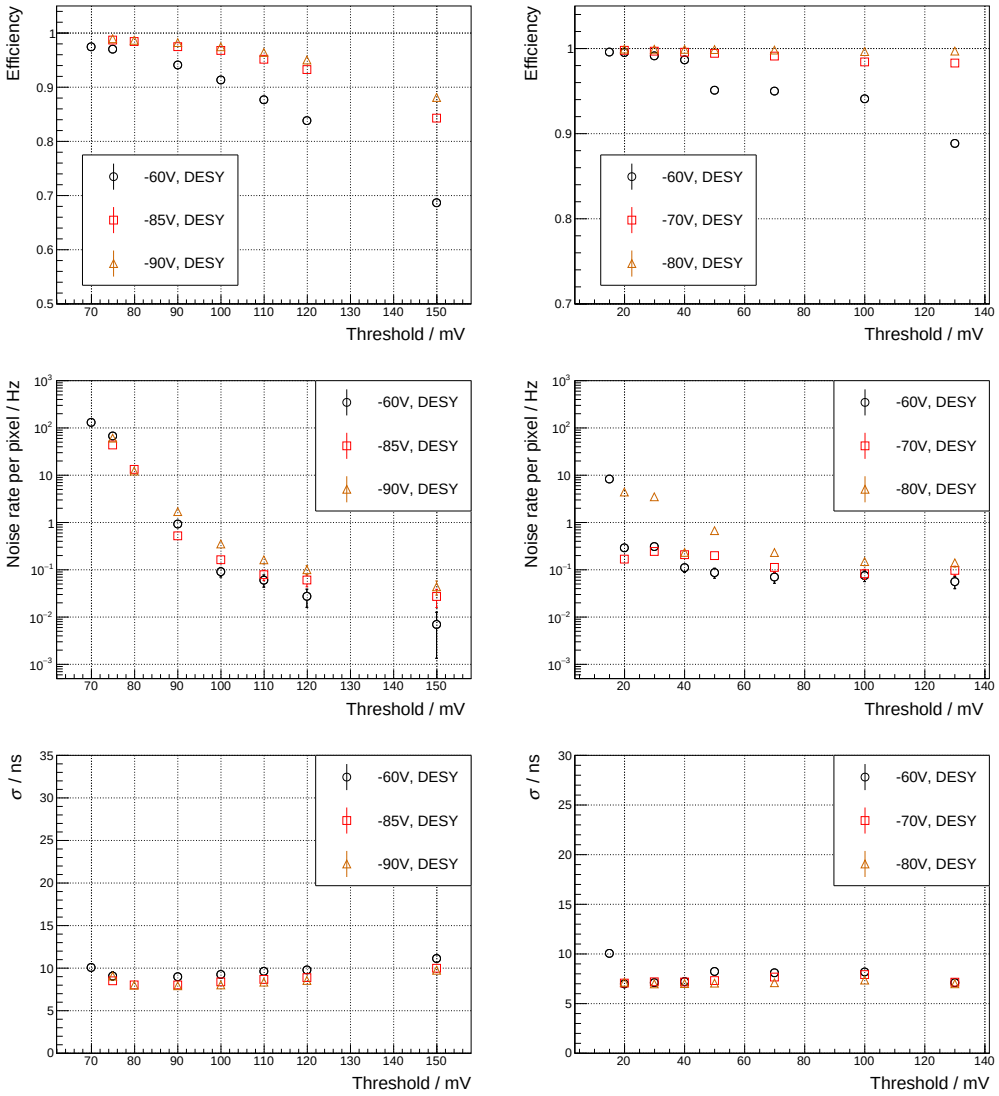

(a) 200 Ωcm, $2 \cdot 10^{15}\,\mathrm{n_{eq}/cm^2}$ neutrons

(b) 200 Ωcm, $5 \cdot 10^{14}\,\mathrm{n_{eq}/cm^2}$ protons

Figure 5.68: Average efficiency (top), average noise rate (middle), and time resolution (bottom) vs threshold for two 200 Ωcm samples: one irradiated with a neutron fluence of $2 \cdot 10^{15}\,\mathrm{n_{eq}/cm^2}$ (a), the other with a proton fluence of $5 \cdot 10^{14}\,\mathrm{n_{eq}/cm^2}$ (b); all scans performed for various HV values

Figures 5.69 and 5.70 show again efficiency, noise, and time resolution plotted against the threshold but here different fluences are compared in each plot. All available data for irradiated samples of one nominal substrate resistivity that was obtained with the same sensor configuration (i.e. at the same testbeam campaign) is plotted together. Data of unirradiated samples is plotted as well, where it is available. The HV is always $-60\,\mathrm{V}$.
During the measurememts with the unirradiated sensor at PSI in October (see figure 5.69b), the coincidence circuit for the reference time measurement did not work reliably. Possibly, either the delays of the scintillator signals or the threshold of a discriminator were not properly adjusted. The according data points for the time resolution for threshold values between 70 mV and 140 mV should therefore be disregarded.
For the PSI testbeam campaign in August 2018 (see figure 5.70b), the matching time window is increased by a factor of two because the measurements were performed with a VMinusPix value of 0.9 V (see 5.3.8). Furthermore, no reference time measurement was performed at this campaign. Consequently, there exists no data on time resolution.
As expected, the noise level starts to increase at higher thresholds for higher neutron fluences (see for example 5.69b, middle). The time resolution does not depend significantly on the fluence. Neither does the efficiency, except for the substrate resistivity of $80\,\Omega\mathrm{cm}$ and the fluence of $1 \cdot 10^{14}\,\mathrm{n_{eq}cm^2}$ (see figure 5.69b, top). Here, the efficiency is lower than for the unirradiated sample and for higher fluences. It has been observed before that sensors with a p-type substrate and low resistivity show a deterioration of their performance for approximatley this fluence, before the beneficial acceptor removal starts to dominate [51]. The effect is not understood.
The maximum efficiencies measured at noise rates per pixel of below 40 Hz for all samples are summarized in table 5.6. The table lists the number of pixels that were masked during the measurement at the lowest threshold and the largest reverse bias. In some cases, the noise limit was reached by masking additional pixels in software during the data analysis. The number of these pixels is given in brackets after the efficiency value.

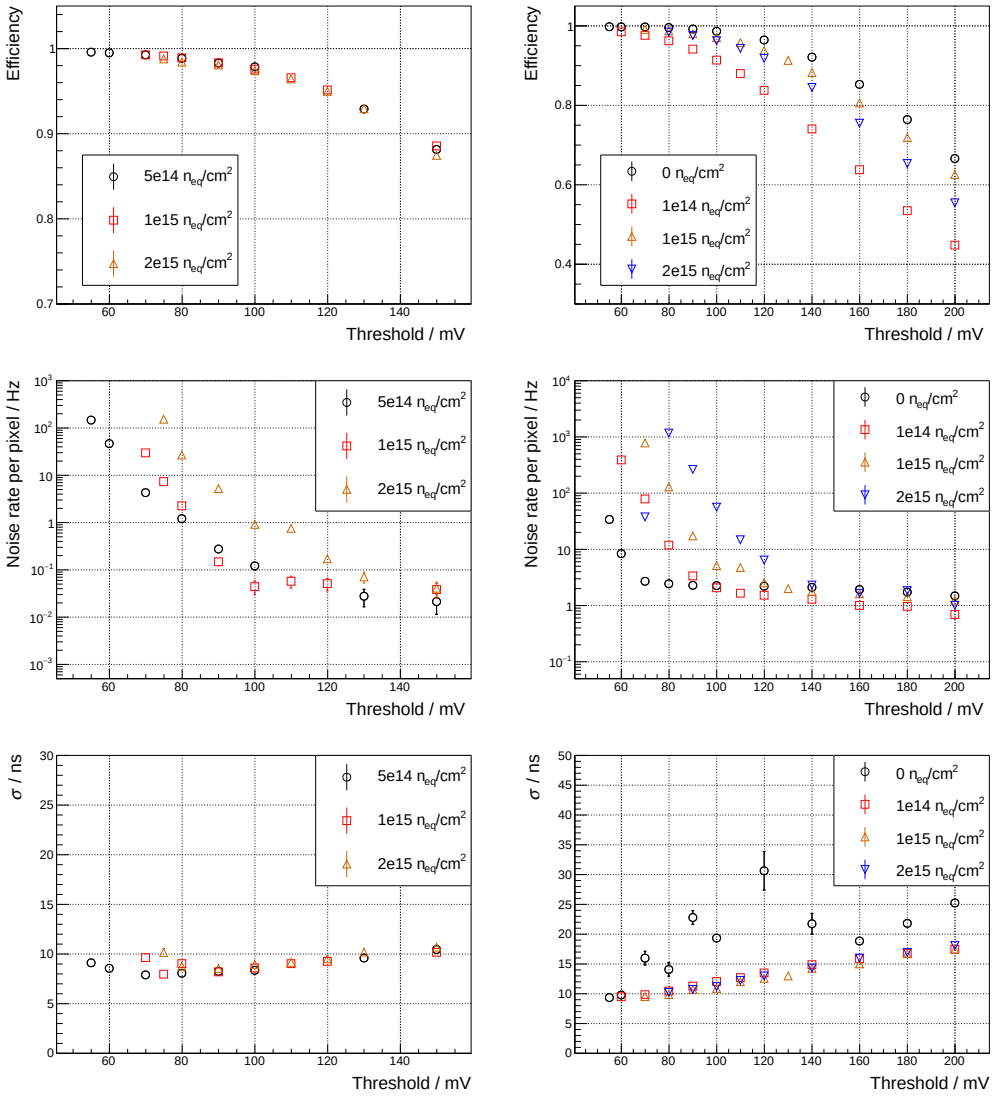

(a) 80 Ωcm, DESY Sep (b) 80 Ωcm, PSI Oct

Figure 5.69: Average efficiency(top), average noise rate (middle), and time resolution (bottom) vs threshold for 80 Ωcm samples, irradiated with different neutron fluences; (a) and (b) measured at different testbeam campaigns using differernt sensor configurations

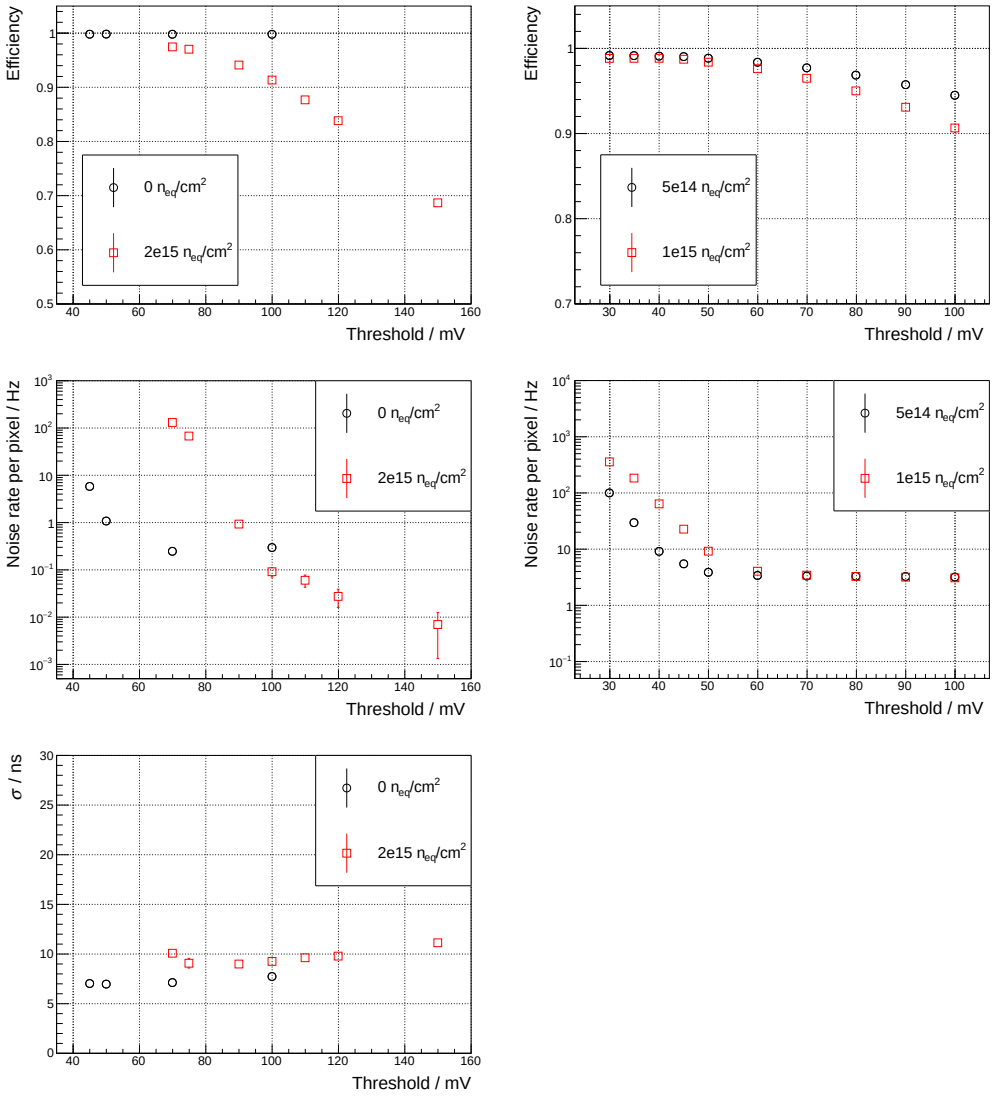

(a) 200 Ωcm, DESY Sep (b) 200 Ωcm, PSI Aug

Figure 5.70: Average efficiency (top), average noise rate (middle), and time resolution (bottom, only (a)) vs threshold for 200 Ωcm samples, irradiated with different neutron fluences; (a) and (b) measured at different testbeam campaigns using differernt sensor configurations

Resistivity / Ωcm	Fluence / n_{eq}/cm^2	#masked pixels	−60 V	−70 V	−80/85 V
			Efficiency / %		
80	$1 \cdot 10^{14}$	26	96.3	97.5	98.3
	$5 \cdot 10^{14}$	17	99.5 (2)	-	-
	$1 \cdot 10^{15}$	38	99.3	-	99.5
	$2 \cdot 10^{15}$	81	98.5	98.4	98.6
200	$5 \cdot 10^{14}$	14	99.2	-	-
	$1 \cdot 10^{15}$	18	98.8	-	-
	$2 \cdot 10^{15}$	55	96.5	-	98.7 (5)
	p $5 \cdot 10^{14}$	≤ 9	99.6	99.7	99.9

Table 5.6: Maximum efficiencies measured with irradidated samples at an average noise rate per pixel of ≤ 40 Hz

Chapter 6

ATLASPix_IsoSimple

While the main focus of this thesis lies on ATLASPix_Simple, the very similar sensor ATLASPix_IsoSimple has also been commissioned and unirradiated samples have been tested in the lab as well as at one testbeam campaign at DESY.
The only differences of ATLASPix_IsoSimple to ATLASPix_Simple is a deep p-well inside the pixel's deep n-well and the implementation of the comparator. The deep p-well is not part of the standard production process. It allows for the use of pMOS transistors as part of the in-pixel comparator because it isolates them from the charge collection region. Consequently, a CMOS comparator is implemented in contrast to ATLASPix_Simple, which has a pure NMOS comparator. In general, CMOS logic draws less current than NMOS logic. Another advantage of the CMOS comparator is that it does not require the voltage VGatePix that has to be supplied to ATLASPix_Simple externally in addition to the main power supply. A schematic of ATLASPix_IsoSimple's CMOS comparator is shown in figure 6.1 [69]. It represents a typical two-stage comparator.

ATLASPix_IsoSimple was operated using the same hardware, firmware, and software as for ATLASPix_Simple (see section 5.1) and measurement data is analyzed in the same way.
All measurements presented in this chapter were performed with a sample that has a nominal substrate resistivity of 200 Ωcm. The focus of the measurements lies on the influence of the comparator on crosstalk, efficiency, and time resolution.

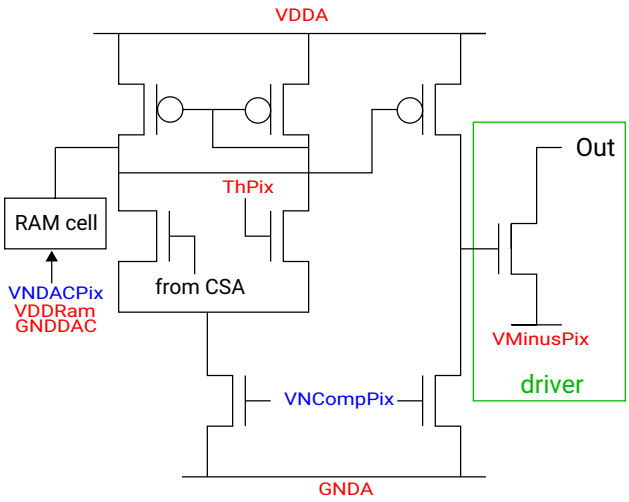

Figure 6.1: Schematic of ATLASPix_IsoSimple's CMOS comparator [69]

Crosstalk

ATLASPix_IsoSimple has a larger line crosstalk probability at the same VMinusPix value than ATLASPix_Simple. Figure 6.2 shows the amount of crosstalk-induced two-hit and three-hit clusters measured at a testbeam with VMinusPix values of 700 mV and 800 mV. The observed structures are coincident with those observed for ATLASPix_Simple but the crosstalk-induced clusters occur with higher probability (see figure 5.33 for comparison). It is assumed that the larger crosstalk probability for ATLASPix_IsoSimple is caused by a larger amplitude and a faster rise of the comparator output. For the measurements discussed in the following, ATLASPix_IsoSimple was operated with a VMinusPix value of 900 mV as default.

Efficiency

Figure 6.3 shows the efficiency of ATLASPix_IsoSimple plotted against the threshold. The measurement was performed at a testbeam at DESY. The HV was −60 V. For the lowest thresholds, the efficiency is 99.90 %. The efficiency plateau is as large as for ATLASPix_Simple (see figure 5.23b for comparison). In contrast to the measurements with ATLASPix_Simple the data was time-sorted on the FPGA during data taking. When using this method, the calculation of the runtime via the FPGA timestamp that is used to determine the noise rate is not correct. Therefore, no data on the noise rate is available. However, the number of unmatched hits in one measurement run is of the same order as for ATLASPix_Simple. Furthermore, without beam the noise rate is observed to be practically zero at the highest threshold

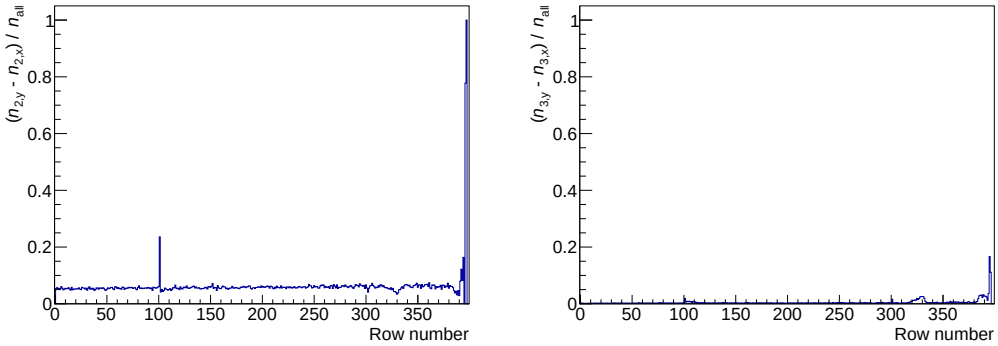

(a) VMinusPix = 800 mV

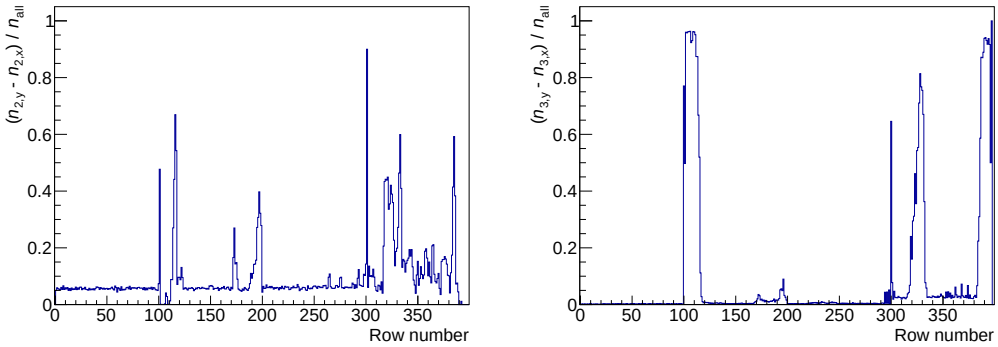

(b) VMinusPix = 700 mV

Figure 6.2: $(n_{2,\mathrm{y}} - n_{2,\mathrm{x}})/n_{\mathrm{all}}$ and $(n_{3,\mathrm{y}} - n_{3,\mathrm{x}})/n_{\mathrm{all}}$ vs row number for different VMinusPix values for ATLASPix_IsoSimple

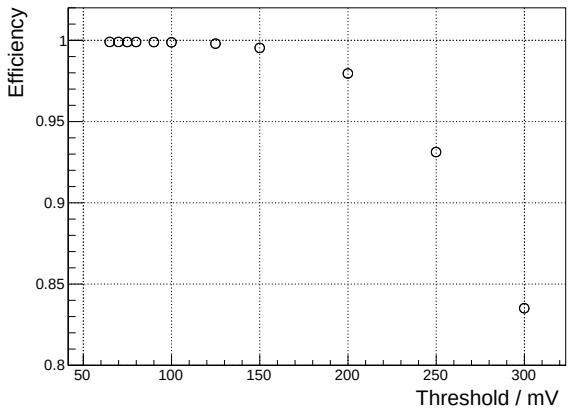

Figure 6.3: Efficiency vs threshold for ATLASPix_IsoSimple

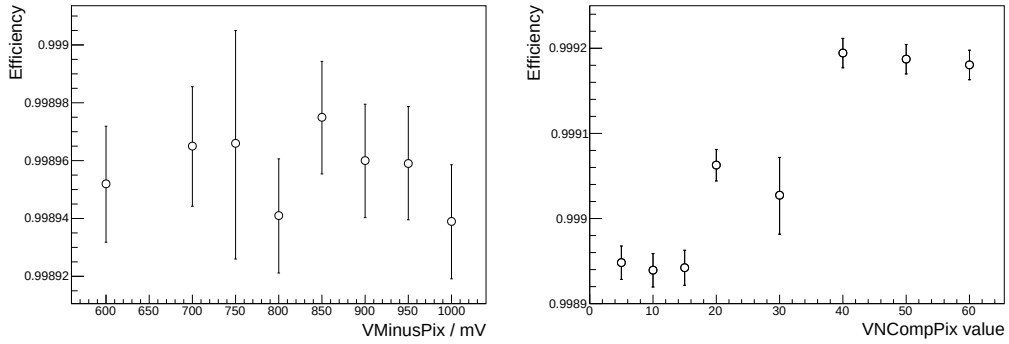

(a) (b)

Figure 6.4: Efficiency vs (a) VMinusPix and (b) VNCompPix for ATLASPix_IsoSimple

values for which the efficiency is still above 99 %.
Figure 6.4 shows the efficiency plotted against VMinusPix and VNCompPix for a threshold value of 80 mV and HV = −60 V. In both cases, the effect is negligible.

Time resolution

The results presented in this subsection were obtained in the scope of and presented first in a Master thesis [69]. They are based on laboratory measurements similar to those discussed in the part on timewalk correction in section 5.3.8.
ATLASPix_IsoSimple shows a much smaller variation of TS1 − t_{ref} with the

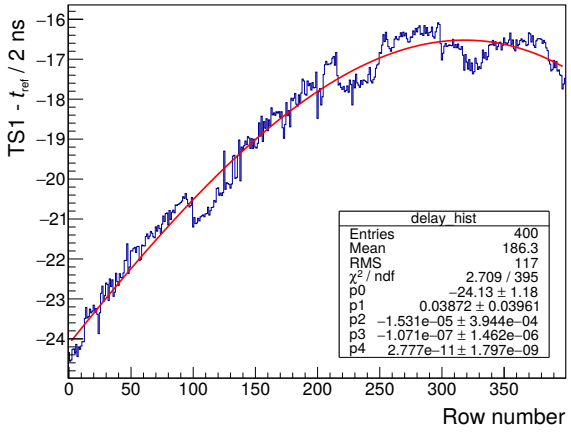

Figure 6.5: Mean of TS1 − t_{ref} distribution vs row number for ATLASPix_IsoSimple [69]

row number than ATLASPix_Simple. The difference between the maximum and the minimum value is approximately 16 ns (see figure 6.5 [69]). For ATLASPix_Simple, it is ca. 50 ns for a comparable chip configuration (see figures 5.36 and 5.43). In general, variations in the signal delay are related to the varying capacitances between the signal lines from the active pixels to the readout cells due to their different lengths (as discussed is section 5.3.8). It is assumed that the overall smaller delays of ATLASPix_IsoSimple stem from the larger amplitude and the faster rise of the comparator output signals compared to ATLASPix_Simple This would be consistent with the larger crosstalk probability discussed above.
The smaller delay variations lead to a better time resolution before offline corrections. After offline corrections it is approximately the same as for ATLASPix_Simple. Figure 6.6 [69] shows the time resolution σ of the whole sensor plotted against VMinusPix and VNCompPix. The threshold was 65 mV and the HV was −60 V. The best result after all offline corrections is ca. 6.5 ns, which is about 1.5 ns better than that obtained with ATLASPix_Simple with a similar chip configuration (see figure 5.46). Figure 6.7 [69] shows the σ of all individual pixels as pixel map and as histogram measured with an HV of −75 V and a VNCompPix value of 20. The mean is ca. 5.8 ns and the RMS is ca. 0.3 ns. Threshold and HV were slightly different here than for the analog measurement with ATLASPix_Simple (see figure 5.47), where the threshold value was 80 mV and the HV was −80 V. The results, however, are not significantly different. In the case of ATLASPix_Simple, the mean is ca. 5.9 ns and the RMS is also 0.3 ns.

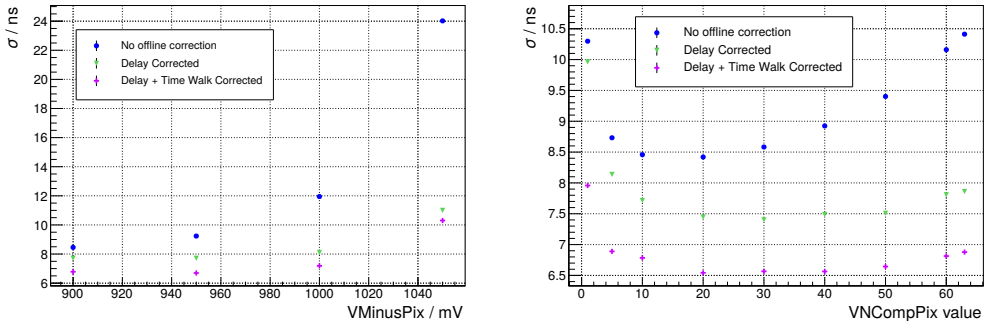

(a) (b)

Figure 6.6: σ vs (a) VMinusPix and (b) VNCompPix for ATLASPix_IsoSimple [69]

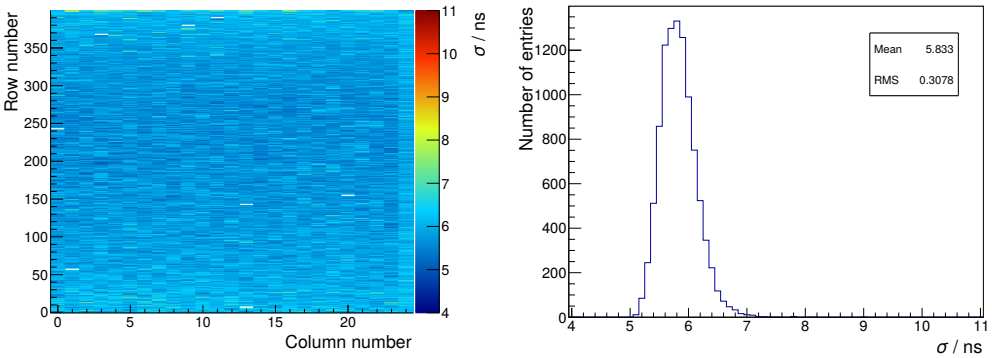

(a) (b)

Figure 6.7: σ of individual pixels as (a) pixel map and (b) histogram for ATLASPix_IsoSimple [69]

Chapter 7

Conclusion

The tracking system of the ATLAS detector at the LHC will be upgraded to retain excellent performance during the operation of the HL-LHC. At the time of this thesis being finalized, the decision has been made that the pixel detector of the new ITk will be constructed according to its baseline design, which foresees the use of hybrid pixel sensors alone. Initially, monolithic pixel sensors were considered as alternative options for the outermost pixel layer, mainly motivated by their comparatively low production costs.
Within the scope of this thesis, the HV-MAPS prototype ATLASPix_Simple was characterized and investigated regarding its suitability for the ITk upgrade. The test systems developed for characterizing MuPix prototypes were adapted to commission the sensor and characterize it in the laboratory and at eight testbeam campaigns.
The basic sensor performance was studied using unirradiated samples with substrate resistivities of 80 Ωcm and 200 Ωcm. The reverse leakage current was measured to be of the order of 0.1 µA down to an HV of ca. −70 V, where the breakdown starts. The breakdown occurs at less reverse bias than expected from the process specifications. The exact reason for this is still under investigation. However, the achievable reverse bias voltages are sufficient for a good sensor performance, as discussed below.
The power consumption of the sensor was measured to be between 160 mW and 200 mW for most sensor configurations used in the context of the thesis. Based on these values, the power consumption of a full-size sensor ($4 \times 4\,\mathrm{cm}^2$ active area, 4 LVDS links) is estimated to equal between ca. 0.9 W and 1.2 W.
An SNR of ca. 10 was measured for a substrate resistivity of 200 Ωcm using ^{55}Fe as signal source. This corresponds to a noise level of ca. 160 signal electrons.
All measurements presented in the thesis were performed without threshold tuning for individual pixels, although the possibility for that is implemented

on the chip in the form of three tuning bits per pixel. Instead, $\mathcal{O}(1)$ very noisy pixels were typically switched off.
Efficiencies of up to ca. 99.8 % were measured and it is shown that this result is achieved without matching noise hits. A large range of threshold values was found to result in efficiencies above 99 % at a low noise rate, especially for a substrate resistivity of 200 Ωcm. The measured noise rates are overestimated in the sense that they include all real particle hits that are not associated with a track. They are found to be $\mathcal{O}(1\,\text{Hz})$ per pixel, except for very low thresholds (compared to the efficiency plateau), at which they rapidly increase.
The size and orientation of hit clusters as well as their distribution over the sensor were investigated to study charge sharing, which was found to only occur between neighboring pixels, and line crosstalk. A comparison with MuPix8 shows that the implementation of the comparator inside the active pixel suppresses line crosstalk over a large part of the chip. Tuning the receiver DACs, which was not done within the scope of this thesis, could suppress crosstalk even further.
No studies on rate capability were carried out with ATLASPix_Simple. Its continuous readout scheme is not suitable to read out the expected hit rate of the outer layer of the ITk of 400 MHz per sensor, where a sensor has an active area of approximately $2 \times 2\text{cm}^2$. The LVDS link of ATLASPix_Simple can theoretically read out a hit rate of 28.3 MHz. It was tested with MuPix9, which has the same readout scheme, that the link saturates at a noise hit rate of ca. 27 MHz [86]. The best result for the time resolution of ATLASPix_Simple (without timewalk correction) that is presented in this thesis is $\sigma \approx 6.8$ ns. This would correspond to ca. 93.4 % of detected hits being "in-time" at the bunch spacing of 25 ns at the LHC. The result was obtained for a substrate resistivity of 200Ωcm and by performing an offline correction for varying signal delays over the chip, which are a result of the different lengths of the signal lines connecting the pixels with the readout cells in the chip's periphery. The necessity of this correction is one of several unintended design features of ATLASPix_Simple, which are related to its timing performance. The bin size of the timestamp used for the measurement of the time of arrival could have been made smaller. MuPix8 uses half the bin size of ATLASPix_Simple. With this, one would expect the above result to improve to $\sigma \approx 5.5$ ns, which would correspond to ca. 97.7 % of "in-time" hits.
A second timestamp is sampled on ATLASPix_Simple, with which the ToT can be calculated. The ToT can be used to perform an offline timewalk correction. It turned out that hits are partially read out before the second timestamp is sampled when the state machine is operated at full speed. Dedicated measurements with slowed-down state machine were carried out in the

laboratory by a master student. The improvement of the time resolution due to timewalk correction increases with the threshold. For the lowest tested thresholds, the improvement is not significant. However, if the timewalk correction could be implemented for example on a front-end FPGA, it would be beneficial after irradiation, when the threshold has to be increased due to noise.
Additional testbeam measurements were performed using a EUDET-type reference telescope, which provides a pointing resolution that allows for resolving sub-pixel effects. The results on efficiency, time resolution, and charge sharing provide a consistent picture.
Several irradiation campaigns were carried out. Testbeam measurements were performed with ATLASPix_Simple samples that were irradiated with neutron fluences between $1 \cdot 10^{14}\,\mathrm{n_{eq}/cm^2}$ and $2 \cdot 10^{15}\,\mathrm{n_{eq}/cm^2}$ and an 18 MeV proton fluence of $5 \cdot 10^{14}\,\mathrm{n_{eq}/cm^2}$.
An efficiency of above 99 % at a noise rate of below 40 Hz per pixel was measured after irradiation with a neutron fluence of $1 \cdot 10^{15}\,\mathrm{n_{eq}/cm^2}$, which is the expected lifetime fluence for the sensors of the outermost pixel layer of the ITk.
An efficiency of 98.7 % was measured after irradiation with a fluence of $2 \cdot 10^{15}\,\mathrm{n_{eq}/cm^2}$ at a noise level below 40 Hz per pixel, despite a large number of masked pixels (60).
The sample that was irradiated with a neutron fluence of $1 \cdot 10^{14}\,\mathrm{n_{eq}/cm^2}$ has a lower efficiency than samples irradiated with higher fluences, which corresponds to a known problem that is not yet understood. Irradiation with small fluences needs to be studied further.
One single proton irradiated sample was tested in the context of this thesis. The fluence of $5 \cdot 10^{14}\,\mathrm{n_{eq}/cm^2}$ corresponds to a TID of ca. $4.8 \cdot 10^5$ Gy, which corresponds to the expected lifetime TID for the outermost pixel layer of the ITk. While an efficiency of 99.9 % was measured, differences in the performance compared to neutron irradiated samples were observed, e.g. a higher leakage current, which could be caused by a larger fraction of removed acceptors. Further studies of the HV-MAPS technology regarding irradiation with charged hadrons should be carried out.
In general, no significant deterioration of the time resolution after irradiation was observed. However, the increased noise level requires the operation at higher thresholds than for unirradiated sensors, where the time resolution is worse due to increased timewalk. Threshold tuning or lower sensor temperatures could allow for the operation of irradiated sensors at lower thresholds.
While ATLASPix_Simple uses an NMOS comparator, ATLASPix_IsoSimple makes use of a deep p-well implant in the active pixel to implement a CMOS comparator. The deep p-well is a non-standard process option, which was

tested for the first time with this chip. ATLASPix_IsoSimple shows promising results in terms of time resolution and its use of CMOS logic has the advantage of requiring one supply voltage less than the NMOS comparator of ATLASPix_Simple. The efficiency of both sensors was measured to be similar.
Although no monolithic pixel sensors will be implemened in the ITk, it was shown that the HV-MAPS technology shows great potential for future applications in particle physics experiments, especially due to its high radiation tolerance combined with a monolithic architecture. At the time that this thesis is being finalized, the next large-scale iteration of HV-MAPS prototypes, ATLASPix3, is being commissioned.

Appendix

A1 Default sensor configuration

DAC/Configuration bits	value
VNBiasPix	0
VPPix	20
VPPix2	0
VNFBPix	10
VPLoadPix	10
VNFollPix	10
VPFoll	0/20
BLResPix	10
VNCompPix	10
VNDACPix	0
VPBiasRec	30
VNBiasRec	25
VNHB	0/63
VPHB	0/63
VNPEdge	10
VNVCO	13
VPVCO	12
VPPump	63
Invert	0

DAC/Configuration bits	value
VNDcl	40
VPDcl	10
VNDelDcl	40
VPDelDcl	40
VNDelDclMux	24
VPDelDclMux	24
VNLVDS	30
VNLVDSDel	0
VNDelPreEmp	24
VPDelPreEmp	24
SelEx	0
SelSlow	0
EnablePll	1
Readout_reset_n	1
Serializer_reset_n	1
Aurora_reset_n	1
sendcounter	0
resetckdivend	15
maxcycend	63
slowdownend	15
timerend	0/15
ckdivend	0
ckdivend2	7

Table A1.1: DAC and configuration bit values used as default

A2 Straight line fit formulae

The testbeam measurements discussed in this thesis were performed without a magnetic field. The analyses are based on straight tracks. The underlying assumption that allows for the application of this track model is that the amount of multiple Coulomb scattering in the tracking layers is negligibly small.
The global coordinate system is chosen to be left-handed with the x- and y-axis being defined to lie in the plane of the first tracking layer. The x-axis is parallel to the pixel rows of the sensor and the y-axis parallel to the pixel columns. The origin lies in the center of pixel (0,0). Tracks are described by

$$\begin{pmatrix} x(z) \\ y(z) \end{pmatrix} = \begin{pmatrix} x_0 \\ y_0 \end{pmatrix} + \begin{pmatrix} \frac{\mathrm{d}x}{\mathrm{d}z} \\ \frac{\mathrm{d}y}{\mathrm{d}z} \end{pmatrix} z \,. \tag{A2.1}$$

The fit is performed by the minimization of χ^2, which is defined as

$$\chi^2 = \sum_{i=1}^{n} \Big(\frac{(x_i - (x_0 + \frac{\mathrm{d}x}{\mathrm{d}x} z_i))^2}{\sigma_{x,i}^2} + \frac{(y_i - (y_0 + \frac{\mathrm{d}y}{\mathrm{d}z} z_i))^2}{\sigma_{y,i}^2} \Big) \,, \tag{A2.2}$$

with n being the number of tracking planes, $(x_i, y_i)^{\mathrm{T}}$ the center of the hit pixel of the i-th layer, and $\sigma_{x/y,i}$ the measurement uncertainty, which is the pixel pitch devided by $\sqrt{12}$. Setting the derivates of χ^2 with respect to the track parameters to zero yields [73]

$$\begin{pmatrix} \sum_i x_i \\ \sum_i x_i z_i \\ \sum_i y_i \\ \sum_i y_i z_i \end{pmatrix} = \begin{pmatrix} \sum_i z_i & \sum_i 1 & 0 & 0 \\ \sum_i z_i^2 & \sum_i z_i & 0 & 0 \\ 0 & 0 & \sum_i z_i & \sum_i 1 \\ 0 & 0 & \sum_i z_i^2 & \sum_i z_i \end{pmatrix} \begin{pmatrix} \frac{\mathrm{d}x}{\mathrm{d}z} \\ x_0 \\ \frac{\mathrm{d}y}{\mathrm{d}z} \\ y_0 \end{pmatrix} \,. \tag{A2.3}$$

This can be solved analytically resulting in the best estimate for the track parameters.

A3 Efficiency error calculation

The efficiency ϵ is given by

$$\epsilon = \frac{k}{n} \tag{A3.1}$$

with k being the number of tracks with a matching DUT hit in the ROI and n the number of all tracks going through the ROI on the DUT.
A statistical error on the efficiency can be calculated assuming the detection of hits can be regarded as a Bernoulli process. The probability mass function for detecting k out of n incident particles is then

$$P(k; n, \epsilon_{\text{true}}) = \binom{n}{k} \epsilon_{\text{true}}^{k} (1 - \epsilon_{\text{true}})^{n-k} \tag{A3.2}$$

with the true efficiency ϵ_{true}. In Bayesian statistics the probability density function for ϵ being the correct efficiency for given k and n is

$$P(\epsilon; k, n) = \frac{P(k; n, \epsilon) P(\epsilon; n)}{C}\,, \tag{A3.3}$$

where $P(k; n, \epsilon)$ is defined in equation A3.2, C is a normalization constant, and $P(\epsilon; n)$ is the probability distribution of ϵ for a given n prior to any measurement, which can be assumed to be constant.
The upper ($\epsilon+$) and lower ($\epsilon-$) boundries of an error interval $\Delta\epsilon$ can be defined by requiring for $\Delta\epsilon$ to be the smallest interval that fulfills

$$\frac{\int_{\epsilon-}^{\epsilon+} \epsilon'^{k} (1 - \epsilon')^{n-k} \, \mathrm{d}\epsilon'}{\int_{0}^{1} \epsilon'^{k} (1 - \epsilon')^{n-k} \, \mathrm{d}\epsilon'} = \text{C.L.} \tag{A3.4}$$

for a specific confidence level C.L.. In the context of this thesis, it is chosen to be 0.683 [73], which corresponds to the standard deviation of the normal distribution. Figure A3.1 shows an illustrative example of $\Delta\epsilon$.
The calculation of the above discussed efficiency error is implemented in the TEfficiency class of the ROOT [85] library.

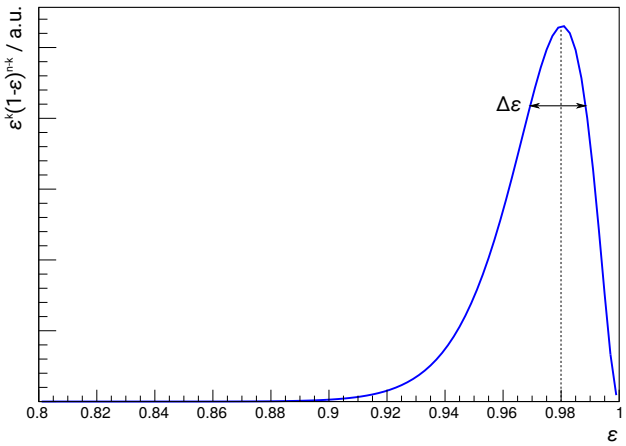

Figure A3.1: Illustrative example of the asymmetric efficiency error determined via the binomial distribution

List of own puplications

Some of the ideas and figures presented in this thesis may have previously appeared in the following journal articles and conference proceedings:

H. Augutin et. al, *MuPix8 - A large-area HV-MAPS chip*, PoS (Vertex 2017) 057, 2017.

D. Wiedner et al., *Readout Electronics for the First Large HV-MAPS Chip for Mu3e*, PoS (TWEPP-17) 099, 2018.

H. Augutin et. al, *Irradiation study of a fully monolithic HV-CMOS pixel sensor design in AMS 180 nm*, Nucl. Instrum. Methods Phys. Res. A 905, 2018.

H. Augutin et. al, *MuPix8 - Large area monolithic HVCMOS pixel detector for the Mu3e experiment*, Nucl. Instrum. Methods Phys. Res. A, 936, 2019.

H. Augutin et. al, *Performance of the large scale HV-CMOS pixel sensor MuPix8*, Proceesings of The 9th International Workshop on Semiconductor Pixel Detectors for Particles and Imaging, JINST, Vol. 14, 2019.

Bibliography

[1] CERN Document Server, *Overall view of the LHC*, URL: https://cds.cern.ch/record/1708847, online, accessed on 16.10.2019.

[2] ATLAS collaboration, *Observation of a New Particle in the Search for the Standard Model Higgs Boson with the ATLAS Detector at the LHC*, Physics Letters B, 716 (1), 1-29, 2012.

[3] CMS collaboration, *Observation of a new boson at a mass of 125 GeV with the CMS experiment at the LHC*, Physics Letters B, 716 (1), 30-61, 2012.

[4] ATLAS Collaboration, *The ATLAS Experiment at the CERN Large Hadron Collider*, JINST, Vol. 3, 2008.

[5] CMS Collaboration, *The CMS experiment at the CERN LHC*, JINST, Vol. 3, 2008.

[6] R. Aaij et al., *Observation of $J/\psi p$ Resonances Consistent with Pentaquark States in $\Lambda_b^0 \to J/\psi K^- p$ Decays*, Phys. Rev. Lett. 115, 072001, 2015.

[7] R. Aaij et al., *Observation of $J/\psi\phi$ Structures Consistent with Exotic States from Amplitude Analysis of $B^+ \to J/\psi\phi K^+$ Decays*, Phys. Rev. Lett. 118, 022003, 2017.

[8] *Nominal HL-LHC luminosity projection - updated with optimistic availability following Run 2*, URL: https://lhc-commissioning.web.cern.ch/lhc-commissioning/schedule/HL-LHC-plots.htm, online, accessed on 15.10.2019.

[9] Homepage of CERN, *The accelerator complex*, URL: https://home.cern/science/accelerators/accelerator-complex, online, accessed on 18.10.2019.

[10] CERN Document Server, *The CERN accelerator complex*, URL: https://cds.cern.ch/images/CERN-DI-0812015, online, accessed on 18.10.2019.

[11] G. Apollinari et al., *High-Luminosity Large Hadron Collider (HL-LHC) Technical Design Report V. 0.1*, CERN Yellow Reports: Monographs, Vol 4, 2017.

[12] P. Azzi et al., *Standard Model Physics at the HL-LHC and HE-LHC*, arXiv:1902.04070 [hep-ph], 2019.

[13] M. Cepeda et al., *Higgs Physics at the HL-LHC and HE-LHC*, arXiv:1902.00134 [hep-ph], 2019.

[14] X. Cid Vidal et al., *Beyond the Standard Model Physics at the HL-LHC and HE-LHC*, arXiv:1812.07831 [hep-ph], 2019.

[15] A. Cerri et al., *Opportunities in Flavour Physics at the HL-LHC and HE-LHC*, arXiv:1812.07638 [hep-ph], 2018.

[16] CERN Document Server, *Computer generated image of the whole ATLAS detector*, URL: http://cds.cern.ch/images/CERN-GE-0803012-01, online, accessed on 16.10.2019.

[17] ATLAS Collaboration, *ATLAS inner detector : Technical Design Report, 1*, CERN-LHCC-97-016 ; ATLAS-TDR-4, 1997.

[18] CERN Document Server, *Computer generated image of the ATLAS inner detector*, URL: https://cds.cern.ch/images/CERN-GE-0803014-01, online, accessed on 16.10.2019.

[19] G. Casse et al., *Improving the radiation hardness properties of silicon detectors using oxygenated n-type and p-type silicon*, IEEE Transactions on Nuclear Science, Vol. 47 (3), 2000.

[20] M. Capeans et al., *ATLAS Insertable B-Layer Technical Design Report*, CERN-LHCC-2010-013 ; ATLAS-TDR-19, 2019.

[21] ATLAS Collaboration, *ATLAS magnet system : Technical Design Report, 1*, CERN-LHCC-97-018 ; ATLAS-TDR-6, 1997.

[22] ATLAS Collaboration, *ATLAS liquid-argon calorimeter : Technical Design Report*, CERN-LHCC-96-041 ; ATLAS-TDR-2, 1996.

[23] ATLAS Collaboration, *ATLAS tile calorimeter : Technical Design Report*, CERN-LHCC-96-042 ; ATLAS-TDR-3, 1996.

[24] CERN Document Server, *Computer Generated image of the ATLAS calorimeter*, URL: https://cds.cern.ch/images/CERN-GE-0803015, online, accessed on 17.10.2019.

[25] ATLAS Collaboration, *ATLAS muon spectrometer : Technical Design Report*, CERN-LHCC-97-022 ; ATLAS-TDR-10, 1997.

[26] E. Diehl, *ATLAS Muon Detector Commissioning*, Proceedings of DPF-2009 Conference, Detroit, arXiv:0910.2767 [physics.ins-det], 2009.

[27] ATLAS Collaboration, *ATLAS Forward Detectors for Measurement of Elastic Scattering and Luminosity*, CERN-LHCC-2008-004 ; ATLAS-TDR-18, 2008.

[28] ATLAS Collaboration, *ATLAS high-level trigger, data-acquisition and controls : Technical Design Report*, CERN-LHCC-2003-022 ; ATLAS-TDR-16, 2003.

[29] ATLAS Collaboration, *Technical Design Report for the Phase-II Upgrade of the ATLAS Muon Spectrometer*, CERN-LHCC-2017-017 ; ATLAS-TDR-026, 2017.

[30] ATLAS Collaboration, *Technical Design Report for the Phase-II Upgrade of the ATLAS LAr Calorimeter*, CERN-LHCC-2017-018 ; ATLAS-TDR-027, 2017.

[31] ATLAS Collaboration, *Technical Design Report for the Phase-II Upgrade of the ATLAS Tile Calorimeter*, CERN-LHCC-2017-019 ; ATLAS-TDR-028, 2017.

[32] ATLAS Collaboration, *Technical Design Report for the Phase-II Upgrade of the ATLAS TDAQ System*, CERN-LHCC-2017-020 ; ATLAS-TDR-029, 2017.

[33] ATLAS Collaboration, *Technical Proposal: A High-Granularity Timing Detector for the ATLAS Phase-II Upgrade*, CERN-LHCC-2018-023 ; LHCC-P-012, 2018.

[34] ATLAS Collaboration, *Letter of Intent for the Phase-II Upgrade of the ATLAS Experiment*, CERN-LHCC-2012-022 ; LHCC-I-023, 2012.

[35] ATLAS Collaboration, *Technical Design Report for the ATLAS Inner Tracker Strip Detector*, CERN-LHCC-2017-005 ; ATLAS-TDR-025, 2017.

[36] ATLAS Collaboration, *Technical Design Report for the ATLAS Inner Tracker Pixel Detector*, CERN-LHCC-2017-021 ; ATLAS-TDR-030, 2017.

[37] ATLAS Collaboration, *Expected Tracking Performance of the ATLAS Inner Tracker at the HL-LHC*, ATL-PHYS-PUB-2019-014, 2019.

[38] *Review of the CMOS Pixel Option for the ITk Phase 2 Upgrade*, Committee report, 2019.

[39] W. Shockley, *Currents to conductors induced by a moving point charge*, J. Appl. Phys. 9 (10), 635, 1938.

[40] S. Ramo, *Currents induced by electron motion*, Proceeding of the IRE, 27 (9), 1939.

[41] L. Rossi, P. Fischer, T. Rohe, N. Wermes, *Pixel Detectors - From Fundamentals to Applications*, Springer, ISBN-13 978-3-540-28332-4, 2006.

[42] H. Spieler, *Semiconductor Detector Systems*, Oxford University Press, DOI:10.1093/acprof:oso/9780198527848.001.0001, 2005.

[43] CyrilB, *IvsV_mosfet.svg*, URL: https://en.wikipedia.org/wiki/MOSFET#/media/File:IvsV_mosfet.svg, licensed under CC BY-SA 3.0 (URL: https://creativecommons.org/licenses/by-sa/3.0/deed.en), online, accessed on 09.11.2019.

[44] C. T. Sah, *Origin of Interface States and Oxide Charges Generated by Ionizing Radiation*, IEEE Trans. Nucl. Sci., 23 (6), 1976.

[45] J. R. Schwank et al., *Radiation Effects in MOS Oxides*, IEEE Trans. Nucl. Sci., 55 (4), 2008.

[46] M. Huhtinen, *Simulation of non-ionising energy loss and defect formation in silicon*, Nucl. Instrum. Methods Phys. Res. A, 491, 2002.

[47] M. Moll, *Radiation Damage in Silicon Particle Detectors - microscopic defects and macroscopic properties* -, PhD thesis, University of Hamburg, 1999.

[48] R. Wunstorf, *Systematische Untersuchungen zur Strahlenresistenz von Silizium-Detektoren für die Verwendung in Hochenergiephysik-Experimenten*, PhD thesis Hamburg, 1992.

[49] G. Casse et al., *A comparative study of oxygenated and non-oxygenated Si pad diodes, miniature and large area microstrip detectors*, Nucl. Instrum. Methods Phys. Res. A, 466, 2001.

[50] G. Kramberger et al., *Initial acceptor removal in p-type silicon*, presentation given at 10th Anniversary "Trento" Workshop on Advanced Silicon Radiation Detectors, 2015.

[51] P. Dias de Almeida et al., *Measurement of the acceptor removal rate in silicon pad diodes*, presentation given at 30th RD50 Workshop on Radiation hard semiconductor devices for very high luminosity colliders, 2017.

[52] Y. Gurimskaya et al., *RD50 Acceptor Removal Project and Defect Characterization at CERN*, presentation given at 33rd RD50 Workshop on Radiation hard semiconductor devices for very high luminosity colliders, 2018.

[53] H. Kolanoski, N. Wermes, *Teilchendetektoren*, Springer-Verlag Berlin Heidelberg, DOI: 10.1007/978-3-662-45350-6, 2016.

[54] M. Tanabashi et al. (Particle Data Group), *Review of Particle Physics*, Phys. Rev. D 98, 030001, 2018.

[55] N. Savić, *Development of Pixel Detectors for the Inner Tracker Upgrade of the ATLAS Experiment*, PhD thesis, Ludwig Maximilian University of Munich, 2017.

[56] J. Lange et al., *Radiation hardness of small-pitch 3D pixel sensors up to a fluence of* $3 \times 10^{16}\, n_{eq}/cm^2$, JINST, Vol. 13, 2018.

[57] C. Da Via et al., *3D silicon sensors: Design, large area production and quality assurance for the ATLAS IBL pixel detector upgrade*, Nucl. Instrum. Methods Phys. Res. A, 694, 2012.

[58] S. Terzo, *The Phase-II ATLAS ITk Pixel Upgrade*, Proceedings of International Conference on Instrumentation for Colliding Beam Physics 2017 (INSTR17), JINST, Vol. 12, 2017.

[59] J. T. Boisers, *Technical challenges and recent progress in CCD imagers*, Nucl. Instrum. Methods Phys. Res. A, 565, 2006.

[60] K. D. Stefanov, *CCD developments for particle colliders*, Nucl. Instrum. Methods Phys. Res. A, 565, 2006.

[61] G. Contin et al., *The STAR MAPS-based PiXeL detector*, Nucl. Instrum. Methods Phys. Res. A, 907, 2018.

[62] A. Besson et al., *From vertex detectors to inner trackers with CMOS pixel sensors*, Nucl. Instrum. Methods Phys. Res. A, 845, 2017.

[63] G. Algieri Rinella, *The ALPIDE pixel sensor chip for the upgrade of the ALICE Inner Tracking System*, Nucl. Instrum. Methods Phys. Res. A, 845, 2017.

[64] W. Snoeys et al., *A process modification for CMOS monolithic active pixel sensors for enhanced depletion, timing performance and radiation tolerance*, Nucl. Instrum. Methods Phys. Res. A, 871, 2017.

[65] H. Pernegger et al., *First tests of a novel radiation hard CMOS sensor process for Depleted Monolithic Active Pixel Sensors*, JINST, 12, 2017.

[66] R. Cardella et al., *MALTA: an asynchronous readout CMOS monolithic pixel detector for the ATLAS High-Luminosity upgrade*, Proceedings of the 9th International Workshop on Semiconductor Pixel Detectors for Particles and Imaging, JINST, 2019.

[67] I. Perić, *A novel monolithic pixelated particle detector implemented in high-voltage CMOS technology*, Nucl. Instrum. Methods Phys. Res. A, 582, 2007.

[68] A. Blondel et al., *Research Proposal for an Experiment to Search for the Decay $\mu \to eee$*, arXiv:1301.6113 [physics.ins-det], 2013.

[69] D. Immig, *Characterization of ATLASPix1, an HV-CMOS Demonstrator for the Phase-II Upgrade of the ATLAS Inner Tracker*, Master thesis, Heidelberg University, 2019.

[70] I. Perić et al., *Description of the ATLASPIX_Simple and ATLASPIX_M2*, User guide, preliminary version, 2017.

[71] Intel, *Stratix IV GX FPGA Development Kits*, URL: https://www.intel.com/content/www/us/en/programmable/products/boards_and_kits/dev-kits/altera/kit-siv-gx.html, online, accessed on 08.08.2019.

[72] S. Dittmeier, *Fast data acquisition for silicon tracking detectors at high rates*, PhD thesis, Heidelberg University, 2018.

[73] L. Huth, *A High Rate Testbeam Data Acquisition System and Characterization of High Voltage Monolithic Active Pixel Sensors*, PhD thesis, Heidelberg University, 2018.

[74] J. Hammerich, *Analog Characterization and Time Resolution of a large scale HV-MAPS Prototype*, Master thesis, Heidelberg University, 2018.

[75] Homepage of the DESY testbeam facility, URL: http://particle-physics.desy.de/test_beams_at_desy/, online, accessed on 09.10.2019.

[76] Homepage of the secondary beam lines at PSI, URL: https://www.psi.ch/en/sbl, online, accessed on 09.10.2019

[77] Homepage of the EUDET-type beam telescopes, URL: https://telescopes.desy.de, online, accessed on 17.09.2019.

[78] A. Meneses González, PhD thesis, Heidelberg University, in preparation.

[79] J. Baudot et al., *First test results Of MIMOSA-26, a fast CMOS sensor with integrated zero suppression and digitized output*, IEEE Nuclear Science Symposium Conference Record, 2009.

[80] U. B. Hartenstein, *Track Based Alignment for the Mu3e Pixel Detector*, PhD thesis, Johannes Gutenberg University Mainz, 2019.

[81] V. Blobel, *Software alignment for tracking detectors*, Nucl. Instrum. Methods Phys. Res. A, 566, 2006.

[82] D. vom Bruch, *Pixel Sensor Evaluation and Online Event Selection for the Mu3e Experiment*, PhD thesis, Heidelberg University, 2017.

[83] Homepage of Reactor Infrastructure Centre (RIC) at JSI, URL: http://www.rcp.ijs.si/ric/index-a.htm, online, accessed on 01.10.2019.

[84] S. Braccini et al., *The New Bern Cyclotron Laboratory for Radioisotope Production and Research*, Proceedings of IPAC2011, THPS080, 2011.

[85] R. Brun, F. Rademakers, *ROOT - An object oriented data analysis framework*, Nucl. Instrum. Methods Phys. Res. A, 389,1997.

[86] H. Augustin, PhD thesis, Heidelberg University, in preparation.

Danksagung

An dieser Stelle möchte ich mich bei allen bedanken, die mich bei der Durchführung dieser Doktorarbeit unterstützt haben.
Zuerst bedanke ich mich bei meinem Doktorvater André Schöning, der mir bei meiner Arbeit die nötige Freiheit ließ und trotzdem immer die entscheidenden Fragen zu stellen wusste.
Außerdem danke ich Ulrich Uwer für seine Bereitschaft, die Rolle des Zeitgutachters zu übernehmen.
Besonderer Dank gilt allen Mitgliedern, ehemaligen Mitgliedern und Verdundenen der Mu3e-Gruppe für die gemeinsame Zeit über die vergangenen Jahre. Insbesondere danke ich Heiko Augustin, Lennart Huth, Sebastian Dittmeier, David Immig, Jan Hammerich und Lars Noehte für die unkomplizierte Zusammenareit, für ihre Hilfe bei meiner Arbeit und fürs Korrekturlesen. Bei Tamasi Kar bedanke ich mich außerdem für das Aushalten der Stille in unserem Büro.
Zum Abschluss danke ich meiner Familie und meinen Freunden, ohne die die Durchführung dieser Arbeit neben vielem anderen für mich nicht möglich gewesen wäre.